8.1.2.3 Ilvaite, lawsonite and related silicates

The sorosilicates from the ilvaite - lawsonite groups (VIII B03 - VIII B05) are listed in Table 1 [91N1].

8.1.2.3.1 Crystal structure. Lattice parameters

Barylite

The chemical composition of barylite, $BaBe_2Si_2O_7$, was determined in [62N1]. In the first structure analysis [64A1] was reported that barylite exhibits strong piezoelectricity and therefore must belong to the noncentrosymmetric space group $Pn2_1a$, despite the fact that structure is nearly centrosymmetric. The structure was reexamined by [69C1] and the space group Pnma was reported. Later on, by using X-ray studies and second harmonic generation (SHG), it has been shown that barylite is noncentrosymmetric [77R1]. The non-centrosymmetric barylite structure can be refined in the centrosymmetric space group Pnma. One possible explanation for the successful refinement in space group Pnma is the dominance of X-ray scattering by centrosymmetrically located heavy atoms (Ba in this structure). A satisfactory centrosymmetric refinement is not conclusive evidence of centrosymmetry.

Kilchoanite

The kilchoanite, $Ca_3Si_2O_7$, crystallizes in an orthorhombic tye structure having space group Imam or Ima2 [61A1].

Ilvaite

The chemical composition of ilvaite can be represented as $\langle Ca\rangle\{Fe^{2+}(A), Fe^{3+}(A), Fe^{2+}(B)\}[Si_2]O_8(OH)$ where [ ], { } and $\langle\ \rangle$ denote cation sites in tetrahedral, octahedral and sevenfold coordination, respectively. The natural ilvaites contain also small amounts of Mn, Al or Mg.

The structure of the ilvaite was studied by [48T1], who proposed an incorrect model with distinct SiO_4 groups. In [54B1] was found the correct basis of the structure which contains Si_2O_7 dimers. The structure was further investigated by X-ray [74B1] and by single-crystal neutron diffraction [76H1]. All above studies have assumed the symmetry to be orthorhombic, space group Pbnm, even though high-resolution powder diffraction [68B1, 72D1] showed the existence of a monoclinic polymorph. The monoclinic symmetry was later recognized [82F1, 83T1, 84G1, 85G1]. The correct space group, at normal conditions, is $P2_1/a$. The Ca^{2+} ions occupy one crystallographically equivalent sevenfold coordinated position. According to [83T1] one half of the Fe^{2+} ions occupy the Fe(B) sites, the other half Fe(Ao) and the Fe^{3+} ions the Fe(Am) sites. Fe(Ao) and Fe(Am) octahedra form an edge-sharing double octahedron chain running parallel to the ***c***-axis. However, Fe^{2+} and Fe^{3+} ions are not completely ordered within that double chain of octahedra. According to [83T1], the variation of the monoclinic angle β between 90.00° and 90.46° depends on the degree of disorder of Fe^{2+} and Fe^{3+} over Fe(Ao) and Fe(Am) sites. Complete order results if $\beta = 90.46°$ and ordering parameter is $Q = 1$; complete disorder gives $\beta = 90°$ and $Q = 0$, i.e. orthorhombic structure. Between these two extremes, ilvaites with completely different degrees of order were observed in nature [93G1]. Only at temperatures higher than a value T_t, the monoclinic structure transforms in the orthorhombic one. The phase transition has been located at temperatures T_t between 333 and 343 K [84G2, 87D1, 88G1, 88G2, 88R1], at 335 K [89G3] or 346 K [89G2]. This phase transition can be referred to an increasing disorder of Fe^{2+} and Fe^{3+} within the double octahedron chain with increasing temperature, which is documented by the decrease of the monoclinic angle β to 90°. This can be described as a λ transition, which occurs when there is a mixture of order-disorder and a displacive transitions [87F1].

In the orthorhombic structure, the mode of polyhedral linkage remains principally the same [93G1]. One half of the Fe^{2+} ions occupy the 4c positions (point symmetry 1) of the space group Pbnm, and the other half of Fe^{2+} ions fill together with Fe^{3+} in random distribution the 8d (point symmetry m) positions, whose coordination polyhedra form a double chain of octahedra running parallel to the ***c***-axis [71B1, 74B1, 76H1]. Thus, the orthorhombic-type structure consists of edge-sharing double chains of octahedra (A sites) running parallel to the ***c***-axis. Half as many larger octahedra (B sites) are attached above and below the chains, sharing edges with A site octahedra. Ca^{2+} ions and Si_2O_7 groups interconnect these chains - Fig. 1 [89G2]. The orthorhombic space

group Pbnm was used by some authors to describe the structure [74B1, 76H1]. Later on, space groups Pnam or Pnma were mostly considered - Table 2. The Pbnm space group is related to Pnam through an interchange of ***a***- and ***b***-axes.

The orthorhombic to monoclinic phase transition in ilvaite is displacive, the monoclinic space group $P2_1/a$ being a subgroup of the orthorhombic space group Pnam. Below T_t, in the orthorhombic phase, the mirror plane normal to ***c*** is lost but continues to serve as a possible mirror plane in the monoclinic structure, and the octahedral A site splits up into two unequivalent sites [82F1, 83T1, 84G1] which were called Ao and Am. O2 and O4 atoms likewise split up into O2o, O2m and O4o, O4m, respectively. We used in the following this nomenclature which has the advantage of indicating the genetic relationships of atoms concerned above and below the phase transition [89G2]. For equivalence with other notations see Table 2.

Detailed studies on crystal structures of monoclinic ilvaites were also performed [82F1, 83T1, 94T1]. The Fe^{2+} and Fe^{3+} cations were partially ordered in the double chains of edge-sharing octahedra formed by oxygen ions about the above cations. In particular, the structure of two ilvaites, one having $\beta = 90.324(9)^o$ and the other $90.03(1)^o$ were compared, the result suggesting a possible linear correlation between β and the order parameter, Q, which represents the degree of ordering in the distribution of Fe^{2+} and Fe^{3+} ions [83T1]. Later on, in [84G1, 87F1, 89G2, 94C2] has been confirmed the linear relationships between chemical composition (iron distribution, Mn content) and crystallographic parameters (b and β). To account for such a peculiar nature of ilvaite, as exhibiting a variety of β angles (or values of order parameter), two crystallographic mechanisms have been suggested, by which an ilvaite structure with order parameter $Q = 1$ may seemingly produce ilvaite crystals with various β values [83T1]. One is polysynthetic twinning with the twin plane parallel to (001). The other is a disorder characterized by mutual displacement of the double chains by $c/2$. The variation of angle β in various ilvaite crystals most probably lies in the fine scale twinning associated with the orthorhombic to monoclinic transition [85G1]. It has been noted that the angle β of crystals, from the same sample, was not necessarily the same [89G2]. Local portions of the same crystal of ilvaite with moderate size revealed that the monoclinic and apparently orthorhombic structures co-exist in the crystal, regardless of their mode of occurrence [94T1]. The diffraction from the crystals of high monoclinicity ($\beta \cong 90.2^o \ldots 90.3^o$) splits into a doublet peak, suggesting that the crystals are most likely made up of two kinds of domains, each having a monoclinic structure with $\beta = 90.45^o$, one twinned on (001) and the other twinned on (100) [94T1]. In the case of crystals of low monoclinicity ($\beta \cong 90.0^o$), the reflections tend to exhibit single broad profiles with fine structure. These are, in general, formed by superposition of three peaks, suggesting that they consist of complex composites of fine monoclinic components twinned on (001) and on (100), respectively.

According to [87G2], above 400 K, ilvaite shows a considerable $Fe^{2+} \leftrightarrow Fe^{3+}$ electron delocalization in the octahedral A(8d) sites [85G1]. A crystallographic phase transition from orthorhombic to monoclinic symmetry takes place, on cooling at T_t temperature, induced by electron ordering. The temperature at which the charge ordering starts depends on the exact composition and the origin of the sample. The monoclinic structure persists down to 5 K [84G1, 84G2]. The mechanism of transition from monoclinic to orthorhombic-type lattice, correlated with the nature of charge localization, was also analysed [82F1, 83T1, 84G1, 84G2, 85G1, 87F1]. Within the double octahedral chains (A sites), pairs of Fe^{2+} ions alternate with pairs of Fe^{3+} ions. Within a single octahedral Fe^{2+}-Fe^{3+}-Fe^{2+} chain, a short Fe^{2+}-Fe^{3+} bond (2.81 Å) alternates with a long bond (3.02 Å). The tightly bound Fe^{2+}-Fe^{3+} pairs (intermediate polarons) have been suggested as the charge carriers [88G2].

When increasing the temperature, both ***a*** and ***b*** lattice constants increase - Fig. 2 [89G2]. Above $T_t = 346$ K the slopes decrease slightly for ***a***, but increases for ***b***. On heating, ***c*** remains virtually constant and then increases. On cooling, the change in slope, at 390 K, is not discernible. Only the ***c*** lattice parameters show a slight hysteresis effect. The β angle decreases rapidly from 295 K to 345 K, beyond which it decreases very slowly in an asympthotic fashion attaining a virtual value $\beta = 90^o$ above 390 K - Fig. 2. The fact that β does not go to 90^o at T_t is connected with the precursor cluster fluctuations above the transition temperature. When increasing the temperature, the size of the Ao octahedron decreases, whereas that of the Am octahedron increases reflecting increasing Fe^{3+} and Fe^{2+} contents, respectively, at these sites. Finally, both attain the same size above 380 K. The differences in the average size of Ao and Am octahedra were related to the variation of angle β from 90^o, $\Delta\beta = \beta - 90^o$. Although the Ca polyhedron, Fe^{2+}(B) octahedron and the Si1 and Si2 tetrahedra are not directly involved in the charge localization process, they all sense the elastic strain associated with symmetry breaking, i.e. the loss of the mirror plane.

The atomic displacement vectors involved in the structural transition were calculated - Fig. 1 [89G2]. The most significant displacements involve oxygen atoms in the plane of the double octahedral chain, nearly parallel to (*ac*) plane. Oxygen O1 plays the most important role, which moves closer to Fe(Ao) and farther away from Fe(Am) with increasing temperature and increasing Fe^{3+} and Fe^{2+} contents, respectively, at these sites. The atomic movements of O1 are parallel or antiparallel to the ***c****-axis as determined from the normal mode analysis. The large anisotropic thermal vibration of O1 with the largest vibrational component parallel to ***c**** is consistent with this picture - Table 2. The other two oxygen atoms showing considerable atomic displacements parallel or antiparallel to ***c**** are O3 and O7 which define the edges of the double octahedral chain.

The effective valence charges, S, were calculated at room temperature and 138 K [85G1]. The *S* values indicate a small but significant increase in the Fe^{3+} content at the Am site, at 138 K. Although a major portion of the itinerant electrons are ordered during the orthorhombic to monoclinic phase transition, the rest of electrons has been sugggested to order slowly with decreasing temperature. Ordering is completed at a temperature very close to 0 K. The *S* values for the Fe^{2+} ions at the B site change very little with temperature.

As already mentioned, the ordering parameter, *Q*, has been proposed [83T1, 84G1, 87F1, 89G2, 94C2] to describe the distribution of Fe^{2+} and Fe^{3+} between Fe(Ao) and Fe(Am) sites, defined by the relation $Q = (OP - 0.5)/0.5$, where OP indicates the Fe^{2+} and Fe^{3+} occupancy at Fe(Ao) and Fe(Am) determined by measuring the mean bond lengths of the two sites. $Q = 0$ characterizes the orthorhombic and $Q = 1$ the monoclinic ilvaite. The data obtained by the study of a large number of ilvaites show that $Q = 2.00(3)$ ($\beta - 90^o$) - Fig. 3 [94C2]. The order parameter *Q* is shown as function of temperature in Fig. 4. Within the temperature range 310…380 K, *Q* is found to be linear dependent on $\Delta\beta$, yielding the relation close to the above $Q = 1.73\ \Delta\beta$ [83T1, 89G2]. The temperature evolution of the strain components is plotted in Fig. 5 [89G2]. If the expression for the strain component e_{13} is expanded in terms of $\Delta\beta$ and if only the lowest order contributions are kept, the strain becomes a linear function of $\Delta\beta$. Hence $\Delta\beta$ behaves like a primary order parameter which can be fitted to the expression $\Delta\beta = \Delta\beta_o(T_t - T)^{\beta}$ with $\beta = 0.35(5)$. Above $T_t \cong 346$ K, the slow asympthotic decrease of e_{13} - Fig. 5 [89G2] - attaining a zero value at 380 K, indicates the presence of fluctuating precursor clusters with considerable short-range order above T_t. A peak in the specific heat (see section 8.1.2.3.8) coincides with the onset of long-range order at 380 K, whereas ^{57}Fe NGR studies indicate the onset of charge localization at higher temperatures ($T \cong$ 470 K) (see section 8.1.2.3.4). The coupling of the d^6 electrons of the Fe^{2+}(A) ion with a longitudinal optic phonon with polarization vector along ***c**** seems to be the mechanism which drive the phase transition. The electron-phonon coupling also provides a charge conduction mechanism through electron hopping, whereby the short-bonded Fe^{2+} - Fe^{3+} pair containing the d^6 electron (intermediate polaron) will break up and re-form, thereby propagating the electron one step along the ***c***-axis [89G2].

Pressure studies were performed on ilvaite [87F1, 93G1]. The natural sample transformed from monoclinic to orthorhombic at a pressure lower than 1.9 GPa [87F1]. There is no evidence for a discontinuity in the volume. For $p \leq 1.3$ GPa, the order parameter *Q* was fitted with a Landau relation $Q = 0.35\ (p_c - p)^{1/4}$ with $p_c = 1.54$ GPa. Accordingly the critical exponent for the high-temperatrure transition was 1/4 with a transition temperature $T_t \cong$ 360 K. In [93G1] was performed, in situ, high-pressure X-ray diffraction to investigate pure synthetic ilvaite at room temperature, and compared with results on natural crystals [87F1]. The lattice parameters decrease with pressure without any discontinuity. The angle β decreases and at $p = 2.25$ GPa, $\beta = 90^o$ and remains constant with further increase of pressure. The plot of monoclinic angle β against pressure shows the typical behaviour of a λ transition which occurs, when there is a mixture of order-disorder and displacive transitions.

$Ca\,Fe^{2+}_{2-x}\,Mn^{2+}_{x}\,Fe^{3+}[Si_2O_7/O/(OH)]$

The Mn atoms, commonly contained in natural ilvaites, in minor amounts, are preferentially located at 4c substitution for Fe^{2+} [76H1]. The distribution of Mn in the crystals tends to increase towards their marginal portions [93T1]. Crystal portions containing more than roughly 0.25 % Mn per formula unit assume orthorhombic symmetry at room temperature.

The study of synthetic Mn-bearing ilvaite have revealed that the β-angle decreases when increasing the Mn content [89G1]. For a $Ca\,Fe^{2+}_{2-x}\,Mn^{2+}_{x}\,Fe^{3+}OSi_2O_7OH$ with x = 0.12 a value $T_t = 370$ K was evidenced - Fig. 6 - while for x = 0.19, the transition temperature is $T_t = 295$ K [92G1]. The reason for the decrease of transition temperature was correlated with order-disorder phenomena (Fe^{2+}, Fe^{3+}) influenced by the Mn-content, valence

fluctuations and with relaxation of the ilvaite lattice [92G1, 93G1]. As mentioned above, in the monoclinic phase, there is electron hopping between Fe^{2+} and Fe^{3+} pairs, whereas in the orthorhombic phase there is an extended electron delocalization via a narrow d-band mechanism.

The coexistence of different symmetries in the same ilvaite crystal was attributed to the variation in scale or mode of twinning incorporated mainly with inhomogeneous distribution of Mn in crystal [83T1, 85G1, 93T1].

The lattice parameters of some ilvaites are listed in Table 3.

Lawsonite

Lawsonite, with the chemical formula $CaAl_2Si_2O_7(OH)_2 \cdot H_2O$, occurs in high-pressure, low-temperature metamorphic rocks. With a water content of ~ 11 wt % and a stability field extending to high pressures and temperatures, lawsonite is a possible candidate mineral for transporting water down into earth's mantle at subduction zones [94P1]. This is the only hydrous phase stable above 3.5 GPa [95P1].

The high-pressure relationship in a H_2O saturated synthetic $CaO–Al_2O_3–SiO_2–H_2O$ (CASH) system has been studied [68N1, 94P1, 94S1, 95S1]. In the CASH system, lawsonite forms from laumontite, $Ca(Al_2Si_4)O_{12} \cdot 4H_2O$, at approximately 0.3 GPa [68N1], and persists up to more than 9.2 GPa [94S1]. In [94P1] lawsonite was found to be stable at 12.0 GPa. The maximum thermal stability of lawsonite was reported to be 1040°C, at pressure of 9.2 GPa [94S1]. In [94P1] a maximum thermal stability was determined to be ~ 1080°C at 9.4 GPa. According to [95S1] the most extreme pressure condition under which pure lawsonite exists, is 12.0 GPa at 960°C.

The room temperature cell parameters of lawsonite were determined by [57S1, 61P2]. At the beginning the crystal structure was described in space group $C222_1$ [47W1]. The crystal structure was refined later in space group Ccmm [59R1]. Then, in [59P1, 60D1, 60R1, 61P1, 77H2, 78B1, 90L1] some discrepancies were resolved and the space group was confirmed to be Ccmm. The designation of crystallographic axes has not been consistent in literature. The axes were defined with the longest direction parallel to ***b***, in this case the space group designation should be Bbmm [74L1]. Now, it is general accepted to use the space group Cmcm [01M1].

Lawsonite undergoes two phase transitions below room temperature. The change in symmetry with decreasing temperature was reported as Cmcm $\xrightarrow{T_1}$ Pmcn $\xrightarrow{T_2}$ $P2_1cn$ with transition temperatures at T_1 = 273(5) K [95L1, 00S2, 01M2] or at 265 K [00M1] and T_2 = 155(5) K [95L1], 130 K [00M1] or 120 K [00S2]. The first transition is a result of decreased thermal libration of water molecule, with the molecule slightly canting and allowing cooperative hydrogen bonding to form. The hydrogen bonds further strengthen at the lower temperature transition, with further canting of the water molecule, and the crystal symmetry is reduced by the movement of the hydrogen atoms out of the [010] plane [95L1].

A projection of the lawsonite Cmcm structure, at 295 K, parallel to [100] is shown in Fig. 7 [95L1]. The atomic coordinates are given in Table 2. The structure consists of rods of edge-sharing AlO_6 octahedra that run parallel to [100] and are interconnected by Si_2O_7 groups. The remaining interstices of the framework are occupied by Ca, an H_2O molecule (O5, 2xHw) and an OH site (O4, Hh), which has twice the multiplicity of O5 (two OH groups pfu). The H_2O molecule occupies a special position with site symmetry m2m, the symmetry of a single, free H_2O molecule. The O5-Hw distances (0.80…0.81 Å) are shorter than those in a free H_2O molecule (~ 0.98 Å) [95L1]. These values are representative of the delocalized H electron [95L1]. The H–O–H angle is larger than the one observed for a free H_2O molecule. According to [95L1] this might be caused by the attractive power of two additional hydrogen bonds to O4 atoms or by the librational motion of the H_2O molecule within the (100) plane. ^1H NMR single crystal measurements at 295 K [95G1] suggest that the H atoms of the H_2O molecule and OH groups are dynamically (time averaged) disordered, oscillating between two equivalent sites. The H atoms of the OH groups are bound to O4 at a distance 0.66…0.71 Å. These short bonds, according to [95L1], are the result of delocalized H electron. The O4-Hh vector and the O5-Hw vectors are parallel to (100) [74L1]. The anisotropic displacement factors of O5 (H_2O molecule) show a preferred elongation along [100]. The strongly anisotropic behaviour of the O5 atom was explained by the next-neighbor environment, which forms cavity elongated parallel to ***a*** [95L1].

The atomic coordinates of the Pmcn lawsonite structure are given in Table 2d [95L1]. In comparison with the Cmcm structure, there seem to be no striking changes in the positions of the Ca, Al, Si and O atoms. Only minor shifts (max 0.09 Å parallel to ***c***) of the fractional coordinates were observed. At the phase transition, the H atoms shift by maximum 0.4 Å parallel to ***c*** and there is a change of their next-neighboring interactions within the structure. The H_2O molecules rotate within the (100) plane, thus lowering the local m2m symmetry to m – –.

The OH groups, symmetrically related in the Cmcm structure, split into two different OH groups by rotation within the (100) plane.

A projection of the $P2_1cn$-type structure is shown in Fig. 8c and the atomic coordinates are listed in Table 2e. The major differences (except for small changes in the framework atoms) between the structures determined at 155 K (Pmcm) and at 110 K were related to the positions of the H atoms (maximum shifts of 0.25 Å parallel to ***a***). Whereas the H atoms are on special positions in the Pmcn structure, in the $P2_1cn$ structure the weakly bonded H atom of the H_2O molecule shifts below the former Pmcn m-plane (to x = 0.958) and the weakly bonded H atom of one OH group shifts off the zero level (to x = 0.043) The H_2O molecule, now occupying a general position, is further rotated off the Ca-O5 line. There is also a shift of the O5 atom of H_2O molecule below the zero level (to x = –0.013).

The lattice constants and the cell volume versus temperature are plotted in Fig. 9 [01M1]. The most dramatic changes occur for lattice constant a. Starting at 500 K, the a values decrease smoothly down to 278(5) K. At this temperature, representing the Cmcm-Pmcn transition, the value of a reaches its minimum. Below this temperature, the slope changes and the values a increase more fast down to 240 K. The slopes remain negative down to 110 K. The decrease in the b and c values together with the rather anomalous increase of a was explained by the structural changes at low temperatures. Some thermal expansion coefficients are listed in Table 4.

Studies were performed concerning the mechanisms of phase transitions in lawsonite [95L1, 96C1, 96L2, 00M1, 00S1, 00S2, 01M1]. Two distinct mechanisms may be envisaged for the transitions. In a displacive model, the rotations of H_2O molecules occur as a function of temperature below the transition. In order-disorder transition, the orientation of the water molecule hops between a number of almost fixed positions; the crystal structure observed experimentally is then a dynamic average of the various orientations. For a purely order-disorder transition, the excess entropy of the transition may be calculated directly using configurational mixing modes. In a displacive transition, the excess entropy comes from changes in phonon frequencies associated with the structural changes (see also sections 8.1.2.3.8 and 8.1.2.3.9). The phase transitions, below room temperature, were investigated by using temperature dependent single crystal X-ray structural refinements and single crystal IR experiments [95L1, 96L1]. Their model for the structural transition involved co-operative changes in hydrogen bonding. Thus, the phase transitions in lawsonite were primarily related with proton ordering. The phase transition Cmcm-Pmcn is accompanied by the loss of the – – m mirror plane because of the rotation of both H_2O and OH groups. This transition was monitored by the appearance of C-centering forbidden reflections (h+k = 2n+1) and by nonlinear changes of cell constants and optical birefrigence. Below 155(5) K the space group symmetry is further reduced to $P2_1cn$ accompanied by the loss of the m – – mirror plane because of unidirectional shifts of the x coordinates of the H atoms of the H_2O and OH groups, thus resulting in a polar structure. At elevated temperatures the OH and H_2O groups were constrained by strong librations to occupy sites with high point symmetry. At low temperatures and reduced thermal vibration, the H atoms are allowed to shift towards neighboring O atoms, building up strong hydrogen bonds. Consequently, the H_2O and OH groups are shifted off their highly symmetric position in an ordered fashion, thus lowering the space group symmetry in two steps. Results of polarized FTIR spectroscopy, at different temperatures, provided evidence that the Pmcn to Cmcn transition is not caused by the real rotation of hydroxyl groups and H_2O molecules to static symmetric positions, as drawn in Fig. 8a, but rather by a dynamical and disordered occupation of hydroxyl and H_2O sites around the highly symmetric positions [96L2]. In addition, a single crystal ^1H NMR study also indicates a disordered H sublattice in lawsonite, the single H sites being close to those of the low-temperature Pmcn structure [95G1]. The librational motion of the hydroxyl and H_2O groups was also indicated by the anisotropic displacement parameters of the H atoms. Refinement using the X-ray data [95L1] and neutron data [99L1], at room temperature, revealed that the Hh atoms show an extremely strong anisotropic displacement parameter along [001]. This is in agreement with the Hh libration around the O4 atoms essentially within the (100) plane. As mentioned above, below T_2 the structure changes to the polar space group $P2_1cn$, which is characterized by a loss of the m– – mirror plane - Fig. 8c. The weakly bounded Hwa atoms of the H_2O groups deviate downwards from the former m – – plane, and those of the hydroxyl groups (Hha) deviate upwards.

In order to analyse the phase transition, in [00M1] the temperature dependence of lattice parameters was studied. These show anomalies at 265 K and 130 K. Spontaneous strains, e_i, which represent the lattice distortion undergone as a result of phase transition, were described by a symmetric rank tensor which possesses a symmetry consistent with the point group of the crystal. It is defined to be zero above the transition

temperature and provides a measure of the variations of the order parameter, Q, in the low-symmetry phase, since in first order $e_1 \propto e_2 \propto e_3 \propto Q^2$. To characterize the strains thermodynamically, a tricritical model was used, which includes order parameter saturation at low temperatures. The resulting fits to the data seem to confirm that a tricritical model provides an effective description of the phase transitions - Fig. 10 [00M1]. The tails in e_1 at $T > T_1$ were attributed to precursor effects. The critical temperatures were shown to vary little for the three directions, depending on the fit quality. A value T_1 = 265 K was preferred. Correlations of the strains against each other reveal almost linear relationships. The transition temperature, T_2, was obtained by calculating the difference betwen the dilatation strain data and the tricritical model fits from Fig. 10. Below T_2 = 130(1) K the Δe_i values follow a near perfect straight line. This indicates a second order transition. Changes in frequency, $\Delta\omega$, of IR spectra due to ordering, and changes of the linewidth have been also used to characterize the state of local order [00M1] (see section 8.1.2.3.9). The excess entropy, associated with a displacive phase transition, scales with Q^2 while for a pure order-disorder transition the configurational entropy scales with some function $(1 + Q)\ln(1 + Q) + (1 - Q)\ln(1 - Q)$ [94C1]. Thus, it was suggested [00M1] that the phase transition was in fact driven primarily by some lattice distortion, with a soft mode origin, rather than by proton ordering.

The phase transitions in deuterated lawsonite were investigated with high-resolution, time-of-flight neutron diffraction between 2 and 500 K [01M2]. From the analysis of the spontaneous strains it was shown that the thermodynamics of the phase transition, at 273 K, was not changed by the deuteration process. The spontaneous strains of a deuterated sample are qualitatively the same as those of non-deuterated ones. The squares of the spontaneous strains, e^2_i, vary linearly with temperature, giving a critical temperature T_1 = 273 K. This value is the same as that determined by specific heat measurements [01M1] (section 8.1.2.3.8). As for the nondeuterated sample, the spontaneous strains below T_1 can be described with a Landau model, which implies that a description of the phase transition on an atomic scale must involve displacive components. Shifts in atomic positions with temperature indicate continuous changes from a framework oxygen and for one of the deuterium atoms, whereas for the other deuterium atom, a more discontinuous behaviour was observed in the average structure. Thus, according to [01M2], the mechanism for the Cmcm → Pmcn transition can be understood in terms of proton ordering, but there is also a significant contribution from framework displacements.

The matter of phase transitions in lawsonite was also analysed considering space-group irreducible representations [00S2]. The reciprocal lattice vectors of the conventional Cmcm base-centered unit cell, Γ_0^b, are $\boldsymbol{b}_1$, $\boldsymbol{b}_2$ and $\boldsymbol{b}_3$. The intermediate phase Pmcn belongs to the primitive orthorhombic Bravais-lattice-type, Γ_0, the unit cell of which coincides with the conventional Cmcm unit cell. The transition Cmcm → Pmcn was associated with the instability at the wave vector $\boldsymbol{k}_{15} = (\boldsymbol{b}_1 + \boldsymbol{b}_2)/2$ (in Kovalev's notation [93K1]). The star of the wave vector consists of a single vector and all space-group irreducible representations, in this point of the Brillouin zone, are real and one-dimensional. The order parameter Q_1 for this transition transforms according to the irreducible representation $\boldsymbol{T}_3$. The low-temperature phase transition Pmcm → $P2_1cn$ at T = 120 K can be described in the simplest case as a distortion $P_1(\boldsymbol{k} = 0)$, where P_1 is the x component of polarization vector of the intermediate phase, where the soft mode instability appears in the center of the Brillouin zone ($\boldsymbol{k}_{19} = 0$) associated with the one-dimensional representation $\boldsymbol{T}_4$ of the space group Pmcn.

The crystal structures of lawsonite were investigated at 23, 444 and 538°C and 0.05 and 3.87 GPa [96C1]. The thermal expansions of lattice parameters were also reported [90L1, 95L1, 00M1, 00S2]. The pressure studies show that lawsonite in the above mentioned temperature range, deforms linearly and with an almost isotropic compression - Table 5 [96C1]. The changes that occur with pressure are similar and opposite to those observed as function of temperature. Moreover, the changes induced by the substitution of large ions in the channels are comparable to those induced by heating. The largest variations affect CaO_6 polyhedra, and to a minor extent AlO_6 octahedra. The channels running along $\boldsymbol{b}$ are narrowed by p and widened by T, and the Si–O1–Si angle is reduced and stretched. The thermal behaviour of lawsonite gives indications of the permanence of H_2O molecules in the structure, at atmospheric pressure, up to above 500°C. Moreover, the framework of octahedral-tetrahedral ribbons does not collapse in the H_2O cavity with pressure, but the diameter of the empty spherical void, in which H_2O molecules are hosted decrease by only about 5 % with pressure increase of 28 kbar. The antisymmetric behaviour of lawsonite with T and p shows that, at first approximation, the effects of pressure and temperature are cumulative and so the equation of state for cell-volume variation is $V/V_o = 1 + 3.13(9)10^{-5}\ T - 9.1(3)10^{-4}\ p$, where T is in °C and p in kbar [96C1].

Lawsonite has distinctive acoustic properties being characterized by extremely high shear elastic anisotropy (74 %), a high v_p/v_s ratio (1.94) of acoustic velocities and a large Poisson ratio ($\sigma = 0.318$) [00S1]. Some elastic properties of lawsonite are listed in Table 6.

Hennomartinite

The crystal structure of hennomartinite, $SrMn_2(Si_2O_7)(OH_2)\cdot H_2O$, at $T > 423$ K, was determined to be of lawsonite type having space group Cmcm, where Ca is replaced by Sr and Al by Mn^{3+} [92A1, 93A1]. As discussed above, the Cmcm structure consists of rods of edge sharing Jahn-Teller distorted MnO_6 octahedra that run parallel to [100] and are interconnected by Si_2O_7 groups. The remaining interstices of the framework are occupied by Sr, an H_2O molecule (O5, Hw x 2) and an OH site (O4, Hh), which has twice the multiplicity of O5 (two OH groups per formula unit) - Fig. 11 [96L1]. The atomic positional parameters are given in Table 2.

The low-temperature boundary of the Cmcm phase is 423(5) K. The high-temperature boundary of the twinned $P2_1cn$ phase is 368 K. In the temperature range 368…423 K, in analogy with lawsonite, the average space group Pmcm was proposed [96L1]. For the $P2_1cn$ structure compared with Cmcm one, the Sr, Mn, Si and O atoms show maximum shifts of 0.16 Å (usually parallel to [100]). Thus, as in lawsonite, the principal changes of the structure were related to shifts of the H atoms and their effects on neighboring atoms. The coordination polyhedra around Sr, Mn and Si are the same as in the Cmcm structure, except that they are slightly more distorted than in the Cmcm structure. Even, the Jahn-Teller distortion of the MnO_6 octahedra is similar in both structure types. Although the H atoms are on special positions (mirror plane m – – at $x = 0$) and are symmetrically related (mirror plane – – m at $z = 0.25$) in the Cmcm structure, in the $P2_1cn$ one the H positions split by rotation within the (100) plane into Hw-Hw1 and Hh-Hh1 sites. Moreover, one H atom (Hw) of the H_2O molecule shifts considerably below m – – ($x = –0.15$; –0.94 Å). The other one (Hw1) remains close to that plane ($x = –0.02$; –0.12 Å). Because of the decrease of the x coordinate of the Hw atom, the O atom of the H_2O molecule (O5) also shifts in the x direction below zero level ($x = –0.025$; –0.16 Å) - Table 2. Compared with the Cmcm structure, some hydrogen bonds are strenghtened (Hw1L ... O4; Hw1R...O5), whereas others are weakened (Hw...O1). According to [96L1] the differences between L and R H atoms are probably caused by a simple disorder model (involving only the H atoms). The H atom (Hh) of one hydroxide group also shifts considerably below the zero level ($x = –0.09$; –0.56 Å). The second H atom (Hh1) remains close to the zero plane ($x = 0.03$; 0.19 Å) enhancing the former Cmcm hydrogen bond (Hh ... O4'), namely (Hh1L...O4) and (Hh1R...O4). The Hh atoms exhibits additional long hydrogen bonds (HhL...O5) and (HhR...O5).

In the $P2_1n$ structure of lawsonite, at 110 K, Hw shifts below and Hh shifts above the zero level [95L1], opposite to hennomartinite, but the general tendency to enhance the hydrogen bond system, at low temperatures, is common to both silicates. The shift of the H atoms was attributed [96L1] to the reduced thermal libration, which constrained the H_2O molecules and OH groups to occupy highly symmetric positions in the interstitial "cavities" of the Cmcm structure. When thermal vibration is reduced, the cavities of the structure become oversized and the OH groups and H_2O molecules are attached by hydrogen bonds to the walls of the cavities.

After one heating and cooling cycle, below ~ 373 K, it was shown that the true, relaxed room temperature structure represents a monoclinic derivative of the natural, initially determined $P2_1cn$ average structure [96L1]. Moreover, a decrease of the unit-cell parameters (particularly a) and the unit-cell volume of hennomartinite during the 518 K data collection, suggests a temperature controlled structural evolution of hennomartinite from disorder and small twin domains in the natural phase, to large twin domains caused by annealing at elevated temperatures. In contrast to lawsonite [95L1], a non-linear change in the unit-cell parameters at the phase boundaries was not observed [96L1] - Fig. 12.

$NaBa_3[Si_2O_7](OH)$

The silicate crystallizes in a hexagonal lattice having space group $P6_3/mmc$, $P6_3mc$ or $P62c$ [71F1].

8.1.2.3.2 Neutron diffraction data

Ilvaite

The magnetic structure derived from powder neutron diffraction consists of A site ribbons composed of two single ferromagnetic (Fe^{2+}-Fe^{3+}-Fe^{2+}-Fe^{3+}...) chains whose spins are aligned antiparallel to each other, below T_N = 123 K - Fig. 13 [84G1, 90G1]. The Fe^{2+}(B) spins are weakly coupled to their A site neighbors and are mostly ordered below 50 K - Fig. 14. Both A and B site spins are nearly parallel and antiparallel to ***b*** - Table 7. Below 123 K, the Fe^{2+}(A) and Fe^{3+}(A) moments increase rapidly with decreasing temperature showing a sudden increase at ≅ 50 K indicating a second transition, whereas Fe^{2+}(B) moments increase slowly below 123 K, with a substantial increase at $T \cong 50$ K. The components of the moments along *x*, *y* and *z*-axes are given in Table 7. The resultant moments extrapolated to 0 K are 3.6, 4.6 and 3.6 μ_B for Fe^{2+}(A), Fe^{3+}(A) and Fe^{2+}(B) sites, respectively. The difference in the thermal evolution of the magnetic moments, at A and B sites, is due to the frustration of Fe^{2+}(B) spins. Whereas Fe^{2+}(A) and Fe^{3+}(A) ions alternate and form chains parallel to ***c***-axis, Fe^{2+}(B) ions occur at the apices of nearly square pyramids, the bases of which are formed by a pair each of Fe^{2+}(A) and Fe^{3+}(A) ions - Fig. 13b. Within one square pyramid, the Fe^{2+}(B) ion at the apex is slightly displaced from the center and is closer to one of the two Fe^{2+}(A) - Fe^{3+}(A) pairs. Since Fe^{2+}(B) occurs on a triangular lattice with respect to the two neighboring Fe^{2+}(A) - Fe^{3+}(A) pairs on either side, it simultaneously senses spins parallel (+) and antiparallel (-) to the ***b***-axis, thereby causing spin frustration. But finally the ferromagnetic interaction of Fe^{2+}(B) with the closer of the two A chains wins out, and long range spin correlation sets in below 50 K [90G1]. Due to the presence of considerable fluctuation of Fe^{2+}(B) spins between 50 K and 123 K, the second transition is smeared out, explaining broad peaks below 50 K observed in magnetic susceptibility [84C1, 87G2] and specific heat measurements [88R1]. Alternatively, the smeared transition could result from impurities, particularly Mn^{2+} at the Fe^{2+}(B) site in the natural sample.

8.1.2.3.3 Magnetization and magnetic susceptibilities

Ilvaite

In addition to structural transitions, ilvaites show two magnetic transitions at T_N [74B1, 79Y1, 84C1] and ~ 40 K [84C1, 84G2]. The T_N temperatures determined by various authors are in the range 116 K and 128 K - Table 8.

The magnetization curves of ilvaites are linear up to 6 T [79Y1, 84C1]. The greatest magnetization that can be induced in a field of 6 T applied parallel to ***c*** is only 9 % of the collinear saturation value, showing the presence of strong antiferromagnetic interactions [84C1].

The temperature dependences of the reciprocal susceptibilities of polycrystalline samples show a Curie-Weiss-type behaviour above 140…150 K [79Y1, 84C1]. The magnetic susceptibilities of powder ilvaite $<\chi>$and of a single crystal with the field applied parallel ($\chi_{\parallel}$) and perpendicular ($\chi_{\perp}$) to the ***c***-axis was also studied [84C1]. An antiferromagnetic-type ordering was observed below T_N = 118(4) K, but $<\chi>$ shows a ferromagnetic increase below T_N. The Curie constant was nearly twice that expected from the free ion Curie constants of the constituent ions $C \cong 11$ emu K/f.u. - Table 8, thereby suggesting that there were also ferromagnetic pair correlations in the studied temperature range ($140 \leq T \leq 350$ K). Around 40 K, $\chi_{\perp}$ exhibited a peak (see section 8.1.2.3.2). Later on [87G2], the thermal variations of magnetic susceptibilities for different crystallographic planes and directions have been studied in the temperature range 21…400 K - Fig. 15. Below 343(1) K a continuous rotation of the molar susceptibility $\chi_{\parallel}$ in the (*ab*) plane down to 90(2) K was observed where the symmetry of magnetic ellipsoid remains unchanged. The susceptibilities along ***a***, ***b*** and ***c***-axes (χ_a, χ_b, χ_c) increase abruptly below 123.0(5) K although antiferromagnetic ordering of Fe^{2+} and Fe^{3+} spins on A sites was evidenced by neutron diffraction study. In addition χ_a^{-1} shows a maximum characteristic for antiferromagnetic ordering at 50(3) K, whereas χ_b^{-1}, χ_c^{-1}, first increase sharply below 123 K, followed by a curvature characteristic to antiferromagnetic ordering in the lowest temperature region. This behaviour was attributed to the antiferromagnetic ordering of Fe^{2+} spins in the B site. According to [87G2] the magnetic data suggest charge delocalization effects between adjacent Fe^{2+}(A)-Fe^{3+}(A) pairs not only along ***c*** but also along ***a*** and ***b*** directions. The negative signs of the molar susceptibility anisotropy ($\chi_{\parallel} - \chi_{\perp}$) suggests a singlet ground state $^5A_1$ for the Fe^{2+} ions. A strong anisotropic exchange interaction between adjacent iron ions in the double chain, possibly

due to electron delocalization effects, seems to be responsible for high Θ values and rotation of the magnetic ellipsoid [87G2] - Table 8.

$Ca\,Fe^{2+}_{2-x}\,Mn^{2+}_{x}\,Fe^{3+}Si_2O_7OOH$

The effects of manganese impurities on the magnetic properties of ilvaite were studied [93B1]. For a Mn^{2+} content of 0.5 wt %, the low-temperature magnetic phase transition is at ~ 40 K, for a Mn^{2+} content of 1.2 wt % the transition temperature is less than 20 K and for a Mn^{2+} content of 4.5 wt % the transition appears to be well below 10 K.

8.1.2.3.4 Nuclear gamma resonance (NGR) data

Ilvaite

The ilvaites were intensively investigated by the ^{57}Fe NGR method [69H1, 71B2, 71G1, 75G2, 77H1, 77P1, 78A1, 79N1, 79Y1, 80E1, 84C1, 84L1, 87G2, 88X1, 92G1, 92L1, 94D1, 95C1]. These studies have in view mainly the analysis of magnetic properties, iron distribution and electron delocalization between the Fe^{2+} and Fe^{3+} ions in octahedral A sites.

The iron distribution as determined by diffraction studies, namely from Fe–O distances was confirmed by ^{57}Fe NGR [69H1, 71G1]. In addition, evidence for a mixed valent state of iron due to thermally activated electron hopping between Fe^{2+} and Fe^{3+} at the 8d sites has been reported [71G1, 77H1, 78A1, 79N1, 80E1]. All these agreed on an averaged hyperfine interaction of the Fe-ions at the 8d sites above 400 K, resulting in one quadrupole split doublet with averaged parameters in the ^{57}Fe NGR spectra. Some discrepancies between the different studies concerning the formation of this mixed valence state resulted from different evaluations of the temperature dependent ^{57}Fe NGR spectra using lorentzian lines. These could be overcome by applying a fitting procedure which considered the temperature dependent relaxation frequency of the electron exchange process [84L1]. By using this model in [84L1] an activation energy for electron hopping E_a = 0.11 eV was evaluated. This is in good agreemnt with electrical conductivity measurements (0.24 eV [75G1, 75G2], 0.15 eV [77H1], 0.13 eV [84C1]) - see section 8.1.2.3.7. Some hyperfine parameters are listed in Table 9. A pseudo-tetragonal symmetry was detected from ^{57}Fe NGR at ferrous iron sites with a lowest orbital singlet $^5A_1$ ground level [84C1].

The spectra, below 90 K, were fitted with three magnetic patterns: Fe^{3+}(A), Fe^{2+}(A), and Fe^{2+}(B). According to [88X1], within the 113…117 K range, due to the relaxation effects or sample inhomogeneity, the paramagnetic and magnetic patterns overlap so strongly that no satisfactory fit could be made. In order to derive the Fe^{2+}/Fe^{3+} ratio, ^{57}Fe NGR spectra of natural ilvaite were studied at T = 121 K [98S1]. At this temperature, according to [98S1], a negligible electron transfer may occur between Fe^{2+}-Fe^{3+} pairs on A sites. The spectrum was fitted with three doublets arising from A-site (Fe^{2+}(A), Fe^{3+}(A)) and B-site (Fe^{2+}(B)) - Table 9.We note that although the hyperfine parameters determined at 4.2 K are similar, the site assignments by different authors were different. Thus, in [88X1] the site assignment of Fe^{2+}(A), and Fe^{2+}(B) were switched comparatively to those reported by [84C1, 95C1].

At low temperatures, the continuous charge localisation between Fe^{2+} and Fe^{3+} ions in octahedral A sites causes the Fe^{2+}-Fe^{3+} interaction to be ferromagnetic, although the overall magnetic order is antiferromagnetic. The hyperfine fields at Fe^{2+}(A) and Fe^{3+} (A) sites follow a relation of the form $B_{hf} = B_{hf,0}\,(1 - T/T_N)^{\beta}$ with β = 0.17, T_N = 116.0(1) K and $B_{hf,0}$ = 32.8 T and 52.3 T, respectively, at 0 K [88X1]. A value $B_{hf,0}$ = 18.6 T was evidenced for the Fe^{2+}(B) site. Similar, as for magnetic moments, the ^{57}Fe hyperfine field for Fe^{2+}(B) shows a sudden decrease at temperature $T \approx$ 36 K - Fig. 16a.

The temperature dependences of the isomer shifts and quadrupole splitting suggest also the presence of two magnetic transitions although they are not as sensitive as B_{hf} values - Fig. 16b,c. The electric field gradient (EFG), asymmetry parameter, η and angle θ between V_{zz} and B_{hf} show that the magnetic transition may be accompanied by a significant change in the distortion of the octahedra, particularly Fe^{2+}(B), at about 36 K. This is the result of a magnetostriction effect. Such an effect, at 123 K, has been found from the study of unit cell dimensions down to 95 K [88G1].

The thermal characteristics of magnetic susceptibilities and their anisotropies of ilvaite single crystals have been analysed in the light of ligand field theory [90K1]. The electronic energy pattern and the corresponding

wave functions were obtained from best fitting of the experimental results with the corresponding theoretical values. These results were used to calculate the thermal characteristic of the quadrupole splittings. The ΔQ values are reasonable close to those reported from ^{57}Fe NGR studies [79N1, 84C1, 84L1]. The analysis suggests appreciable molecular overlap between the orbits of the ligand electrons and those of the Fe^{2+} ions, the overlap being prominent along the chain direction as also observed from electrical conductivity measurements.

Above the magnetic transition temperatures, T_N, the spectra were analysed considering the presence of two up to four doublets. Thus, for example in [71G1], in the temperature range 240 K…350 K, the spectra were analysed on the basis of three doublets. In the 350 K…520 K range only two doublets were observed. This was attributed to the presence of an electron hopping mechanism. The relaxation model has been also used to explain ^{57}Fe NGR spectra of the ilvaite within the range 298 K and 455 K and to evaluate the activation energy for electron hopping [84L1]. Thermally activated electron delocalization between Fe^{2+} and Fe^{3+} occurs if Fe^{2+} and Fe^{3+} occupy crystallographically equivalent or geometrical very similar neighboring sites which share common edges to form extended structural units.

Since the increase of temperature leads to an increase of the electron exchange rate between Fe^{2+}(A) and Fe^{3+}(A), the lifetime of Fe^{2+}(A) and Fe^{3+}(A) at high temperatures will be short, and ^{57}Fe NGR spectra will correspond to the weighted average of those for Fe^{2+} and Fe^{3+} [92L1]. From Table 9 it can be seen that δ and ΔQ for Fe^{2+}-Fe^{3+} doublets are quite unusual, too high for Fe^{3+} but too low for Fe^{2+} in octahedra within the range of 473 K to 673 K. The ratios Fe^{2+}(B) doublet area to Fe^{2+}-Fe^{3+} doublet area are approximately equal to 1/2. This value corresponds to the ratio of the number of iron in A sites to that from B sites. Therefore, the doublets with δ = 0.57…0.66 mm/s and ΔQ = 1.31…1.40 mm/s were ascribed to the mixed valence state of iron ions on A sites [92L1]. The increase of temperature leads to a narrowed linewidth of Fe^{2+}-Fe^{3+} doublets. This suggests that the lifetime of Fe^{2+} and Fe^{3+} doublet on A sites, at high temperatures, is so short that ^{57}Fe NGR spectra show sharp lines.

According to [80E1] four partially resolved patterns were required to account for the spectra of polycrystalline ilvaites at 298 K and pressures up to 6 GPa - Table 9. These were assigned to: (a) "Fe^{3+}-like" ions on A site for which the electron density at the nucleus decreases modestly with increasing pressure and temperature, (b) "Fe^{2+}-like" ions on A site which with increasing temperature and pressure become progressively more ferric-like, (c) well defined Fe^{2+} ions on the B site throughout the temperature and pressure range investigated, (d) a component of a relaxation spectrum due to electron exchange between Fe^{2+} and Fe^{3+} ions on the A lattice sites. There is generally a decrease with increasing pressure or temperature of the apparent quadrupole splitting and isomer shift of the "Fe^{2+}(A)-like" subpattern and a little increase of the quadrupole splitting and isomer shift of the "Fe^{3+}-like" subpattern. These coupled changes in the spectrum lead to a coalescence of these two patterns at temperatures above 350 K, at 0.1 kPa pressure, and at 298 K and pressures above 2.8 GPa and 6 GPa, respectively, for a single crystal (001) platelet and either (100) or (010) platelets, or polycrystalline samples. According to [80E1] the electron delocalization in ilvaite can be understood in terms of two distinguishable but connected processes. One is the electron exchange between Fe^{2+} and Fe^{3+} ions resulting in a mixing of Fe^{2+} and Fe^{3+} states to the extent of only 5…15 %. The other electron delocalization process involves primarily Fe^{2+} (A) ions in such a way that they become more Fe^{3+} like with increasing pressure and temperature, that is to say a process $Fe^{2+} \rightarrow Fe^{3+} + e^-$. In this process the e^- is intrinsically delocalized and does not occupy another localized state.

$Ca\,Fe^{2+}_{2-x}\,Mn^{2+}_{x}\,Fe^{3+}Si_2O_7O(OH)$, $Ca\,Fe^{2+}_{2}\,Fe^{3+}_{1-x}\,Al_xSi_2O_7O(OH)$

In [95C1] the Mn- and Al-doped ilvaites were analysed by ^{57}Fe NGR. The ^{57}Fe hyperfine field value for the Fe^{2+}(A) site in $Ca\,Fe^{2+}_{2-x}\,Mn_xFe^{3+}Si_2O_7O(OH)$ is reduced, this fact being connected with an incompletely developed moment due to completely planar anisotropy and exchange. The angle θ between B_{hf} and the EFG principal axis system increase from about 14° at 4 K to 45° at 110 K for Fe^{2+}(A) and from 43° at 4 K to 52° at 110 K for Fe^{3+}(A) (θ = 56° may also mean random orientation). Thus, there is a severe canting of moments which is related to the temperature dependent competition between the exchange interaction and anisotropy. In $Ca\,Fe^{2+}_{2-x}\,Mn_xFe^{3+}Si_2O_7O(OH)$, with $x \leq 0.19$ the θ and B_{hf} values are almost independent of Mn concentration [95C1] - Table 9.

The relaxation rates, λ, were evaluated in $Ca\,Fe^{2+}_{2-x}\,Mn^{2+}_{x}\,Fe^{3+}Si_2O_7O(OH)$, in the temperature range 295 K…450 K [92G1]. Two activation energies E_{a1} and E_{a2} were determined in different temperature ranges - Fig. 17 and Table 10. This is in contrast with [84L1] where only one relaxation rate was obtained. The activation energies E_{a1} = (0.10…0.25) eV were attributed to the process of thermally activated intersite electron hopping between Fe^{2+} and Fe^{3+} at the (A) sites. The second activation energy, E_{a2}, is higher than E_{a1}. This behaviour was interpreted by a narrow d-band or polaron band which is filled at higher temperatures. The (A) pattern with the averaged hyperfine parameters at high temperatures was attributed to this narrow band mechanism with delocalized electrons. The temperature at which there is a change of slope decreases with increasing Mn content and follows the trend evidenced for the crystallographic transition temperature, T_t. The Mn^{2+} ions are mainly incorporated into the double octahedron chains. Consequently, they increase the disorder in these chains (A sites or 8d sites) and therefore favour the tendency for the formation of the orthorhombic phase. A narrow band can only be formed in the orthorhombic phase with crystallographically equivalent (A) sites. For localized hopping which is slow enough, the monoclinic lattice can "follow" the electron jumps by changing bonding angles and distances. At higher temperatures this is not possible any more. The orthorhombic phase has to form and the electron delocalization via a narrow d-band mechanism becomes the dominant process. In contrast to samples having x = 0 and 0.12, for x = 0.19 the starting temperature for the second mechanism, evidenced by a change in slope, is larger than T_t. This shows that the band mechanism does not become operative directly at the monoclinic to orthorhombic phase transition at 300 K but still needs a certain thermal activation.

The relaxation has been further studied also, at low temperatures, in Mn- and Al-doped synthetic ilvaites [95C1]. In $Ca\,Fe^{2+}_{2-x}\,Mn^{2+}_{x}\,Fe^{3+}Si_2O_7O(OH)$, between 50 K and 120 K the ^{57}Fe spectral lineshapes can be described by relaxation due to spin rotation. The relaxation rate between ~ 80…120 K can be fitted to $\exp(-E_a/k_BT)$ - Fig. 18 [95C1]. The thermal activation energy increases from 0.018 eV (x = 0) to 0.023 eV (x = 0.19). Electron spin correlation times in the above samples have been also determined from muon spin relaxation (μSR) experiments in natural ilvaite [94D1]. The activation energy $E_a \cong 0.017$ eV obtained from μSR data agrees with the values obtained by ^{57}Fe NGR data. This dynamics was attributed to the movement of wide domain walls along the ferromagnetic chains. Both, ^{57}Fe NGR and μSR data, show a levelling off of relaxation rates, below about 80 K, where the antiferromagnetic coupling between chains becomes dominant. Even at the lowest temperatures the rotational spin dynamics is, however, not frozen as can be traced from μSR [94D1]. This behaviour was related to the ground state anisotropy of Fe^{2+}(A). The enhancement of relaxation rates values for the sample with x = 0.19 as compared to that with x = 0.0, at low temperatures, was probably caused by a static distribution of the hyperfine fields due to doping. Irrespective of this problem, the dynamics above 80 K is faster for the Mn doped samples as may be explained in part by a smaller anisotropy. The enhanced activation energy, however, results from the antiferromagnetic Fe^{3+}-Mn^{2+} coupling introduced into the ferromagnetic chains.

For $Ca\,Fe^{2+}_{2}\,Fe^{2+}_{1-x}\,Al_xSi_2O_7O(OH)$ silicates with $0.0 < x \leq 0.20$ an onset of magnetic splitting is observed below ~ 120 K [95C1]. In contrast to Mn-doped samples, the hyperfine patterns show the presence of both, magnetically ordered and still paramagnetic regions. The paramagnetic fraction increases with increased Al-doping. As seen in Fig. 19, for the sample with x = 0.20, the ordered fraction increases with decreasing temperature. This behaviour was interpreted as due to gradual freezing of superparamagnetic regions in the ferromagnetic chains caused by the breaking of the ferromagnetic coupling by aluminium. The ^{57}Fe hyperfine field and the angle θ between B_{hf} and the EFG principal axis for different iron sites in the magnetically ordered region are almost independent on aluminium content.

8.1.2.3.5 Nuclear magnetic resonance (NMR) data

The data obtained by ^{29}Si MAS NMR spectroscopy in lawsonite are listed in Table 11.

8.1.2.3.6 Dielectric properties

Lawsonite

The temperature dependence of the dielectric constant $\varepsilon_a = \varepsilon_{11}$, measured along the [100] direction, shows an anomalous peak at about 120 K - Fig. 20. Below 120 K a hysteresis loop is observed showing that the $P2_1cn$ phase is proper ferroelectric [00S2]. Consistently, the dielectric constant ε_a increased (by a factor of 7) when approaching T_2 from both sides. The ε_a^{-1} values vary linearly with temperature above and below T_2, except in the close vicinity of T_2, as characteristic for a proper ferroelectric. The ratio of slopes $\varepsilon_a^{-1}(T>T_2)/\varepsilon_a^{-1}(T<T_2)$ is 1:1.25 and deviates from the value predicted by the Landau-Ginzburgh theory (1:2). This deviation was explained in terms of a contribution of ferroelectric domain-wall motion to the permittivity below T_2. The characteristic relaxation time of the domain-wall motion was $\tau_D < 10^{-7}$ s. The domain walls were mobile down to the lowest measured temperature, $T = 80$ K [00S2].

8.1.2.3.7 Electrical resistivity

Ilvaite

Electrical *dc* resistivity on a natural ilvaite single crystal (Elba, Italy), of unspecified composition, along the [001] axis yielded a conductivity σ (300 K) = $3\cdot10^{-6}$ $(\Omega\text{cm})^{-1}$, while σ shows a slightly lower value when perpendicular to [001] [84C1]. A semiconducting behaviour described by the relation $\sigma = \sigma_o \exp(-E_a/k_B T)$ was evidenced. Three temperature ranges were distinguished between 200 and 460 K with activation energies E_a = 0.13 eV ($T \le 300$ K), E_a = 0.36 eV (300 K $\le T \le$ 415 K) and E_a = 0.67 eV (415 K $\le T \le$ 460 K). These were associated with $Fe^{2+}(A) \rightarrow Fe^{3+}(A)$, $Fe^{2+}(B) \rightarrow Fe^{3+}(A)$ and $3d^6 \rightarrow 3d^5 4s$ electron transfer, respectively. For other ilvaite crystals, conductivity experiments lead to an activation energy E_a = 0.5 eV at higher temperature [71G1] and 0.15 eV close to 300 K [77H1]. Later on, the electrical resistivity of ilvaite having the composition $\langle Ca_{0.997}\rangle\{(Fe^{2+},Fe^{3+})_{2.877}Mg^{2+}_{0.016}Mn^{2+}_{0.060}Al_{0.047}\}[Si_{1.996}Al_{0.004}]O_8(OH)$ was studied [98S1]. The $\log\sigma^{ac}_{dc}$ versus T^{-1} values where σ^{ac}_{dc} are the conductivities deduced from the real part of impedance by extrapolating towards frequency $\omega/2\pi \rightarrow 0$, are plotted in Fig. 21a. A bending curve is seen that can be approximated by two straight lines in the high- and low-temperature ranges with different slopes that can be described by the exponential relation given above. According to [98S1], the slopes arise from two different kinds of semiconducting charge transport mechanisms. From these data, for 160 K $\le T \le$ 270 K, E_a = 0.41(3) eV and in the range 270 K $\le T \le$ 300 K, a lower value, E_a = 0.29(3) eV was obtained. The resistivity at 300 K is by 10^3 higher than that observed for a natural ilvaite crystal for which no composition was given [84C1]. The activation energies reported by [98S1] are far above E_a = 0.13…0.14 eV found for $T <$ 300 K by [84C1]. The dc conductivity was $1.8\cdot10^{-3}$ $(\Omega\text{cm})^{-1}$ at 300 K, measured parallel (||) to the [001] direction. Perpendicular ($\perp$) to [001] it was $1.4\cdot10^{-5}$ $(\Omega\text{ cm})^{-1}$, i.e. the conductivity is highly anisotropic.

The results of thermopower measurements, S, - Fig. 21b - show that S values are positive, pointing to p-type conduction, and is comparatively low. There is a decrease of the values obtained parallel to [001] towards higher temperatures, up to 450 K, where S appears to tend a value $S = 11\,\mu V/K$ [98S1]. For measurements perpendicular to [001] direction, the S values are negative. The above data indicate two different conduction mechanisms for measurements $\parallel$ and $\perp$ to [001].

The analysis of the resistivity data suggests that the conduction is effected by a hopping charge transport between localized levels in the energy gap, associated with activation energies E_a = 0.3…0.5 eV. The impurities (Mg, Al, Mn) may play a decisive role in the charge hopping transport $\parallel$ [001] that is basically governed by Fe^{2+}-Fe^{3+} pairs on the A-site of the lattice as the source of electrons. Although the E_a values were similar for both measured directions, the sign of termopower is different which points to different charge transfer mechanisms. The bulk *dc* conductivity σ^{ac}_{dc} for measurements $\parallel$ [001], obtained by extrapolation of *ac* data using impedance spectroscopy, could only be determined at $T <$ 300 K owing to the sample-electrode interfacial effects. The bulk σ^{ac}_{dc} conductivity $\perp$ [001] showed a slight break at $\cong$ 380 K that may reflect the structural phase transition monoclinic-orthorhombic at $T_1 \cong$ 345 K. From *ac* conductivity measurements, in the frequency range 20 Hz…1 MHz, at $T <$ 300 K, a dispersive character of electronic relaxation was found, resembling that of amorphous

semiconductors and of impurity conduction in crystalline semiconductors where it was ascribed to charge hopping processes of electrons between localized levels of cation pairs of clusters of limited lengths.

8.1.2.3.8 Heat capacity

Ilvaite

Specific heat measurements were performed on $Ca_{0.98}Mn_{0.021}Fe_{2.97}Al_{0.026}(Si_{1.99}O_7)O(OH)$ ilvaite [88R1] - Fig. 22a-c. A peak in C_p was found at T_N = 121.9(5) K corresponding to the magnetic transition. Between 10 and 40 K, the heat capacity curve exhibits an anomalous curvature but no sharp peak indicative of cooperative ordering. The lack of sharp peak in C_p near 40 K may be a consequence of the weak interactions between the Fe^{2+} ions on B sites. If the exchange interactions between the Fe^{2+} ions on the B sites are less than the energy separation between the spin states of the Fe^{2+}, the result will be a broad hump in C_p (Schottky anomaly) [77C1]. The C_p values obtained in the temperature range $300 < T < 500$ K (except for the sample heated at 750 K prior to the measurements) show a "hump" at ~ 375 K which was associated with the electron localization. As seen from Fig. 22d, the excess C_p shows that charge localisation begins at 450 K, the major part of charge localising at 375 K. As evidenced by ^{57}Fe NGR, the onset of charge localisation has been found at ~ 470 K [88X1]. With the onset of charge localisation (~ 470 K) fluctuating precursor clusters of the low-temperature phase (with a high degree of short-range order) begin to form within the high-temperature phase. The correlation length (size of the clusters) increases with decreasing temperature and finally long-range order sets in at around 380 K which coincides with the peak in C_p. Below 380 K two regimes were distinguished. The first, between 380 K and T_t = 346 K with a long time scale; the charge localisation increases slowly as $T \rightarrow T_t$. Within the second regime between T_t and 310 K, with a short time scale, the charge localisation increases rapidly with decrease in temperature. In the region ($5 < T < 310$ K) another mechanism is operative. It is possible that within the third regime the impurities, particularly Al^{3+} ions in the A sites present further growth of the ordered domains, where the charge localisation takes place via a much longer superexchange path such as Fe–O–Si–O–Fe, thus slowing down the rate of charge localisation considerably [89G2]. From the difference in energy between the ground and excited state(s), at $T \cong 375$ K, an activation energy of 0.077 eV was estimated [88R1].

Lawsonite

The specific heat of $Ca_{1.00}Al_{1.95}Fe_{0.05}Si_{2.00}O_7(OH)_2 \cdot H_2O$ lawsonite, as function of temperature, is shown in Fig. 23a. [01M1]. The data of [80P1], which were obtained on a natural (95 % pure) lawsonite, are also plotted. The specific heat anomaly in lawsonite has two parts. There is a distinct change in $C_p(T)$ slope at ≅ 295 K, which is evidence for a pronounced tail in the heat capacity anomaly above T_1. At the transition temperature, a distinct peak was shown, but the magnitude of this peak varies greatly between experimental runs - Fig. 23b. In particular, the peak is far more pronounced when the sample is heated than when it is cooled. The magnitude of the total excess entropy associated with this transition is not reproducible, varying in the range 5.93…6.24 $JK^{-1}mol^{-1}$ [01M1]. On heating, the specific heat anomaly is consistent with a tricritical phase transition. However, on cooling significant hysteresis is observed and the form of the C_p anomaly is quite different. In all measurements extensive pre-transitional effects were observed above T_1 . An anomaly associated with the Pmcn-$P2_1cn$ phase transition was also observed [80P1] - Fig. 23c. The excess entropy associated with this transition is 6(1) $JK^{-1}mol^{-1}$. The above data were interpreted as showing that both transitions are caused by the interaction of proton ordering and displacive changes in the aluminosilicate framework. The standard entropy, at 298 K, was calculated, incorporating the effects of the two transitions [01M1]. Two methods were used for this calculation giving values S^0_{298} = 233.27 and 234.96 $JK^{-1}mol^{-1}$, respectively.

8.1.2.3.9 Optical properties

Ilvaite

The optical absorption spectrum of ilvaite, at room temperature, is given in Fig. 24 [89G3]. A strong pleochroism was found exhibiting the main absorption parallel to the crystallographic ***c***-axis, which coincides with the polymerization direction of the Fe-O octahedral double chains [84A1, 89G3]. The shapes of the spectra perpendicular to the ***c***-axis (***E*** || ***a***, ***E*** || ***b***) are characterized by an exponential increase towards the ligand-metal charge transfer (LMCT) transitions at energies above 38000 cm^{-1} [85S1]. The feature is overlain by a broad shoulder at ≈ 13000 cm^{-1} (***E*** || ***a***) and a more pronounced shoulder around 12000 cm^{-1} (***E*** || ***b***) which were presumably related to the intervalence charge transfer between the double chains or between 8d and 4c sites [89G3]. An additional shoulder near 20000 cm^{-1} has been observed for ***E*** || ***b*** which may be related to pair excitations of adjacent Fe^{3+} in 8d sites [85S2]. The absorption coefficient for ***E*** || ***c*** also exhibits an increase towards the LMCT transition as a brackground feature. This is superimposed by an edge-like absorption feature between 4000 and 7000 cm^{-1} and a broad asymmetric band at higher wave numbers. The maximum absorption coefficient is around 14500 cm^{-1}. The minimum absorption coefficient in this window is higher than the absorption coefficient for ***E*** || ***a*** and ***E*** || ***b*** at the same frequency. The absorption feature for ***E*** || ***c*** is mainly related to intervalence charge transfer (IVCT) along the polymerization axis of the Fe-octahedral chains, but additional contribution have to be considered [89G3]. The polymerization of the Fe–O octahedra, however, causes strong coupling between Fe^{2+} and Fe^{3+} along the ***c***-axis. which can result in additional absorption features polarized parallel to the Fe^{2+}-Fe^{3+} vector. They are then caused by the spin allowed Fe^{2+}: $^5T_{2g} \rightarrow {}^5E_g$ ligand field transition [84A1, 89G3]. Additional absorption intensities, at frequencies lower than 10570 cm^{-1}, were tentatively explained by transition probabilities of polaronic states at configurational coordinates q smaller than the equilibrium value. Heating the sample to 450 K results in continuously increasing absorption coefficients between 4000 cm^{-1} and 15000 cm^{-1} (***E*** || ***a***) with a shoulder around 8000 cm^{-1}. This was interpreted as being due to increasing IVTC (or localized polar hopping) transition probabilities perpendicular to ***c*** caused by a continuously decreasing Fe^{2+}-Fe^{3+} order [89G3]. Increasing absorption intensities between 4000 and 5000 cm^{-1} were found for ***E*** || ***c***, whereas the absorption coefficient at higher energies remains unchanged.

The IR absorption spectra of ilvaite were analysed [77P1, 89G3]. In [89G3] fourteen phonon bands, were recognized in the frequency range 400 cm^{-1} to 1100 cm^{-1} in polarized single crystal spectra - Fig. 25 - or in powder spectra at: 1035 (B_{3u}); 984 (B_{2u} or B_{3u}); 966 (B_{1u}); 954 (B_{1u}); 907 (B_{2u} or B_{3u}); 859 (B_{3u}); 822 (B_{1u}); 706 (B_{3u}); 638 (B_{2u}); 571; 539; 495; 457; 431. We note that in ilvaite the expected optically active modes are: $27A_g$ $+27B_{1g} + 18B_{2g} + 18B_{3g}$ (Raman active) + $17B_{1u} + 26B_{2u} + 26B_{3u}$ (infrared active).

Heating to 425 K results in increasing absorption coefficients between 1500 cm^{-1} and 4000 cm^{-1} (for ***E*** || ***c***) with increasing intensity towards higher energies. This feature was considered to be also responsible for increasing intensities in optical spectroscopy between 4000…5500 cm^{-1} (***E*** || ***c***) during heating [89G3] and was related to vibronic effects.

The above data show the presence of a phase transition near 335 K which follows the Landau theory, the local behaviour as measured by spectroscopy shows a continuous behaviour with large short range order at temperatures above the transition point. The strong pleochroic effect of the absorption coefficient gives evidence that the one-dimensional character of ilvaite is reflected in its electronic properties. The lack of any Drude absorption in the high-temperature phase of ilvaite with ***E*** || ***c*** is an obvious consequence of this effect [89G3]. Thus, it was concluded that effects of the electronic ordering process of ilvaite have to be treated in terms of a perturbation of localized electron states.

Lawsonite

According to atomic positions and symmetries for Ccmm-type structures, the following representations of the 114 modes were expected: $\Gamma = 16\ A_g + 11\ B_{1g} + 16\ B_{2g} + 8\ B_{3g}$ (Raman active)+ $18\ B_{1u} + 13\ B_{2u} + 18\ B_{3u}$ (IR active) + $1\ B_{1u} + 1\ B_{2u} + 1\ B_{3u}$ (acoustic) + $11\ A_u$ (inactive) [90L1].

The ambient pressure IR spectra of lawsonite have been studied by [74L1, 90L1, 96L2, 99S1]. In [74L1] was carried out an IR study of the vibrations of OH and H_2O in lawsonite and they have resolved the high-frequency region (> 1600 cm^{-1}) and assigned the band as follows: bending of water molecules, at 1620 cm^{-1} (δ, B_{3u}); symmetric stretching of water molecule at 3250 cm^{-1} (ν_s, B_{3u}); antisymmetric stretching of water molecules at

3070 cm^{-1} (ν_{as}, B_{1u}); stretching of hydroxyl groups at 3560 cm^{-1} (ν, B_{1u} and B_{3u}). In [90L1] was mentioned that in powder spectra only half of the expected bands were found. The obtained spectrum was in agreement with those reported by [74L1]. In [96L2] the assignments of the O-H stretches of the water molecule and hydroxyl units were reinterpreted based on a combination of the low-temperature infrared pleochroism of lawsonite and the known O-H bond lengths and inferred hydrogen bonding in this phase [95S1]. In [99S1] the above mode assignments were used to analyze the spectra. The primary divergence between the results of [96L2] and the assignment given by [74L1, 90L1] is that they evaluated the H_2O molecule not as a free unit superimposed in the bulk crystal, with both symmetric and asymmetric stretching vibrations, but rather as having two distinct O-H stretching vibrations produced by each of the O-H bonds in the H_2O molecule. According to [99S1], the IR spectrum of lawsonite between 500 and 4000 cm^{-1} can be divided into five separate regions - Fig. 26: (1) the O-H stretching vibration of the most weakly hydrogen bond hydroxyl unit, which produces a sharp band near 3560 cm^{-1}, ν_{OH}(b); (2) a broad band due to O-H stretches of both the H_2O molecule and the more strongly hydrogen bound hydroxyl unit centered at 3225 cm^{-1}, (ν_{OH}(a) at ~ 3240 cm^{-1} and ν_{H_2O}(a) at ~ 2950 cm^{-1}); (3) a single, lower amplitude peak due to the H–O–H bend of the water molecule, δ H_2O at 1625 cm^{-1}; (4) three peaks between 880 cm^{-1} and 1000 cm^{-1} produced by symmetric and asymmetric stretching modes of silicate tetrahedra $\nu_s SiO_4$ and $\nu_{as} SiO_4$ and (5) at 610 cm^{-1} a high-amplitude band produced by either O–Si–O and/or Si–O–Si silicate stretching/bending vibrations, δ Si–O–Si and δ O–Si–O. A significant smaller number of bands than were predicted to be IR active [90L1] was shown.

The IR study, at 300 K, under pressure [99S1] shows that the asymmetric and symmetric stretching and bending vibrations of the Si_2O_7 groups (at zero pressure frequencies between 600 and 1000 cm^{-1}) increase in frequency with pressure at rates between 3.6 and 5.9 cm^{-1}/GPa. All silicate modes appear to shift continuously with pressure up to 20 GPa, although the lowest frequency stretching vibration becomes unresolvable above 18 GPa, and a splitting of the main bending vibration is observed near this pressure. The O–H stretches of the hydroxyl units exhibit a discontinuity in their mode shift at ~ 8…9 GPa, which was interpreted to be produced by a pressure-induced change in hydrogen bonding. The stretching and bending vibrations of the water molecule were relatively unaffected by compression up to 20 GPa, thus showing that the structural cavities in which water molecules reside are relatively rigid. Significant changes in the amplitude of the O-H stretches of the hydroxyl and water units were observed at this pressure as well. The data show that the dominant structural units in lawsonite persist metastably at 300 K with only modest structural modifications well beyond the known stability field of this phase.

Raman spectra of natural lawsonite have been also recorded [90L1]. Three Raman bands of A_g type were expected and observed - Fig. 27 [90L1]: ν_s Si-O-Si (695 cm^{-1}); ν_s SiO_3 (915 cm^{-1}) and ν_{as} SiO_3 (935 cm^{-1}). Two bands of B_{1g} type are observed whereas only one is expected arising from ν_{as} SiO_3 (959 cm^{-1}). Only two bands of B_{2g} symmetry appear instead of three expected: ν_{as} Si-O-Si (1047 cm^{-1}) and ν'_s SiO_3 + ν'_{as} SiO_3 (912 cm^{-1}). The B_{3g} polarization spectra were difficult to be analysed because of poor quality of the spectra. The ν'_{as} SiO_3 was preferentially attributed to the 963 cm^{-1} band. The 809 cm^{-1} mode (B_{1g}, B_{3g}) probably arises from an AlO_6 stretching vibration.

The phase transitions in lawsonite were studied by analysing the temperature dependence of the IR spectra [96L2, 00M1]. In [00M1] a quantitative analysis was undertaken on the unmerged spectra. Phonon signals in the regions 170-180 cm^{-1} (a), 870…900 cm^{-1} (b), 800…1200 cm^{-1} (c), 1600…1700 cm^{-1} (d), 3300…3800 cm^{-1} (e), 2400…4000 cm^{-1} (f) and the peaks at 2750 cm^{-1} (g) and at 3250 cm^{-1} (h) were chosen for analysis - Fig. 28A. Two methods were employed, one to detect changes of the peak positions, $\Delta\omega$, with changing temperature, the second to measure the effective line width, Δcorr, of the peaks using the autocorrelation method. The change of $\Delta\omega$ and Δcorr are shown in Figs. 28B,C for some peaks. From the frequency data, a small peak near 900 cm^{-1} due to vibrations of the framework and peaks in the region 3400…3800 cm^{-1} due to OH and H_2O stretching modes show the largest variation. Below RT there are two peaks close to 3580 cm^{-1}. For the high-frequency branch, which is an OH stretching mode [96L2], the T_1 is clearly detected while the lower-frequency branch is sensitive to the second transition T_2. The Δcorr variations are more pronounced over the full spectral range than the ω variations - Fig. 28B. The values of $\delta\Delta$corr, which represent changes of Δcorr due to phase transitions were determined. The driving mechanism of the transition has been explained by [96L2] with a model of co-operative hydrogen bonds. At about 275 K the H_2O molecule starts ordering which is evidenced from $(\delta\Delta\text{corr})_e^2$

and $(\Delta\omega)_e^2$. The framework reacts to this behaviour. This can be seen in the behaviour of the framework mode at 900 cm^{-1} and in the expansion along ***a***. OH-modes follow this, but perhaps only to a temperature of about 200 K, where $\Delta\omega_e$ changes its slope towards a plateau. At T_2 the OH-s enter the next stage of order. Thus, the IR data reveal an almost tricritical behaviour for the square of the effective line width $(\delta\Delta\text{corr})^2_{3800}$, $(\Delta\omega)^2_{3650}$ and $(\Delta\omega)^2_{900}$ correlated to the square of the e_1 strain component. The $(\delta\Delta\text{corr})^2_{900}$ and $(\Delta\omega)^2_{3550}$ seem to follow a more complex behaviour of the strain components e_2^2 and e_3^2. The findings from IR and strain analysis allow the transitions to be understood as strain mediated ordering processes of protons in a channel parallel to the crystallographic ***c***-axis.

The birefringence values of lawsonite were studied in a large temperature range [95L1, 00S2]. The temperature dependences of the optical birefringence along the principal crystallographic directions are shown in Fig. 29 [00S2]. The variations of birefringence above T_1 are nonlinear along all directions. The corresponding deviations, which appear to be especially pronounced along the [001] direction, indicate strong pretransitional effects. These fluctuations effects occur in an extremely wide temperature range (~ 200 K above T_1). A smeared anomaly is observed only at T_1. The phase transition temperature was obtained from the derivative of the optical birefringence at $T_1 \cong 271$ K - Fig. 29. In the low-temperature region additional anomalies of the optical birefringence were observed at $T_2 \cong 120$ K along all crystallographic directions; the most pronounced one occurs along the [100] direction. These anomalies were attributed to the low-temperature transformation Pmcm-$P2_1cn$ [00S2].

Hennomartinite

The IR powder spectrum was analysed [92A1]. The spectrum between 1000 and 1200 cm^{-1} is similar to that for lawsonite. Strong absorption between 800 and 1000 cm^{-1} are similar to those for ilvaite. IR bands in this frequency range are due to vibrations of $[Si_2O_7]$ units. An absorption at 3555 cm^{-1} accompanied with a diffuse shoulder towards lower frequencies and one diffuse band at ~ 1650 cm^{-1} are characteristic of OH and H_2O [74L1].

Kilchoanite, barylite

The kilchoanite is optically biaxial with $n_\alpha = 1.647$, $n_\gamma = 1.650$ and $2V = 60°$ [61A1]. Values $n_\alpha = 1.680$, $n_\gamma = 1.706$ and $2V = 60°$ were reported for barylite [62H1].

Tables and figures

Table 1. Sorosilicates from groups VIII B 03-05 [91N1].

Silicate	Composition	Group
Barylite	$BaBe_2Si_2O_7$	VIII B 03
Kilchoanite	$Ca_3Si_2O_7$	VIII B 04
Rankinite	$Ca_3Si_2O_7$	VIII B 04
Ilvaite	$CaFe_3O(Si_2O_7)(OH)$	VIII B 05
Lawsonite	$CaAl_2(Si_2O_7)(OH)_2 \cdot H_2O$	VIII B 05
Hennomartinite	$SrMn_2(Si_2O_7)(OH)_2 \cdot H_2O$	VIII B 05

Table 2. Atomic sites and thermal parameters

a) Ilvaite $CaFe_{2.92}Al_{0.01}Mn_{0.02}Mg_{0.02}Si_2O_7O(OH)$ having space group Pnma at 400 K [89G2].

Atom	x	y	z	$\beta_{ij} \cdot 10^4$						S
				β_{11}	β_{22}	β_{33}	β_{12}	β_{13}	β_{23}	
FeA	0.89033(3)	0.05069(4)	0.00646(6)	93(1)	90(1)	97(1)	–2(1)	–8(1)	10(1)	2.500
FeB	0.94032(4)	0.73939(6)	0.25000(0)	111(2)	90(2)	104(2)	–7(2)	0(0)	0(0)	
Ca	0.81294(5)	0.37062(8)	0.75000(0)	95(3)	85(3)	127(3)	9(2)	0(0)	0(0)	
Si1	0.95960(7)	0.36816(10)	0.25000(0)	71(4)	68(4)	59(4)	0(3)	0(0)	0(0)	
Si2	0.67956(7)	0.22704(10)	0.25000(0)	72(4)	69(4)	62(4)	8(3)	0(0)	0(0)	
O1	0.01034(20)	0.02908(30)	0.75000(0)	139(11)	113(12)	143(11)	14(9)	0(0)	0(0)	
O2	0.93618(13)	0.27203(19)	0.01676(28)	120(7)	93(7)	71(7)	–23(3)	–7(6)	–19(6)	
O3	0.77722(18)	0.10929(29)	0.25000(0)	76(10)	94(10)	113(10)	20(8)	0(0)	0(0)	
O4	0.67096(13)	0.32975(20)	0.01886(30)	118(8)	98(7)	98(7)	6(6)	7(6)	15(6)	
O5	0.58469(18)	0.10115(8)	0.25000(0)	76(10)	84(10)	118(10)	5(8)	0(0)	0(0)	
O6	0.60171(20)	0.02444(21)	0.75000(0)	122(11)	96(11)	183(12)	–27(9)	0(0)	0(0)	
O7 (OH)	0.79764	0.10918(29)	0.75000(0)	105(10)	95(10)	88(10)	5(9)	0(0)	0(0)	

b) The same composition as in a) having space group $P2_1/a$ at 295 K [89G2].

Atom[3)]	x	y	z	$\beta_{ij} \cdot 10^4$						S
				β_{11}	β_{22}	β_{33}	β_{12}	β_{13}	β_{23}	
Fe(Ao)	0.89019(3)	0.04983(5)	0.00727(8)	67(2)	64(2)	86(2)	–2(2)	–3(1)	6(2)	2.276
Fe(Am)	0.89004(3)	0.05172(5)	0.49272(8)	60(2)	61(2)	80(2)	–2(2)	3(1)	–4(2)	2.724
Fe(B)	0.94063(3)	0.73996(5)	0.24886(8)	81(2)	61(2)	87(2)	–7(2)	–1(1)	–3(2)	
Ca	0.81296(5)	0.37035(7)	0.75267(11)	66(2)	60(2)	107(3)	6(2)	0(2)	–1(2)	
Si1	0.95955(6)	0.36831(10)	0.24296(15)	54(3)	47(3)	57(3)	0(3)	3(3)	2(3)	
Si2	0.67949(6)	0.22724(10)	0.25156(15)	47(3)	55(4)	58(3)	2(3)	1(3)	1(3)	
O1	0.00986(18)	0.02900(27)	0.73935(43)	79(9)	95(11)	134(11)	17(8)	–5(8)	–2(9)	
O2o	0.93712(17)	0.27206(28)	0.01614(39)	90(9)	69(9)	72(10)	–9(7)	–3(7)	–14(8)	
O2m	0.93547(17)	0.27264(28)	0.48315(40)	89(9)	75(9)	77(10)	–11(8)	–6(7)	6(8)	
O3	0.77717(16)	0.10951(27)	0.25521(40)	57(9)	64(9)	97(10)	17(7)	3(7)	–1(8)	
O4o	0.67137(17)	0.32852(27)	0.01910(39)	87(10)	69(10)	79(10)	0(8)	4(8)	7(8)	
O4m	0.67068(17)	0.33130(27)	0.48206(40)	86(9)	75(10)	80(10)	0(8)	5(7)	–20(8)	
O5	0.58481(16)	0.10087(26)	0.25308(41)	51(9)	64(9)	107(10)	1(7)	1(7)	–17(8)	
O6	0.60193(18)	0.25080(27)	0.75216(46)	75(9)	65(10)	174(11)	–22(8)	4(8)	8(9)	
O7 (OH)	0.79767(17)	0.10973(27)	0.74510(40)	69(9)	82(9)	81(9)	11(8)	9(7)	1(8)	

Table 2 (continued)

c) Lawsonite, $CaAl_2Si_2O_7(OH)_2 \cdot H_2O$, having space group Cmcm, at 295 K [95L1].

Atom	Multiplicity	Site symmetry	*x*	*y*	*z*	B_{eq} [Å^2]
Ca	4	mm	0	0.33321(3)	0.25	0.694(4)
Al	8	$\bar{1}$	0.25	0.25	0	0.341(3)
Si	8	m	0	0.98043(3)	0.13300(2)	0.348(3)
O1	4	mm	0	0.0496(1)	0.25	0.64(1)
O2	16	1	0.27263(7)	0.37884(5)	0.11693(3)	0.583(5)
O3	8	m	0	0.13758(7)	0.06497(4)	0.470(7)
O4	8	m	0	0.63922(8)	0.04793(5)	0.645(8)
O5	4	mm	0	0.6093(2)	0.25	1.56(2)
Hw	8	m	0	0.660(2)	0.199(2)	3.9(6)[1)]
Hh	8	m	0	0.559(3)	0.054(2)	7.1(8)[1)]

d) Lawsonite, $CaAl_2Si_2O_7(OH)_2 \cdot H_2O$, at 233 K, having space group Pmcn [95L1].

Atom	*x*	*y*	*z*	B_{eq} [Å^2]
Ca	0	0.33250(3)	0.25075(2)	0.553(3)
Al	0.25	0.25	0	0.269(7)
Ala	0.25	0.25	0.5	0.283(8)
Si	0	0.98049(5)	0.13200(3)	0.285(6)
Sia	0	0.97895(5)	0.36589(2)	0.299(6)
O1	0	0.0498(1)	0.24919(7)	0.51(1)
O2	0.2749(2)	0.37470(9)	0.11942(5)	0.52(1)
O2a	0.2716(2)	0.38008(9)	0.38420(4)	0.45(1)
O3	0	0.1375(1)	0.06359(6)	0.39(2)
O3a	0	0.1360(1)	0.43420(6)	0.42(2)
O4	0	0.6406(1)	0.0508(7)	0.44(2)
O4a	0	0.6346(1)	0.45757(8)	0.57(2)
O5	0	0.6089(1)	0.24855(8)	1.19(2)
Hw	0	0.647(3)	0.187(2)	3.4(7)[1)]
Hwa	0	0.677(3)	0.287(2)	3.3(7)[1)]
Hh	0	0.555(3)	0.038(2)	7.2(6)[1)]
Hha	0	0.571(5)	0.423(3)	9.7(1.3)[1)]

Table 2 (continued)

e) Lawsonite, $CaAl_2Si_2O_7(OH)_2 \cdot H_2O$, at 110 K, having space group $P2_1cn$ [95L1].

Atom	*x*	*y*	*z*	B_{eq} [Å^2]
Ca	0.0066(1)	0.33176(2)	0.25106(1)	0.311(3)
Al	0.25	0.24952(8)	–0.00036(6)	0.192(5)
Ala	0.2458(1)	0.25214(8)	0.50131(5)	0.162(5)
Si	–0.0031(1)	0.98003(4)	0.13181(2)	0.198(4)
Sia	–0.0010(1)	0.97795(4)	0.36558(2)	0.205(4)
O1	–0.0076(2)	0.0499(1)	0.24891(5)	0.35(1)
O2	0.2752(2)	0.3731(2)	0.1192(1)	0.367(5)[2)]
O2a	0.2675(2)	0.3818(2)	0.38584(9)	0.367(5)[2)]
O2b	–0.2763(2)	–0.3765(2)	–0.11797(9)	0.367(5)[2)]
O2c	–0.2761(2)	–0.3719(2)	–0.37840(9)	0.367(5)[2)]
O3	0.0024(2)	0.13682(9)	0.06297(5)	0.29(1)
O3a	–0.0011(2)	0.13475(9)	0.43428(5)	0.32(1)
O4	–0.0062(2)	0.6395(1)	0.05075(5)	0.31(1)
O4a	–0.0007(3)	0.6320(1)	0.45967(5)	0.38(1)
O5	–0.0130(3)	0.6094(1)	0.24811(6)	0.66(1)
Hw	–0.004(9)	0.640(2)	0.183(2)	2.8(5)[1)]
Hwa	0.958(7)	0.689(3)	0.283(2)	3.4(6)[1)]
Hh	0.008(8)	0.539(3)	0.037(2)	2.5(5)[1)]
Hha	0.043(7)	0.576(3)	0.414(2)	5.4(8)[1)]

[1)] refined isotropically; [2)] refined with $\beta_i(O2) = \beta_i(O2c) = \beta_i(O2b) = \beta_i(O2c)$ (i = 1 – 3);
[3)] In some papers are used rotations. M11-MAo; M12-MAm; M2-MB; O21 – O2o; O22 – O2m; O41 – O4o; O42 – O4m.

f) Hennomartinite, $SrMn_2[Si_2O_7](OH)_2 \cdot H_2O$, having space group Cmcm at 528 K [96L1]

Atom	*x*	*y*	*z*	$\beta_{ij} \cdot 10^4$					
				β_{11}	β_{22}	β_{33}	β_{12}	β_{13}	β_{23}
Sr	0	0.31258(4)	1/4	227(2)	220(2)	144(1)	0	0	0
Mn	1/4	1/4	0	109(1)	116(1)	112(1)	–4(1)	1(1)	–27(1)
Si	0	0.96991(7)	0.13224(4)	120(2)	90(2)	82(2)	0	0	0
O1	0	0.0198(3)	1/4	280(10)	220(10)	77(8)	0	0	0
O2	0.2851(2)	0.3723(1)	0.11492(2)	144(5)	178(5)	164(5)	–39(4)	18(4)	–55(4)
O3	0	0.1275(2)	0.0768(1)	216(8)	115(6)	148(7)	0	0	38(6)
O4	0	0.6340(2)	0.0424(2)	181(8)	127(6)	216(8)	0	0	32(6)
O5	0.0294[1)]	0.6068(5)	1/4	500(100)	370(20)	250(20)	0	0	0
Hw	0	0.637(6)	0.198(2)	B_{eq} [Å^2] = 4.74 (fixed isotropically)					
Hh	0	0.552(2)	0.046(4)	B_{eq} [Å^2] = 7.11 (fixed isotropically)					

Table 2 (continued)

g) Composition as in f) having space group $P2_1cn$ at 295 K [96L1]

Site[2)]	x	y	z	$\beta_{ij} \cdot 10^4$					
				β_{11}	β_{22}	β_{33}	β_{12}	β_{13}	β_{23}
Sr	0.01703	0.31155(4)	0.2517(1)	80(3)	100(1)	77(1)	–9(2)	29(7)	3(6)
Mn	0.2454(5)	0.2566(2)	–0.0051(1)	56(1)	46(1)	47(1)	3(2)	–21(8)	16(5)
Mn1	0.2482(5)	0.2508(2)	0.5023(2)	56(1)	46(1)	47(1)	3(2)	–21(8)	16(5)
Si	–0.001(1)	0.9715(5)	0.1315(2)	63(2)	44(3)	51(2)	0(3)	–10(10)	10(10)
Si1	–0.004(1)	0.9670(5)	0.3667(2)	63(2)	44(3)	51(2)	0(3)	–10(10)	10(10)
O1	–0.0179(8)	0.0202(3)	0.2477(9)	120(10)	95(9)	50(10)	–10(10)	–50(40)	–10(30)
O2	0.282(2)	0.372(1)	0.1130(5)	88(5)	73(7)	65(6)	–16(5)	–20(20)	–20(20)
O21	0.280(2)	0.379(1)	0.3915(5)	88(5)	73(7)	65(6)	–16(5)	–20(20)	–20(20)
O22	–0.287(1)	–0.3718(9)	–0.1171(4)	88(5)	73(7)	65(6)	–16(5)	–20(20)	–20(20)
O23	–0.294(1)	–0.3594(9)	–0.3752(5)	88(5)	73(7)	65(6)	–16(5)	–20(20)	–20(20)
O3	0.001(2)	0.128(1)	0.0746(5)	90(10)	65(5)	85(6)	1(9)	10(30)	–10(30)
O31	0.011(2)	0.127(1)	0.4227(4)	90(10)	65(5)	85(6)	1(9)	10(30)	–10(30)
O4	–0.001(1)	0.6368(7)	0.0462(4)	80(10)	78(8)	81(9)	–7(9)	10(20)	–10(10)
O41	–0.017(2)	0.6269(7)	0.4631(5)	80(10)	78(8)	81(9)	–7(9)	10(20)	–10(10)
O5	–0.025(1)	0.6082(4)	0.2475(7)	370(30)	210(10)	190(20)	–60(20)	–190(50)	0(40)
HwL[3)]	–0.148(5)	0.626(9)	0.26(1)						
HwR[3)]	–0.148(5)	0.626(9)	0.24(1)						
Hw1L[3)]	–0.02(2)	0.642(8)	0.195(3)						
Hw1R[3)]	–0.02(2)	0.642(8)	0.305(3)						
HhL[3)]	–0.09(1)	0.61(1)	0.415(4)						
HhR[3)]	–0.09(1)	0.61(1)	0.085(4)						
Hh1L[3)]	0.03(2)	0.551(6)	0.030(8)						
Hh1R[3)]	0.03(2)	0.551(6)	0.470(8)						

[1)] split atom position; [2)] L und R mark the respective split H positions (x, y, z; x, y, 0.5–z). The twinned domain structure was refined with fractions of 7 % disorder (–x, y, z) and 43 % twin fraction (–x, y, z); [3)] fixed isotropically B_{eq} [Å^2] = 3.95 for Hw-type sites and 6.32 for Hh-type sites.

Table 3. Crystal structure and lattice parameters.

Sample	T [K]	Space group	Lattice parameters				Refs.
			a [Å]	b [Å]	c [Å]	β	
Kilchoanite[1)]	RT	Imam Ima2	11.42(5)	5.09(5)	21.95(5)		61A1
Barylite[2)]	RT	Pnma	9.79	11.65	4.63		41Y1
Barylite[3)]	RT	Pnma	9.82(1)	11.67(1)	4.69(1)		77R1
Ilvaite[2)]	RT	Pbnm	8.76	13.04	5.82		36K1
Ilvaite[2)]	RT	Pbnm	8.800	13.019	5.852		74B1
Ilvaite[4)]	RT	Pbnm	8.818(5)	13.005(5)	5.853(3)		76H1
Ilvaite[5)]	RT	Pbnm	8.843(1)	13.006(2)	5.843(2)		89G1

Table 3 (continued)

Sample	*T* [K]	Space group	Lattice parameters				Refs.
			a [Å]	*b* [Å]	*c* [Å]	β	
Ilvaite[6)]							
x = 0.35 wt%	RT	Pbnm	8.756(11)	13.004(10)	5.828(10)		79Y1
x = 1.35 wt%	RT	Pbnm	8.754(6)	13.014(6)	5.840(5)		
x = 3.37 wt%	RT	Pbnm	8.818(6)	13.006(5)	5.853(5)		
x = 5.26 wt%	RT	Pbnm	8.824(11)	13.001(8)	5.830(6)		
x = 6.07 wt%	RT	Pbnm	8.825(11)	12.993(12)	5.838(5)		
x = 9.03 wt%	RT	Pbnm	8.829(11)	12.945(11)	5.836(6)		
Ilvaite[7)]	RT	$P2_1/a$	13.0065(9)	8.8073(7)	5.858(4)	90.332(6)°	87G1, 92G1
Ilvaite[8)]	RT	$P2_1/a$	13.0103(5)	8.8039(4)	5.8517(3)	90.209(5)°	82F1, 87F1
Ilvaite[9)]	RT	$P2_1/a$	13.0056(6)	8.7976(5)	5.8539(5)	90.105(6)°	82F1, 87F1
Ilvaite[18)]	5	$P2_1/a$	13.0229(2)	8.7977(1)	5.8428(1)	90.234(1)°	84G1
	80	$P2_1/a$	13.0230(6)	8.7994(4)	5.8422(2)	90.231(3)°	84G1
	150	$P2_1/a$	13.0244(7)	8.8006(5)	5.8445(3)	90.233(3)°	84G1
	350	$P2_1/a$	13.0207(7)	8.8121(4)	5.8609(3)	90.249(3)°	84G1
Ilvaite[10)]	RT	$P2_1/a$	13.009(1)	8.8008(3)	5.8589(2)	90.324(9)°	83T1
Ilvaite[11)]	RT	$P2_1/a$	13.013(3)	8.8197(6)	5.8424(5)	90.03(1)°	83T1
Ilvaite[12)]	RT	$P2_1/a$	13.041(1)	8.831(1)	5.8642(4)	90.253(7)°	94T1
Ilvaite[13)]	RT	$P2_1/a$	13.036(7)	8.842(4)	5.856(3)	90.08(4)°	94T1
Ilvaite[14)]	RT	$P2_1/a$	13.018(7)	8.818(3)	5.862(2)	90.28(3)°	94T1
Ilvaite[15)]	RT	$P2_1/a$	13.007(5)	8.837(3)	5.852(2)	90.07(3)°	93T1
Ilvaite[16)]	RT		13.019(4)	8.800(3)	5.852(3)	90.00°	72B1
Ilvaite[17)]	RT		13.015(2)	8.807(2)	5.854(1)	90.22(3)°	72D1
Ilvaite[2)]	RT		13.007(2)	8.817(2)	5.851(1)	90.28(2)°	68B1
Ilvaite[9)]	297	$P2_1/a$	13.0387(10)	8.8204(5)	5.8640(5)	$90.266(5)^0$	89G2
	380	Pnma	13.0533(9)	8.8345(5)	5.8674(3)	90.006(5)°	
Ilvaite[18)]	298	$P2_1/a$	13.014(1)	8.804(1)	5.8589(4)	90.245°	88R1
Ilvaite[19)]	RT	$P2_1/a$	13.0042(3)	8.8066(2)	5.8542(2)	90.197°	98S1
Hennomartinite[20)]	130		6.2372(6)	9.015(2)	13.386(5)		92A1
	RT	Cmcm	6.255(1)	9.034(2)	13.397(2)		92A1
Hennomartinite[21)]	295	$P2_1cn$	6.247(1)	9.034(1)	13.401(2)		96L1
	518	Cmcm	6.255(1)	9.067(1)	13.431(2)		96L1
Lawsonite[22)]	RT	Ccmm	8.795(3)	5.847(1)	13.142(6)		78B1
Lawsonite[23)]	2	$P2_1cn$	5.86465(2)	8.7652(3)	13.1002(5)		01M1
	50	$P2_1cn$	5.8639(2)	8.76442(4)	13.099(5)		
	100	$P2_1cn$	5.86332(2)	8.76659(4)	13.1021(5)		
	130	Pmcn	5.86243(2)	8.76981(4)	13.1063(5)		
	175	Pmcn	5.86092(2)	8.77586(4)	13.1132(6)		
	225	Pmcn	5.85942(2)	8.78269(4)	13.1209(6)		
	268	Pmcn	5.85539(3)	8.79152(5)	13.1326(7)		
	285	Cmcm	5.85424(3)	8.79471(6)	13.1365(8)		
	300	Cmcm	5.8543(4)	8.79679(7)	13.1387(9)		
	350	Cmcm	5.85603(3)	8.80228(7)	13.1442(9)		

Table 3 (continued)

Sample	*T* [K]	Space group	Lattice parameters				Refs.
			a [Å]	*b* [Å]	*c* [Å]	β	
Lawsonite[23] (cont.)	400	Cmcm	5.85851(3)	8.80727(7)	13.149(8)		
	500	Cmcm	5.8642(5)	8.817(1)	13.159(1)		
Lawsonite[24]	RT		8.75	13.09	5.84		57S1
Lawsonite[2]	RT		8.787	13.123	5.826		61P1
$NaBa_3Si_2O_7$	RT	$P6_3/mmc$, $P6_3mc$, $P\bar{6}2c$	5.791(4)		14.748(8)		71F1

[1] $(Ca_{23.47}Mn_{0.03}Fe^{3+}_{0.05})(Si_{15.71}Al_{0.35}O_{55.53}OH_{0.47})$;
[2] Natural sample;
[3] $BaBe_2Si_2O_7$;
[4] $Ca_{3.84}Fe^{2+}_{7.03}Fe^{3+}_{4.24}Mn_{0.78}Mg_{0.08}Al_{0.03}Si_{7.94}O_{36}H_4$;
[5] $CaFe_{1.81}Mn_{0.19}Si_2O_7O(OH)$;
[6] $Ca(Fe^{2+}Fe^{3+})_2(Fe^{2+},Mn^{2+})Si_2O_7O(OH)$, having x wt% Mn
[7] $CaFe^{2+}_2Fe^{3+}Si_2O_7O(OH)$ synthetic;
[8] $CaFe_{2.73}Al_{0.12}Mn_{0.07}Mg_{0.04}Si_2O_8(OH)$;
[9] $CaFe_{2.92}Al_{0.01}Mn_{0.02}Mg_{0.02}Si_2O_7O(OH)$;
[10] Natural sample, Tsumo, Japan;
[11] Natural sample, Techukhe, Siberia;
[12] $Ca_{1.01}Fe^{3+}_{1.00}Fe^{2+}_{1.84}Mn_{0.15}Si_{2.00}HO_{8.5}$;
[13] $Ca_{0.93}Fe^{3+}_{1.00}Fe^{2+}_{1.74}Mn_{0.36}Si_{1.97}HO_{8.5}$;
[14] $Ca_{0.99}Fe^{3+}_{1.00}Fe^{2+}_{1.89}Mn_{0.14}Si_{1.99}HO_{8.5}$;
[15] $(Ca_{0.96}Mn_{0.02})(Fe^{2+}_{1.00}Fe^{3+}_{0.93}Al_{0.07})(Fe^{2+}_{0.50}Mn_{0.50})[Si_{1.96}Al_{0.04}]O_7O(OH)$;
[16] Natural sample, Elba;
[17] Natural sample, Switzerland;
[18] Natural sample, Seriphos, Greece;
[19] $Ca_{0.997}\{(Fe^{2+},Fe^{3+})_{2.877}Mg^{2+}_{0.016}Mn^{2+}_{0.060}Al^{2+}_{0.047}\}[Si_{1.996}Al_{0.004}]O_8(OH)$;
[20] $Sr_{0.98}Ba_{0.01}Mn_{2.01}Fe_{0.03}Si_{1.97}O_7(OH)_2 \cdot H_2O$;
[21] $SrMn_2[Si_2O_7](OH)_2 \cdot H_2O$;
[22] $Ca_{0.981}(Al_{1.953}Fe_{0.036}Ti_{0.013})Si_{2.013}O_7(OH)_2 \cdot H_2O$;
[23] $Ca_{1.00}Al_{1.95}Fe_{0.05}Si_{2.01}O_7(OH)_2 \cdot H_2O$;
[24] Natural sample, Mountailand.

Table 4. Thermal expansion coefficients.

Silicate	α_{ij} [10^{-5} K^{-1}]			Temperature range	Refs.
	α_a	α_b	α_c		
Lawsonite	1.26(4)	1.12(4)	0.76(3)	$20 \le T \le 600$ °C	96C1
Lawsonite	1.49	1.18	1.12	$15 \le T \le 449$ °C	90L1

Table 5. Compressibility coefficients.

Silicate	$\beta_{ij} \cdot 10^4$ [GPa^{-1}]			p [GPa]	Reference
	β_a	β_b	β_c		
Lawsonite	3.4(1)	3.0(1)	2.8(2)	$p < 3.77$	96C1

Table 6. Elastic properties.

a) Elastic moduli[1)].

Silicate	K [GPa]	G [GPa]	Method	Refs.
Lawsonite	110(4)		Diamond anvil cell, 3.8 GPa	96C1
Lawsonite	191(5)		Diamond anvil cell, 12 GPa	96H1
Lawsonite	124.1(1.8)		Diamond anvil cell, 7.8 GPa	99D1
Lawsonite	106.7(1.3)		Cubic anvil apparatus, 7.2 GPa	00G1
Lawsonite	112(6)		Multi anvil high pressure / high temperature cell, 7 GPa	00C1
Lawsonite	125(2)	52(2)	Brillouin, 1 atm	00S1

[1)] in all static compression experiments $K' \cong 4$.

b) Elastic coefficients.

Silicate	c_{ij} [GPa]									Ref.
	c_{11}	c_{22}	c_{33}	c_{44}	c_{55}	c_{66}	c_{12}	c_{13}	c_{23}	
Lawsonite	226(2)	214(2)	259(2)	65(1)	60(1)	17(1)	69(2)	65(2)	82(2)	00S1

Table 7. Magnetic moments determined by neutron diffraction along the crystallographic axes x, y, z and the total moments p.

Sample	T [K]	Components	p_{Fe}(Ao) [μ_B/atom]	p_{Fe}(Am) [μ_B/atom]	p_{Fe}(B) [μ_B/atom]	Ref.
$CaFe_{2.92}Al_{0.01}Mn_{0.02}Si_2O_7O(OH)$	5	p_x	–0.2(1)	–0.3(2)	0.6(2)	90G1
		p_y	–3.3(1)	–4.1(1)	3.5(2)	
		p_z	0.6(1)	0.8(2)	–1.5(3)	
		p	3.4(1)	4.2(1)	3.9(2)	
	80	p_x	–0.6(1)	–0.8(2)	–0.2(3)	
		p_y	–3.1(1)	–3.9(1)	1.4(2)	
		p_z	–0.1(4)	–0.2(3)	–0.9(5)	
		p	3.2(1)	3.9(1)	1.7(3)	

Table 8. Data obtained from magnetic measurements.

Sample	T_N [K]	Θ [K]	C [emu K/f.u.]	Refs.
Ilvaite (Elba)	118(2)	–300(25) (140≤T≤350)		84C1
Ilvaite (Seriphos)	118(3)			
Ilvaite (Fujian)	116(3)			
Ilvaite (Seriphos)	121.9(5)			87G1
Ilvaite	123.0(5)	Θ_a = –342.4 Θ_b = –373.7 Θ_c = –318.9 <Θ> = –341.7	21.4 22.37 20.6 20.6	87G2
$CaFe^{2+}_{2-x}Mn_xFe^{3+}Si_2O_7(OH)$				
x = 0	127			95C1
x = 0.12	128			
x = 0.19	121.8			

For Table 9 see p. 115

Table 10. Activation energies in ilvaites.

Sample	Type of measurements	Activation energies [eV]		Refs.
		E_{a1}	E_{a2}	
Ilvaite	^{57}Fe NGR	0.11 (300K≤T≤500K)		84L1
$CaFe^{2+}_{2-x}Mn_xFe^{3+}Si_2O_8(OH)$	^{57}Fe NGR			92G1
x = 0		0.10(1) (295K≤T≤365K)	0.60…0.70 (365K<T<455K)	
x = 0.12		0.10(1) (295K≤T≤355K)	0.90…1.10 (355K<T<455K)	
x = 0.19		0.25(1) (295K≤T≤345K)	0.75…1.15 (345K<T<455K)	
Ilvaite (natural) x = 0.02	^{57}Fe NGR	0.11 (T>360K)		92G1
$CaFe^{2+}_{2-x}Mn_xFe^{3+}Si_2O_8(OH)$	^{57}Fe NGR			95C1
x = 0		0.018 (50K<T<120K)		
x = 0.19		0.023 (50K<T<120K)		
Ilvaite (natural)	μSR	0.017 (50K<T<120K)		94D1

Table 10 (continued)

Sample	Type of measurements	Activation energies [eV]		Refs.
		E_{a1}	E_{a2}	
Ilvaite (natural)	Electrical resistivity	0.13 (210K<T<330K) 0.36 (330K<T<410K)	0.67 (410K<T<500K)	84C1
Ilvaite	Electrical resistivity	0.15		77H1
Ilvaite (natural) (Livorno - Italy)	Electrical resistivity	0.24 [1)]		75G1, 75G2
$Ca_{0.98}Mn_{0.021}Fe_{2.97}Al_{0.026}(Si_{1.99}O_7)O(OH)$	Specific heat	0.077 300 <T< 500 K		88R1

[1)] Temperature range not mentioned.

Table 11. Data obtained by ^{29}Si MAS NMR spectroscopy.

Silicate	Chemical shift [ppm]				$\Delta\delta$ [2)] [ppm]	η [3)]	Ref.
	δ_i [1)]	δ_{11}	δ_{22}	δ_{33}			
Lawsonite[4)]	–81	–123	–92	–28	80	0.58	83S1

[1)] isotropic chemical shift; δ_{ii} are the principal values of the chemical shielding;
[2)] chemical shift anisotropy;
[3)] asymmetry parameter;
[4)] natural sample.

Table 9. Data obtained from ^{57}Fe nuclear gamma resonance method.

Sample	Sites	T [K]	p [GPa]	δ [1)] [mm/s]	ΔQ [mm/s]	B_{hf} [T]	Γ [mm/s]	η	θ [°]	A [%]	Refs.
Ilvaite		RT		1.03(3)[2)]	2.30(3)						71G1
(Livorno – Italy)				0.49(3)[3)]	1.32(3)						
				0.86(3)[2)]	1.85(3)						
		520		0.85(5)[2)]	1.95(3)						
				0.51(5)[2)]	1.15(2)						
Ilvaite	Fe^{3+}(A)	4.2		0.56	1.14[3)]	50.9	0.40		34	36	84C1
(Elba)	Fe^{2+}(A)			1.25	2.25	18.1	0.35	0.0	15	32	
	Fe^{2+}(B)			1.10	2.75	31.5	0.38	0.1	17	32	
Ilvaite	Fe^{3+}(A)	4.2		0.58	1.16[3)]	50.2	0.36		35	37	84C1
(Seriphos)	Fe^{2+}(A)			1.29	2.32	18.1	0.36	0.0	14	32	
	Fe^{2+}(B)			1.18	2.75	31.2	0.37	0.0	17	31	
Ilvaite	Fe^{3+}(A)	4.2		0.60	1.14[3)]	50.4	0.37		34	35	84C1
(Fujian)	Fe^{2+}(A)			1.29	2.32	18.2	0.40	0.1	15	30	
	Fe^{2+}(B)			1.14	2.91	30.9	0.40	0.3	19	35	
Ilvaite[4)]	Fe^{3+}(A)	4		0.56	0.71	52.0	0.55				88X1
(Elba)	Fe^{2+}(A)			1.06	3.11	32.4	0.52	0.36	18		
	Fe^{2+}(B)			1.20	2.50	18.5	0.47	0.04	12		
	Fe^{3+}(A)	20		0.59	0.72	51.8	0.56				
	Fe^{2+}(A)			1.08	3.09	32.4	0.31	0.31	19		
	Fe^{2+}(B)			1.20	2.49	16.8	0.52	0.08	13		
	Fe^{3+}(A)	77		0.51	0.59	43.5	0.75				
	Fe^{2+}(A)			1.00	3.04	27.8	0.64	0.24	25		
	Fe^{2+}(B)			1.12	2.37	6.5	0.54	0.25	41		
	Fe^{3+}(A)	120		0.60	1.19		0.63				
	Fe^{2+}(A)			1.04	2.93		0.59				
	Fe^{2+}(B)			0.99	2.39		0.58				

Table 9 (continued)

Sample	Sites	T [K]	p [GPa]	δ [1)] [mm/s]	ΔQ [mm/s]	B_{hf} [T]	Γ [mm/s]	η	θ [°]	A [%]	Refs.
Ilvaite [5)]	Fe^{2+}-Fe^{3+}(A)	473		0.66	1.40		0.40	66			92L1
	Fe^{2+}(B)			1.04	2.21		0.24	34			
	Fe^{2+}-Fe^{3+}(A)	573		0.62	1.31		0.31	66			
	Fe^{2+}(B)			0.99	2.15		0.24	34			
	Fe^{2+}-Fe^{3+}(A)	673		0.57	1.31		0.28	63			
	Fe^{2+}(B)			0.99	1.99		0.28	37			
$CaFe^{2}_{2-x}Mn_xFe^{3+}Si_2O_8(OH)$ x = 0; 0.11; 0.19	Fe^{3+}(A)	4				50.3			43		95C1
	Fe^{2+}(A)					18.0			14		
	Fe^{2+}(B)					31.0					
Ilvaite [6)]	Fe^{3+}(A)	298		0.510(6)	1.28(2)		0.24(1)			25.55	80E1
(0.36 wt % Mn)	Fe^{2+}(A)			1.085(6)	2.12(2)		0.28(1)			40.07	
(Seriphos – Greece)	Fe^{2+}(B)			1.066(6)	2.53(2)		0.25(1)			26.53	
	Fe^{n+}(A)			1.459(6) [7)]	0.40(2)		0.32(1)			7.95	
Ilvaite	Fe^{n+}(A) [12)]	425		0.670	1.363		0.398			67.4	80E1
(0.36 wt % Mn)	Fe^{2+}(B)			1.002	2.158		0.314			32.6	
(Seriphos – Greece)	Fe^{n+}(A) [12)]	475		0.577	1.304		0.361			67.2	80E1
	Fe^{2+}(B)			0.972	2.094		0.301			32.8	
Ilvaite[8)]	Fe^{3+}(A)	298		0.557(6)	1.32(2)		0.29(1)			30.01	80E1
(0.89 wt % Mn)	Fe^{2+}(A)			1.056(6)	2.05(2)		0.33(1)			36.29	
(Calamito-Elba, Italy)	Fe^{2+}(B)			1.065(6)	2.53(2)		0.24(1)			23.85	
	Fe^{n+}(A)			1.619(6)	0.57(2)		0.32(1)			9.86	
Ilvaite[9)]	Fe^{3+}(A)	298		0.567(6)	1.29(2)		0.26(1)			30.11	80E1
(1.14 wt % Mn)	Fe^{2+}(A)			1.056(6)	2.07(2)		0.28(1)			31.18	
	Fe^{2+}(B)			1.062(6)	2.52(2)		0.25(1)			27.42	
	Fe^{n+}(A)			1.467(6)	0.29(2)		0.27(1)			11.29	
Ilvaite[10)]	Fe^{3+}(A)	298		0.489(6)	1.35(2)		0.23(1)			26.94	80E1
(3.35 wt % Mn)	Fe^{2+}(A)			1.012(6)	2.18(2)		0.28(1)			38.91	
(Laxey Mine – Idaho)	Fe^{2+}(B)			1.193(6)	2.30(2)		0.21(1)			24.24	
	Fe^{n+}(A)			1.590(6) [7)]	0.34(2)		0.34(1)			9.92	

Table 9 (continued)

Sample	Sites	T [K]	p [GPa]	δ [1)] [mm/s]	ΔQ [mm/s]	B_{hf} [T]	Γ [mm/s]	η	θ [°]	A [%]	Refs.
Ilvaite[9)]	Fe^{3+}(A)	298	2	0.484(6)	1.21(2)		0.28(1)			33.6	80E1
(1.14 wt % Mn)	Fe^{2+}(A)			1.090(6)	1.97(2)		0.32(1)			31.1	
	Fe^{2+}(B)			0.983(6)	2.47(2)		0.28(1)			20.8	
	Fe^{n+}(A)			1.579(6)[7)]	0.28(2)		0.40(1)			14.4	
Ilvaite[9)]	Fe^{3+}(A)	298	3	0.495(6)	1.22(2)		0.28(1)			35.4	80E1
(1.14 wt % Mn)	Fe^{2+}(A)			0.957(6)	1.86(2)		0.30(1)			25.4	
	Fe^{2+}(B)			0.981(6)	2.46(2)		0.29(1)			26.4	
	Fe^{n+}(A)			1.553(6)[7)]	0.21(2)		0.34(1)			12.8	
Ilvaite[9)]	Fe^{3+}(A)	298	6	0.463(6)	1.22(2)		0.24(1)			21.9	80E1
(1.14 wt % Mn)	Fe^{2+}(A)			0.851(6)	1.74(2)		0.34(1)			40.7	
	Fe^{2+}(B)			0.968(6)	2.50(2)		0.29(1)			25.5	
	Fe^{n+}(A)			1.501(6)[7)]	0.19(2)		0.41(1)			11.9	
Ilvaite[9)]	Fe^{3+}(A)	298	after	0.507(6)	1.22(2)		0.28(1)			35.8	80E1
(1.14 wt % Mn)	Fe^{2+}(A)		high	1.014(6)	1.95(2)		0.28(1)			28.8	
	Fe^{2+}(B)		pressu	0.992(6)	2.41(2)		0.28(1)			24.7	
	Fe^{n+}(A)		re removal	1.582(6)[7)]	0.34(2)		0.46(1)			10.7	
Ilvaite	Fe^{3+}(A)	80		0.604(3)	1.003(6)	–21.5(5)				37.8(2)	79Y1
(2.58 wt % Mn)	Fe^{2+}(A)			1.368(3)	1.756(6)	–15.6(5)				39.3(2)	
(Tsumo – Japan)	Fe^{2+}(B)			0.912(3)	2.383(6)					21.9(2)	
	Fe^{3+}(A)	293		0.627(3)	1.320(6)		0.326(3)			33.5(2)	
	Fe^{2+}(A)			1.190(3)	2.513(6)		0.374(3)			33.7(2)	
	Fe^{2+}(B)			1.243(3)	1.925(6)		0.344(3)			32.8(2)	
Ilvaite	Fe^{3+}(A)	293		0.627(3)	1.354(6)		0.441(3)			39.4(2)	79Y1
(8.40 wt % Mn)	Fe^{2+}(A)			1.134(3)	2.623(6)		0.434(3)			38.2(2)	
(Daikoku – Japan)	Fe^{2+}(B)			1.037(3)	2.179(6)		0.361(3)			22.4(2)	
Ilvaite[11)]	Fe^{3+}(A)	121		0.54	1.55		0.36			38	98S1
	Fe^{2+}(A)			1.21	2.61		0.25			22	
	Fe^{2+}(B)			1.26	2.27		0.32			40	

Table 9 (continued)

[1] relative to α-Fe if other notations were not used;
[2] relative to ^{57}Co in Cu;
[3] at 120 K;
[4] composition $CaFe_{2.73}Al_{0.12}Mn_{0.07}Mg_{0.04}Si_2O_8(OH)$;
[5] composition $CaFe_{2.94}Mg_{0.02}Mn_{0.02}Al_{0.01}Ti_{0.01}Si_2O_8(OH)$;
[6] composition (in wt %) $Fe_{39.24}Si_{15.93}Ca_{9.39}Mn_{0.36}(O+H)_{35.08}$;
[7] center of gravity;
[8] composition (in wt %) $Fe_{38.37}Si_{15.97}Ca_{9.40}Mn_{0.89}(O+H)_{35.36}$;
[9] composition (in wt %) $Fe_{38.03}Si_{15.91}Ca_{9.40}Mn_{1.14}(O+H)_{35.53}$;
[10] composition in (wt %) $Fe_{36.08}Si_{16.01}Ca_{9.33}Mn_{3.35}(O+H)_{35.23}$;
[11] $Ca_{0.997}\{(Fe^{2+},Fe^{3+})_{2.877}Mg^{2+}_{0.016}Mn^{2+}_{0.060}Al^{2+}_{0.047}[Si_{1.996}Al_{0.004}]O_8(OH)$;
[12] Coalescence at $T \geq 400$ K of Fe^{2+} and Fe^{3+} (8d) into single "Fe^{3+}-like" doublet.

Ilvaite

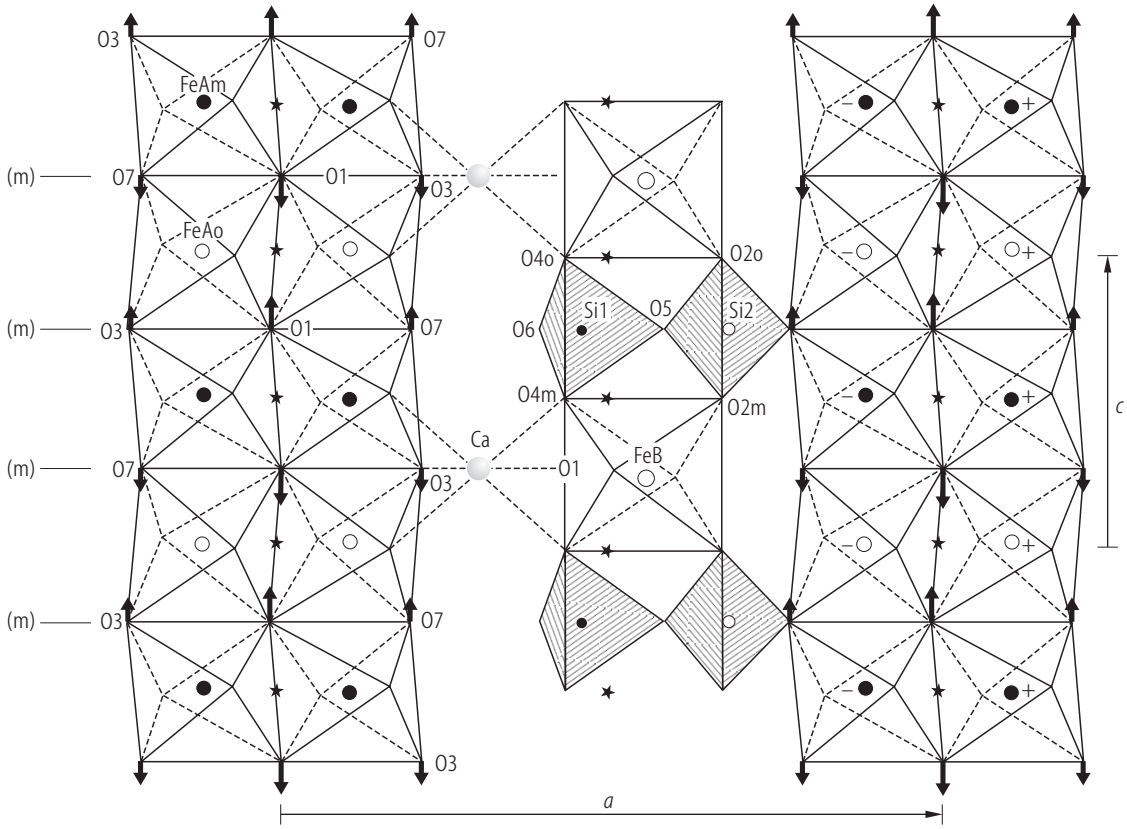

Fig. 1. Ilvaite. A view of the "dynamical" structure in terms of atomic displacement vectors, ***u***(l), calculated from atomic coordinates at 295 K and 400 K, and the unit cell dimensions at 400 K [89G2].

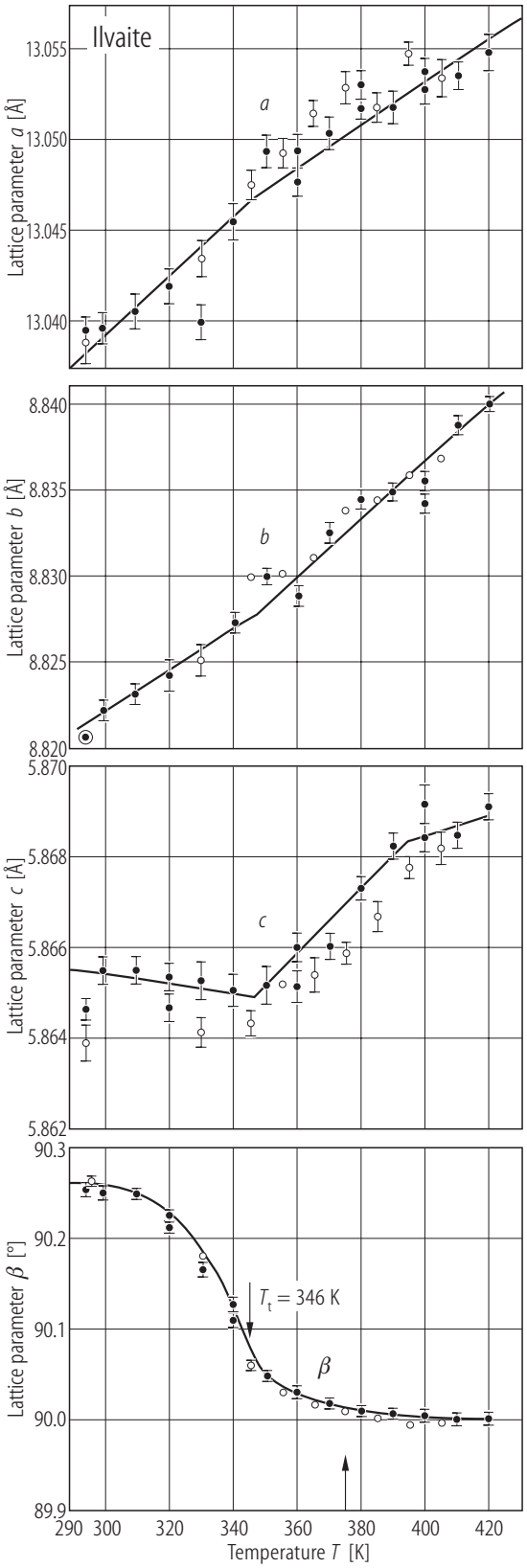

←

Fig. 2. Ilvaite. Unit cell dimensions as a function of temperature. Filled and unfilled circles indicate measurements on heating and cooling cycles, respectively. The full lines are visual fits [89G2].

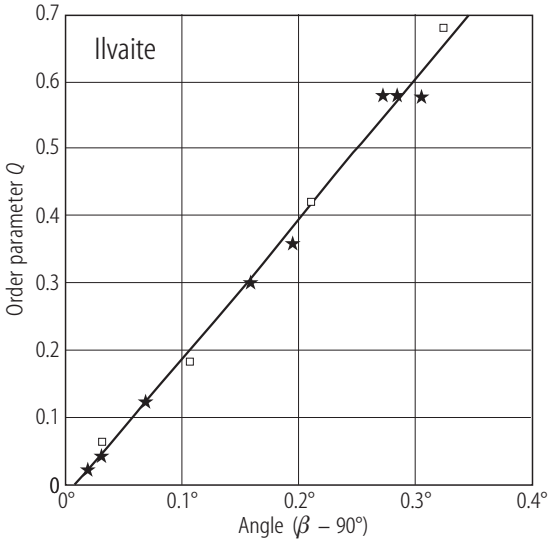

Fig. 3. Ilvaite. Order parameter, Q, as function of the monoclinic angle ($\beta - 90°$). By stars are denoted the data obtained by [94C2] and the squares are data from literature as listed in [94C2].

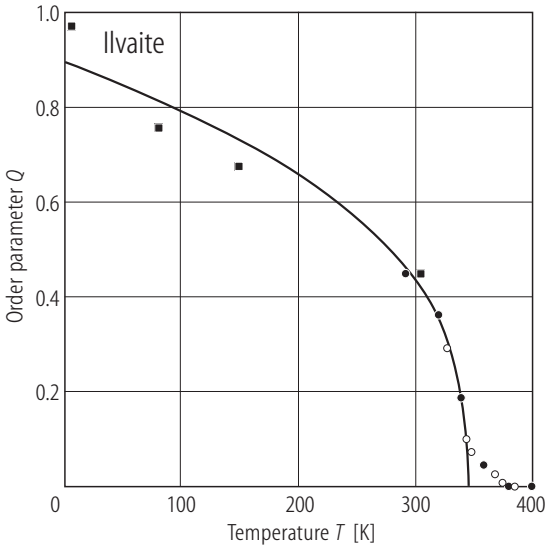

Fig. 4. Ilvaite. Order parameter, Q, as a function of temperature. The data noted by filled circles [89G2] and filled squares [84G1] were determined from the difference in the normalized effective ionic charges at the Fe (Ao) and Fe (Am) sites. Open circles were derived from the relationship $Q = 1.73\ \Delta\beta$, where $\Delta\beta = \beta - 90°$ [89G2].

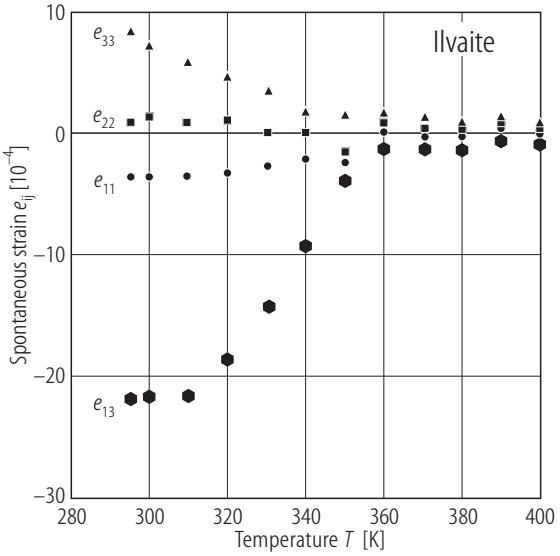

Fig. 5. Ilvaite. The strain components, e_{ij}, as a function of temperature [89G2].

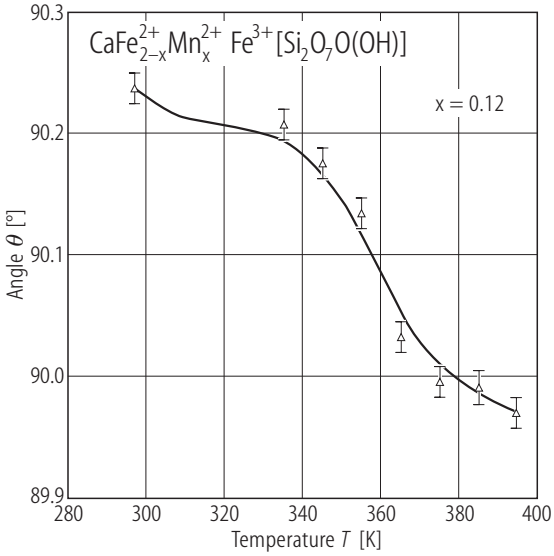

Fig. 6. $CaFe^{2+}_{2-x}\ Mn^{2+}_{x}\ Fe^{3+}[Si_2O_7O(OH)]$ with x = 0.12. Temperature dependence of the monoclinic angle [92G1].

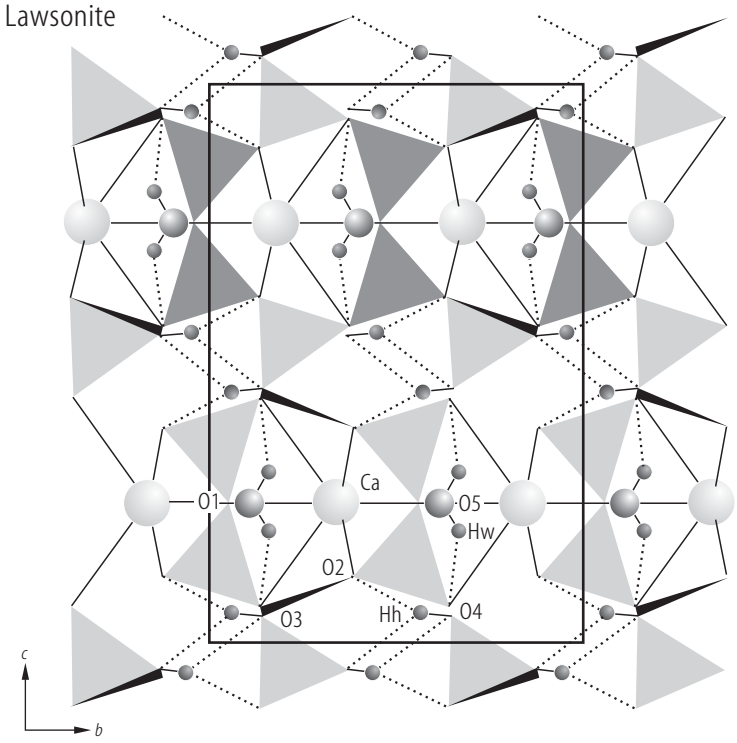

Fig. 7. Lawsonite. Cmcm structure at 295 K, projection along [100]. The edge-sharing AlO_6 octahedra form rods parallel to [100] that are interconnected by Si_2O_7 groups. The interstices of the framework are occupied by Ca atoms (large spheres), H_2O molecules (O5, medium sphere) and the H atoms (small spheres) of the OH groups. Dotted lines represent O....H distances between 1.9 and 2.5 Å [95L1].

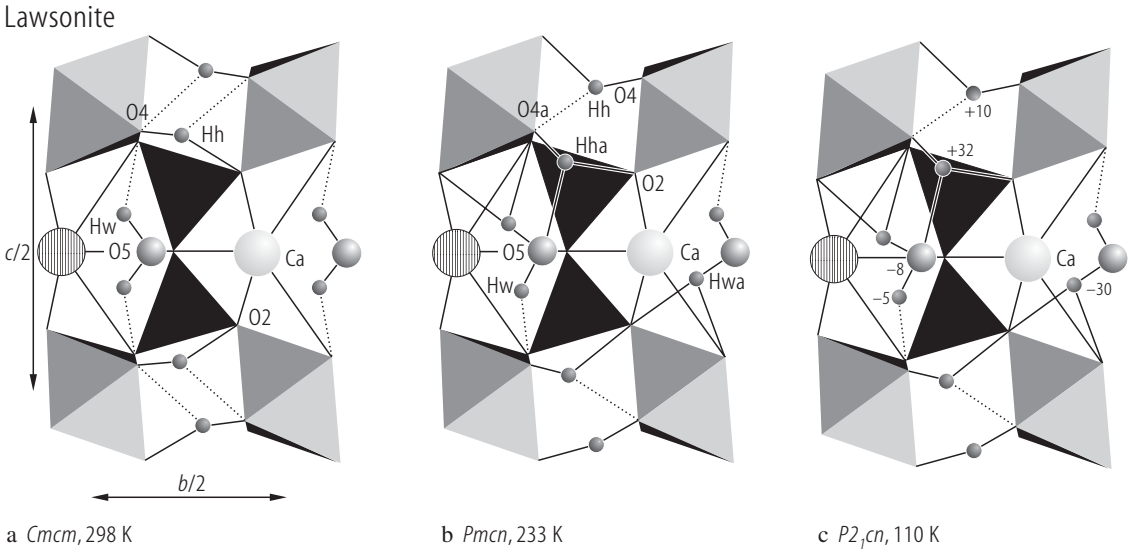

a *Cmcm*, 298 K b *Pmcn*, 233 K c $P2_1cn$, 110 K

Fig. 8. Lawsonite. Structure projected along [100]. **(a)** Cmcm structure, at room temperature; **(b)** Pmcn at 233 K **(c)**; $P2_1cn$ at 110 K. Numbers denote the deviation of the atom from the (100) plane (x = 0) in Å·10^{-2}. Dashed lines indicate H.....O bonds shorter than 2.00(2) Å [00S2].

Fig. 9. Lawsonite. Temperature dependences of the lattice parameters and of the volume [01M1]. The coth-function used as a baseline in spontaneous strain calculations is also shown (solid lines).

Fig. 10. Lawsonite. Dilatation data and model fits versus temperature. The model is a tricritical Landau potential with order parameter saturation at low temperatures [00M1].

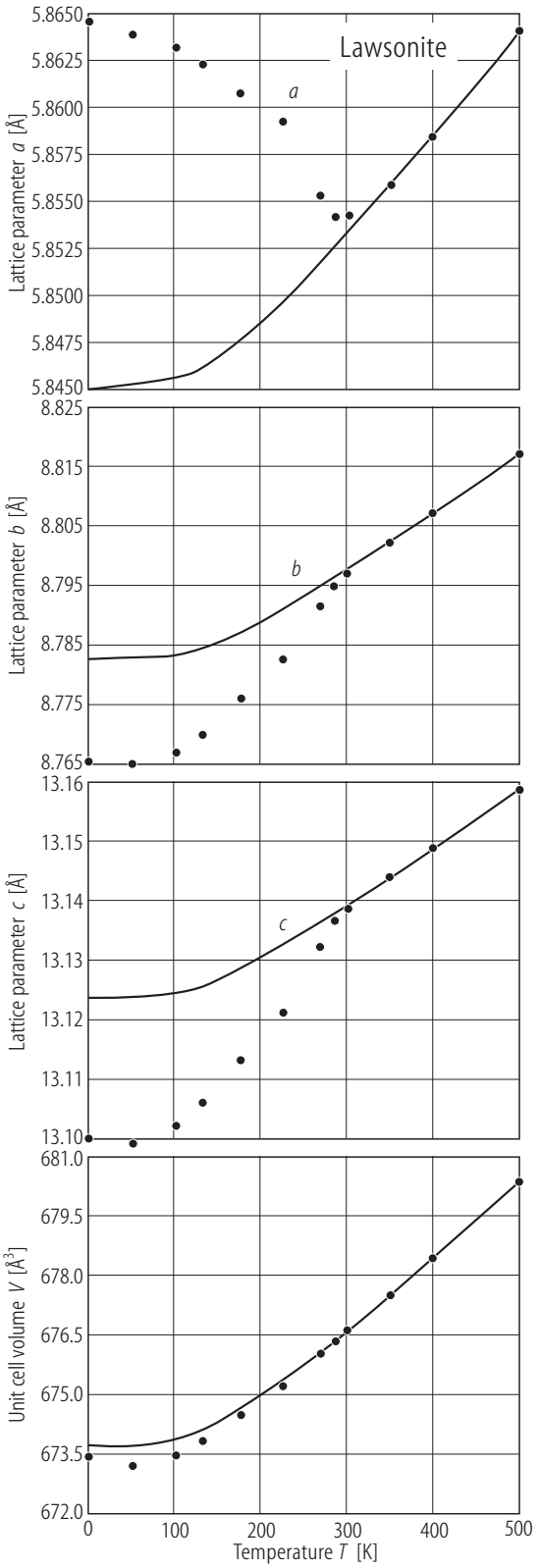

Fig. 9. For caption see previous page

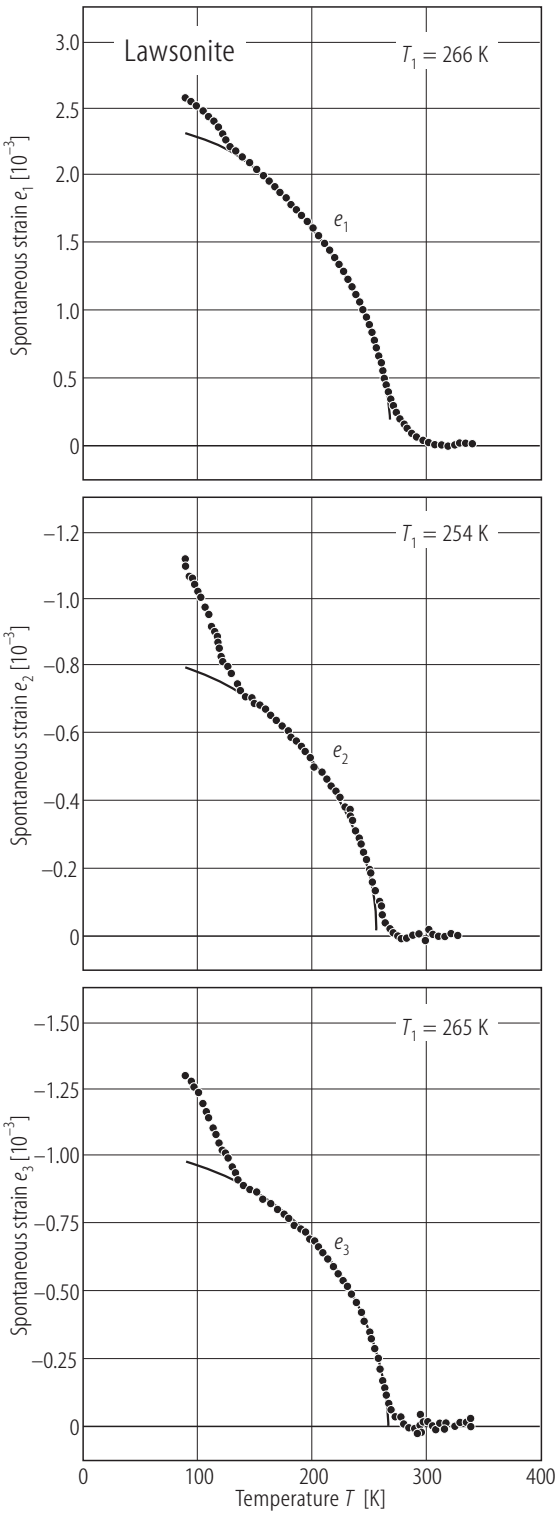

Fig. 10. For caption see previous page

Hennomartinite

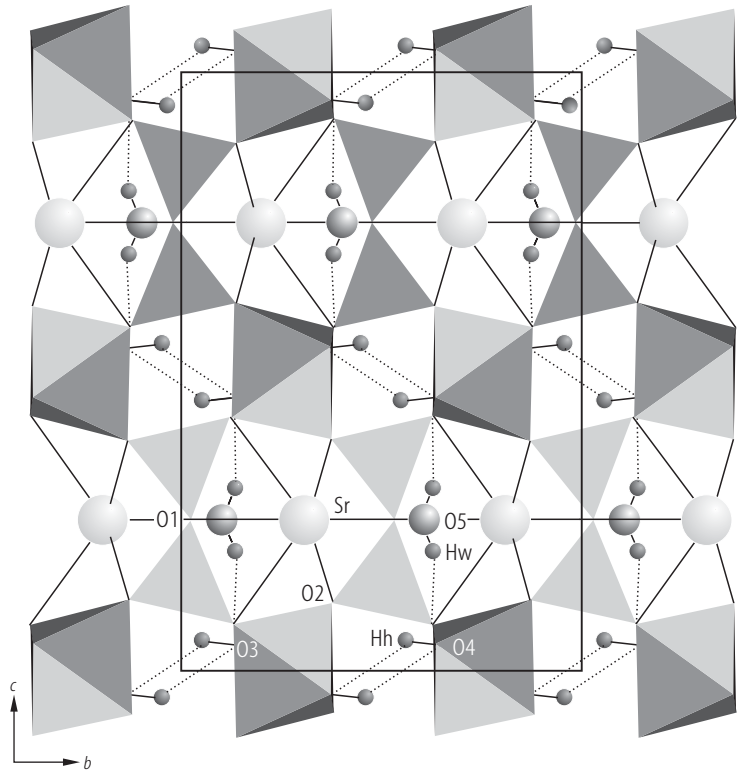

a

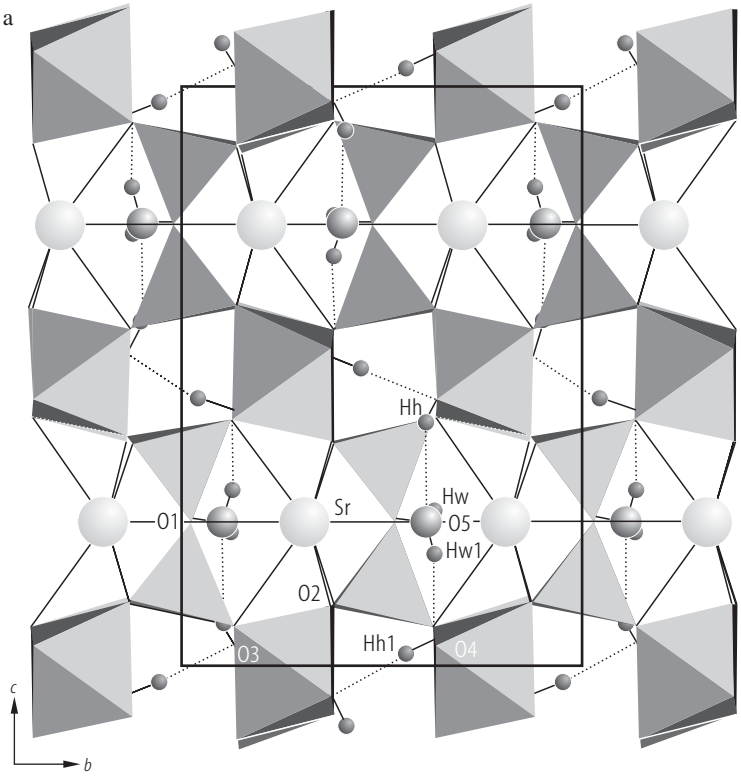

b

Fig. 11. Hennomartinite. **(a)** The Cmcm structure at 518 K projected along [100]. The edge sharing Jahn-Teller distorted MnO_6 octahedra form rods parallel to [100], which are interconnected by Si_2O_7 group. The interstices of the framework are occupied by Sr atoms (large spheres), H_2O molecules (O5 = medium spheres) and by the H atoms (small spheres of the OH group). Dotted lines represent O - - - H bonds between 2.0 and 2.1 Å; **(b)** $P2_1cn$ structure at 295 K projected along [100]. Only one untwinned atom set and only the L H atom positions are shown. Dotted lines represent O - - - H bonds between 1.8 and 2.3 Å. Symbols as in **(a)** [96L1].

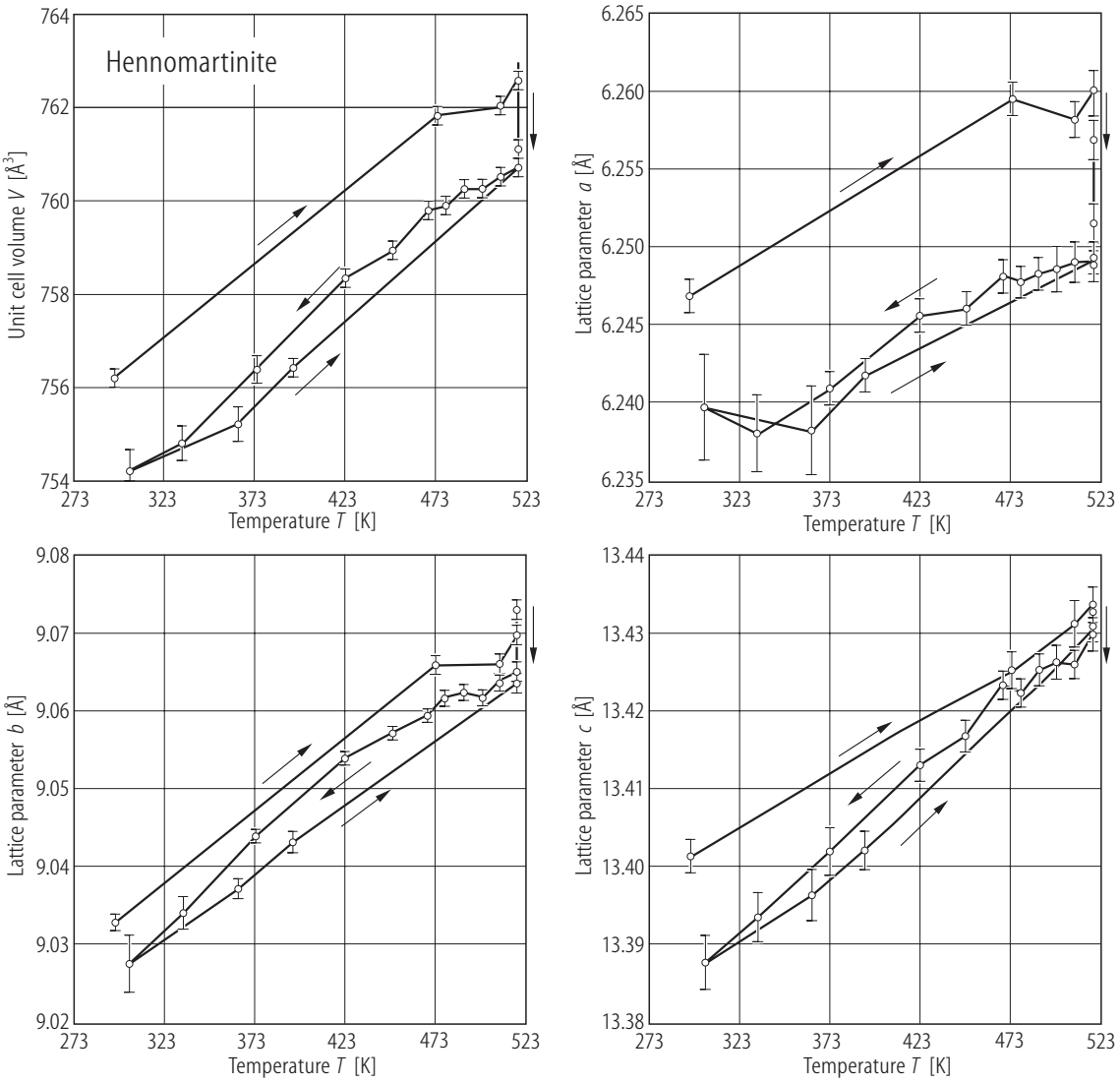

Fig. 12. Hennomartinite. Unit cell parameters and volume versus temperature [96L1]. The heating and cooling path is indicated by arrows starting at 295 K.

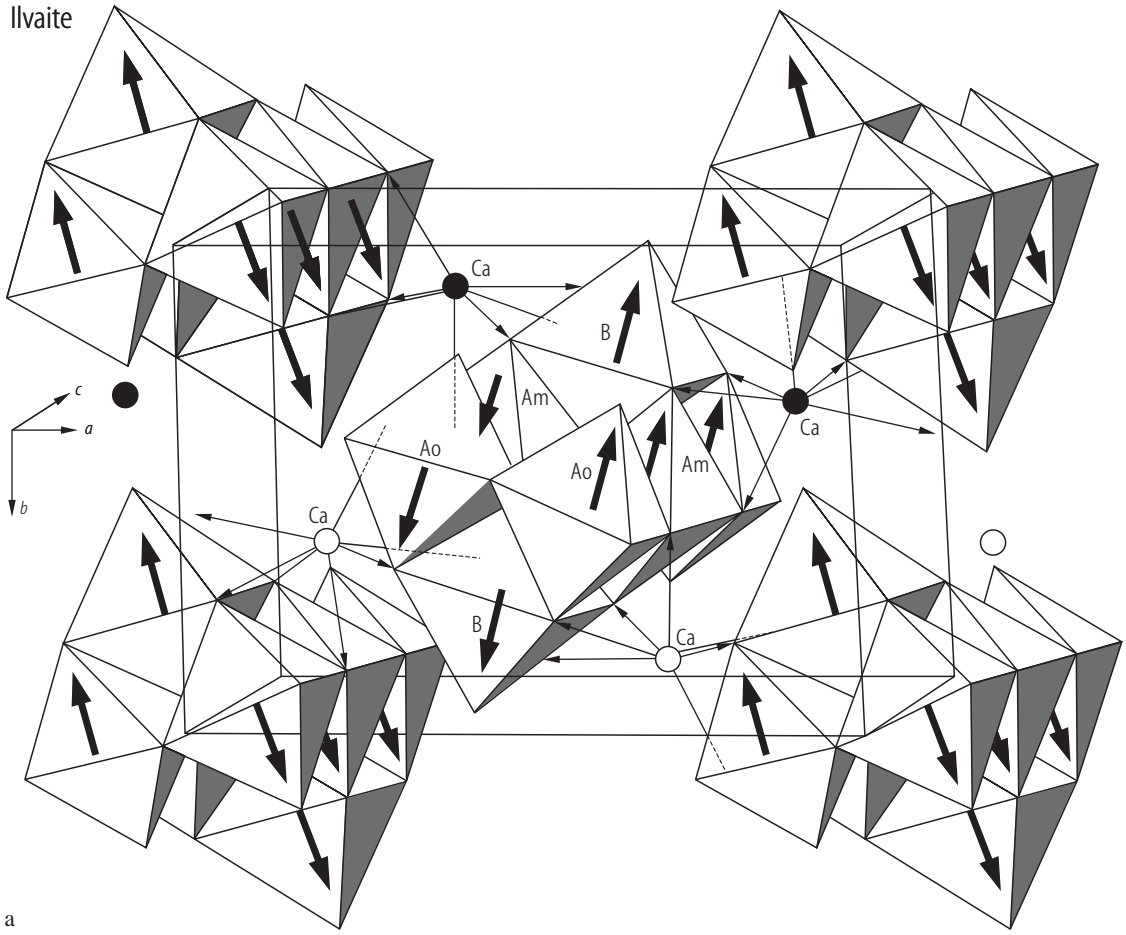

a

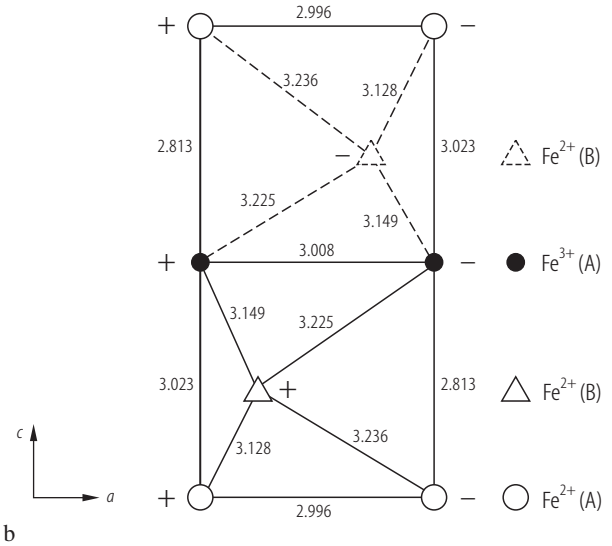

b

Fig. 13. $CaFe_{2.92}Al_{0.01}Mn_{0.02}Si_2O_7$ O(OH) ilvaite. **(a)** Magnetic structure at 5K; **(b)** spatial arrangement of Fe^{2+}(A), Fe^{3+}(A) and Fe^{2+}(B) sites; distances in Å [84G1, 90G1].

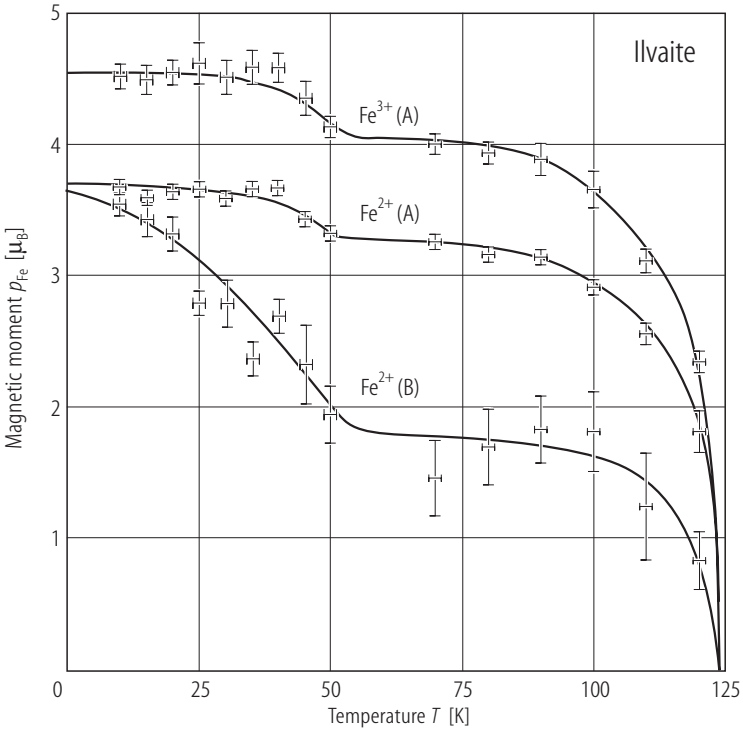

Fig. 14. $CaFe_{2.92}Al_{0.01}Mn_{0.02}Si_2O_7O(OH)$. Thermal variations of magnetic moments at Fe^{2+}(A), Fe^{3+}(A) and Fe^{2+}(B) sites [90G1].

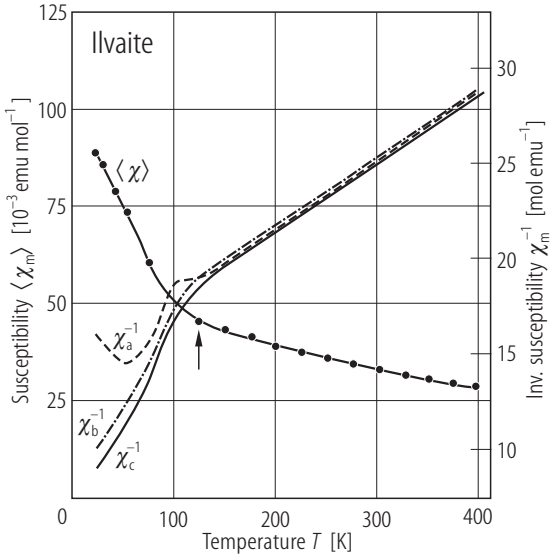

Fig. 15. Ilvaite. Temperature dependences of the magnetic susceptibilities χ_a, χ_b, χ_c, along ***a***, ***b***, ***c***-axes, respectively, and the mean molar susceptibility $\langle\chi\rangle = (\chi_{\parallel} + 2\chi_{\perp})/3$ where $\chi_{\parallel} - \chi_{\perp} = \pm\{(\chi_a - \chi_c) + (\chi_b - \chi_c)\}$ [87G2].

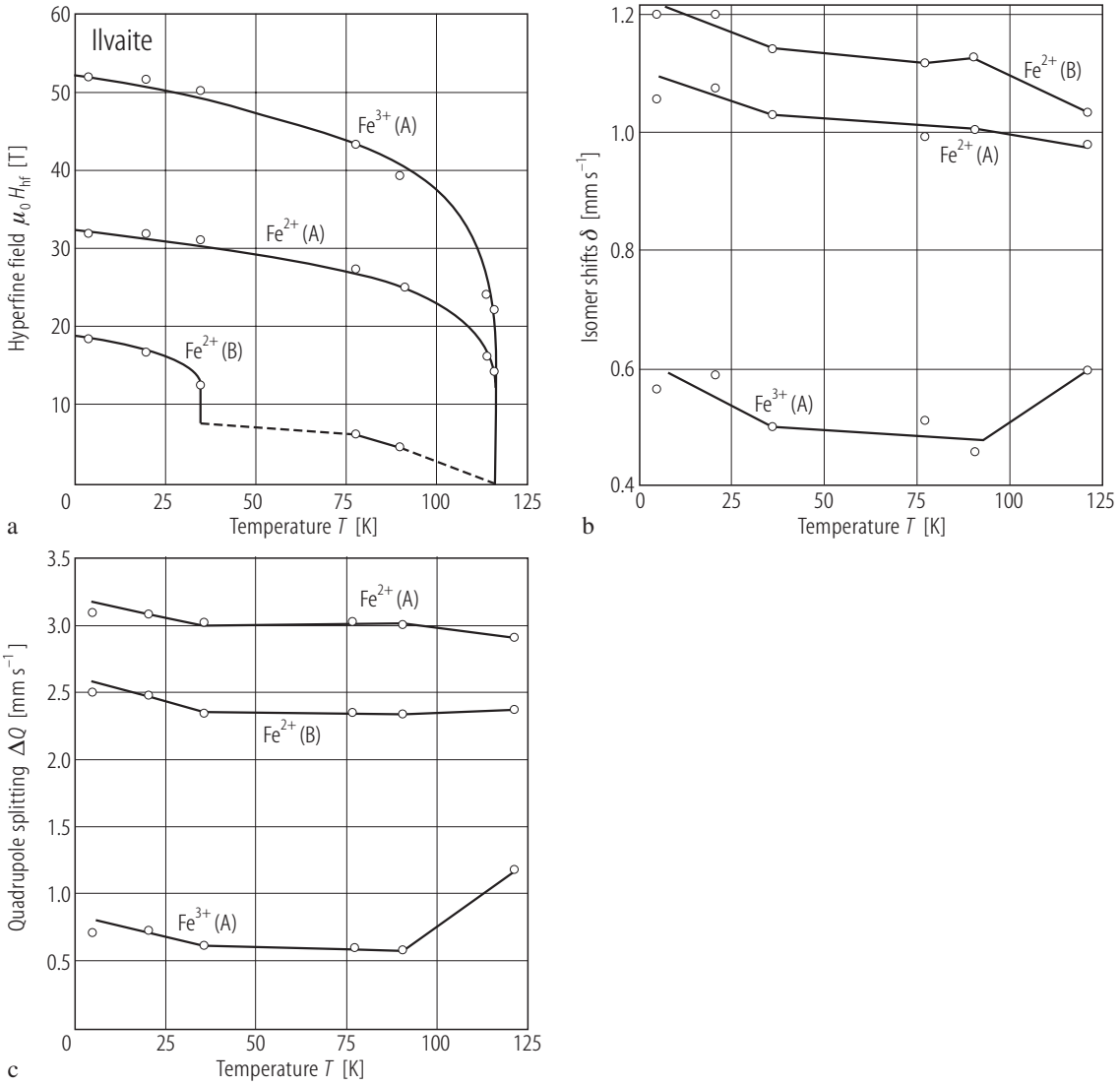

Fig. 16. $CaFe_{2.73}Al_{0.12}Mn_{0.07}Mg_{0.04}Si_2O_8$ (OH). Temperature dependences of the: **(a)** ^{57}Fe hyperfine fields; **(b)** isomer shift and **(c)** quadrupole splitting [88X1].

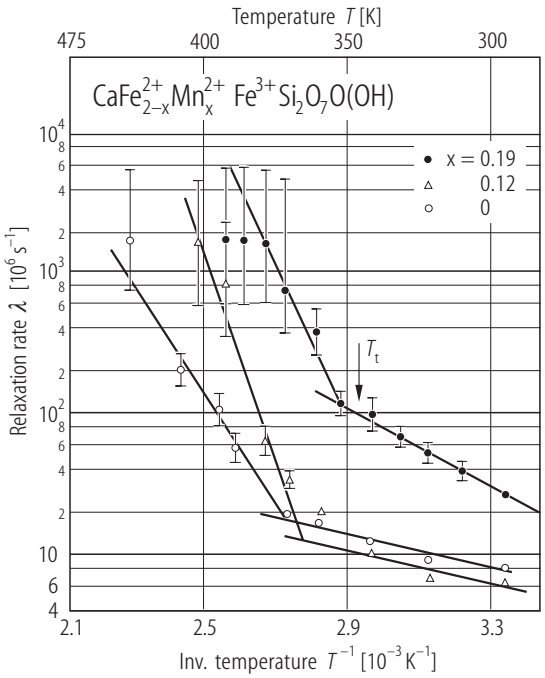

Fig. 17. $CaFe^{2+}_{2-x}Mn^{2+}_{x}Fe^{3+}Si_2O_7O(OH)$. Relaxation rate as function of (reciprocal) temperatures (295 K < T < 450 K) for samples with x = 0; 0.12 and 0.19 [92G1].

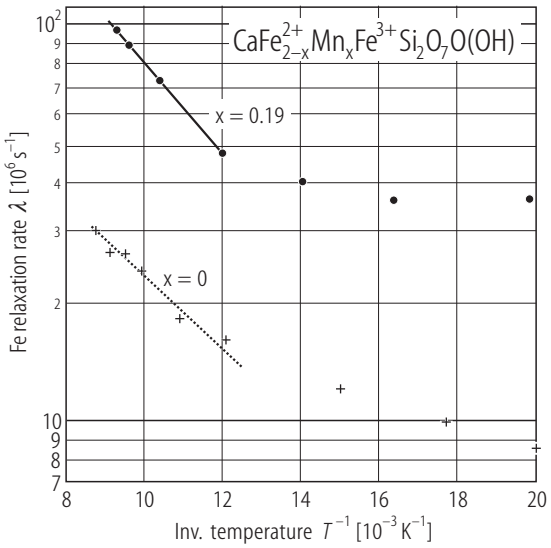

Fig. 18. $CaFe^{2+}_{2-x}Mn_xFe^{3+}Si_2O_7O(OH)$ Temperature dependences of the relaxation rates (50 K < T < 120 K) in synthetic ilvaites with x = 0 and 0.19 [95C1].

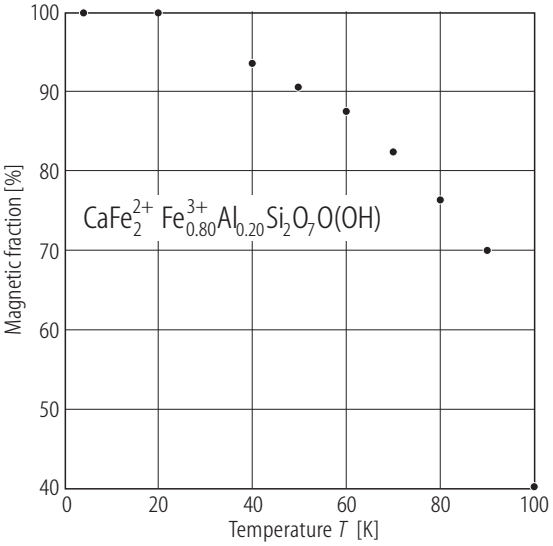

Fig. 19. $CaFe^{2+}_{2}Fe^{3+}_{0.80}Al_{0.20}Si_2O_7O(OH)$. Temperature dependence of the magnetic fraction of iron [95C1].

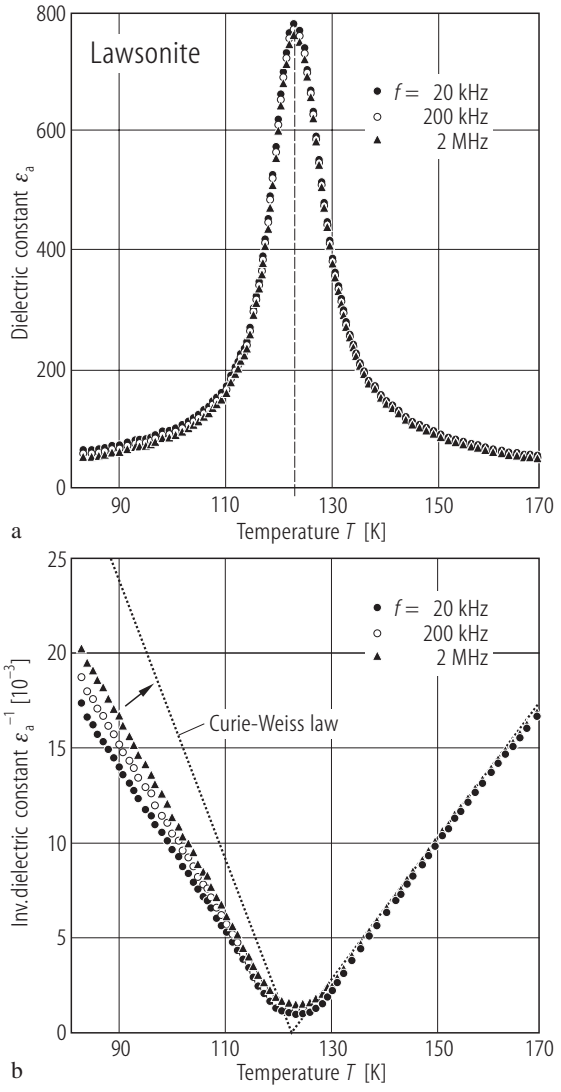

Fig. 20. Lawsonite. Temperature dependences of the **(a)** dielectric constant ε_a (measured) and **(b)** inverse value ($1/\varepsilon_a$) measured along the [100] direction for different frequencies. The electric measuring field E_{ac} = 1 V/cm, E_{dc} = 0. The dotted line indicates Curie-Weiss behaviour [00S2].

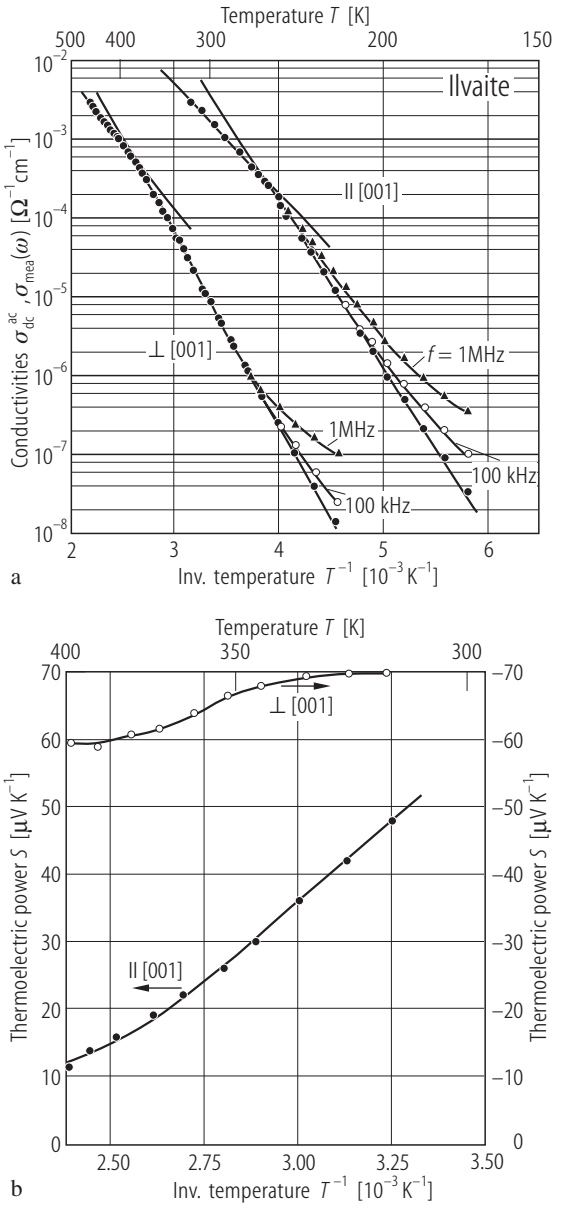

Fig. 21. Ilvaite. **(a)** Logarithm of extrapolated *dc* conductivity σ_{dc}^{ac} vs reciprocal temperature for measurements parallel and perpendicular to [001] and *ac* conductivity $\sigma_{mea}(\omega)$. **(b)** Thermopower, *S,* as a function of T^{-1}, measured ∥ and ⊥ to [001] [98S1].

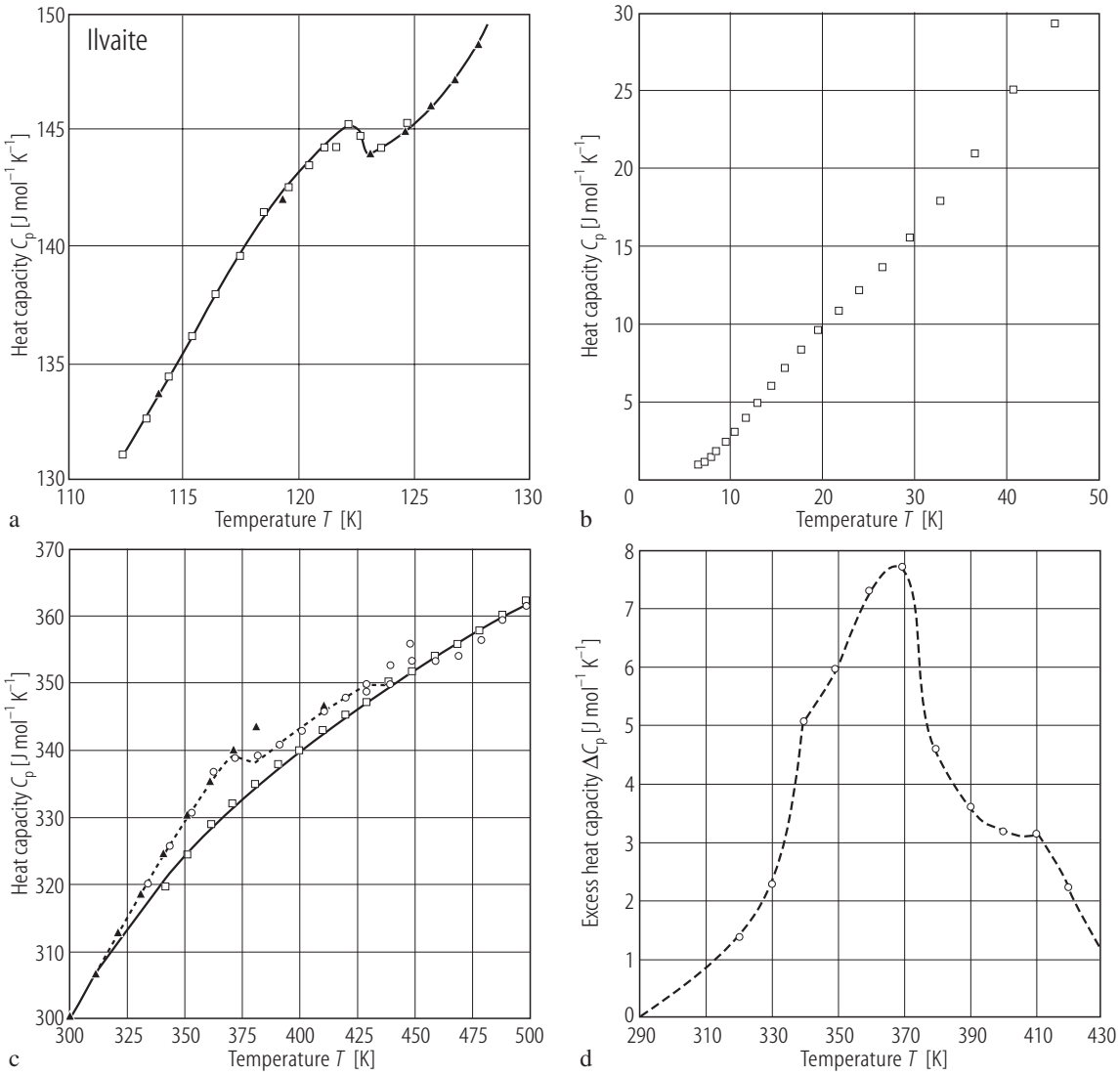

Fig. 22. Ilvaite. $Ca_{0.98}Mn_{0.021}Fe_{2.97}Al_{0.026}(Si_{1.99}O_7)O(OH)$. Molar heat capacity **(a)** in the region of antiferromagnetic transition; **(b)** in the temperature range 6.4…40 K; **(c)** in the temperature range $300 \leq T \leq 500$ K. The results of various series of samples were noted differently. In **(c)** triangles are the data obtained with adiabatic calorimeter. All other symbols indicate measurements made with differential scanning calorimeter. For the open squares the sample was heated at 750 K prior to the measurements [88R1]; **(d)** excess specific heat due to charge localization [88R1, 89G2].

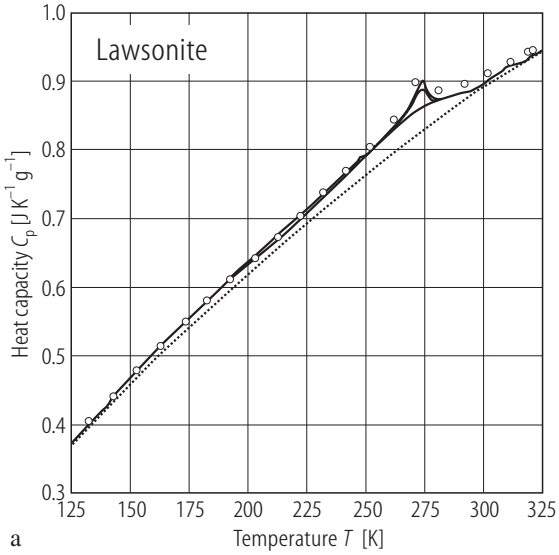

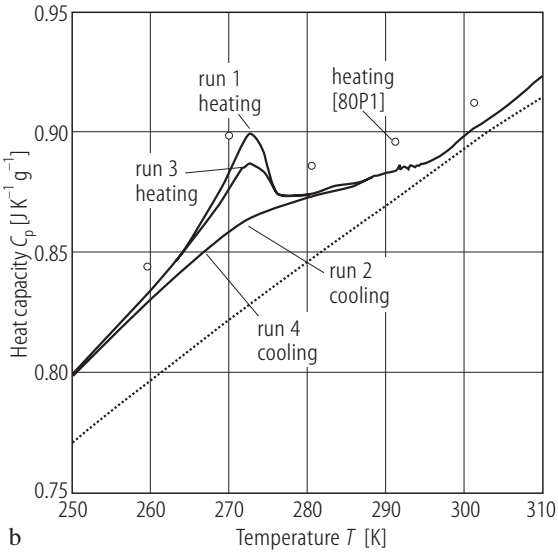

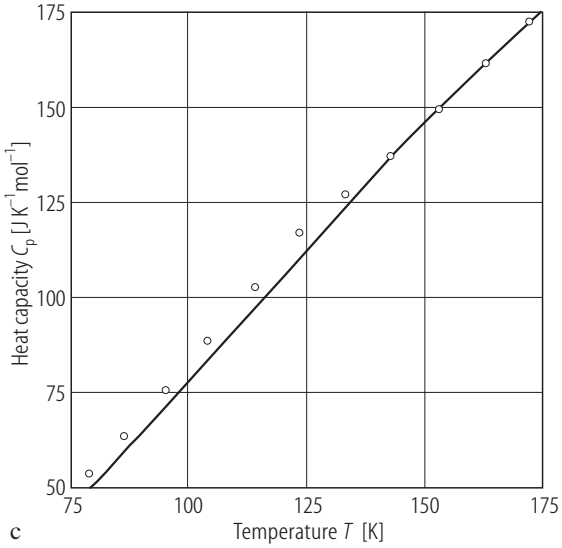

Fig. 23. Lawsonite, $Ca_{1.00}Al_{1.95}Fe_{0.05}Si_{2.00}O_7(OH)_2 \cdot H_2O$. Temperature dependences of the specific heat, **(a)** in whole temperature range [01M1]; **(b)** in the vicinity of the Cmcm-Pmcn transition. The four solid lines show the data for the two heating and two cooling runs [01M1] and circles show the data of [80P1] for heating; **(c)** data obtained in the vicinity of the Pmcn-$P2_1cn$ transition [80P1]. A step anomaly consistent with a second order phase transition is shown. Dotted line in **(a)**, **(b)** and solid line in **(c)** are data when no anomaly is expected to be present at 273 K **(a, b)** and 175 K **(c)**, respectively.

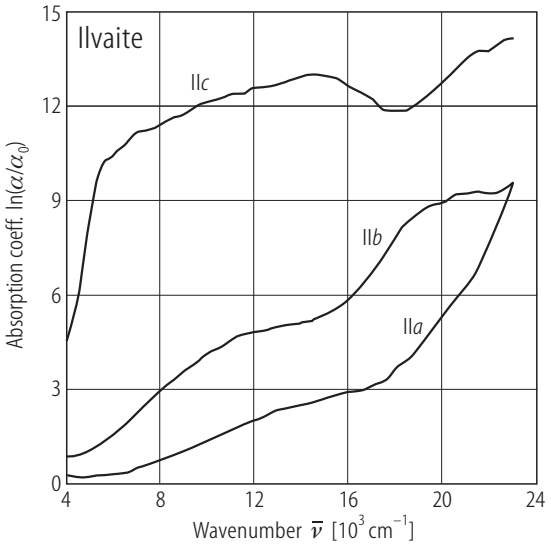

Fig. 24. Ilvaite, $Ca_{0.93}Fe_{2.73}Al_{0.05}Mn_{0.07}Si_2O_8(OH)$. Optical absorption spectra measured in the 4000…23000 cm^{-1} range, at room temperature. The ***E*** vector was oriented parallel to the three principal crystallographic axes of the orthorhombic system Pnma (the monoclinic distortion was disregarded) [89G3]. Absorption scale was given in natural logarithm for 8 μm sample thickness).

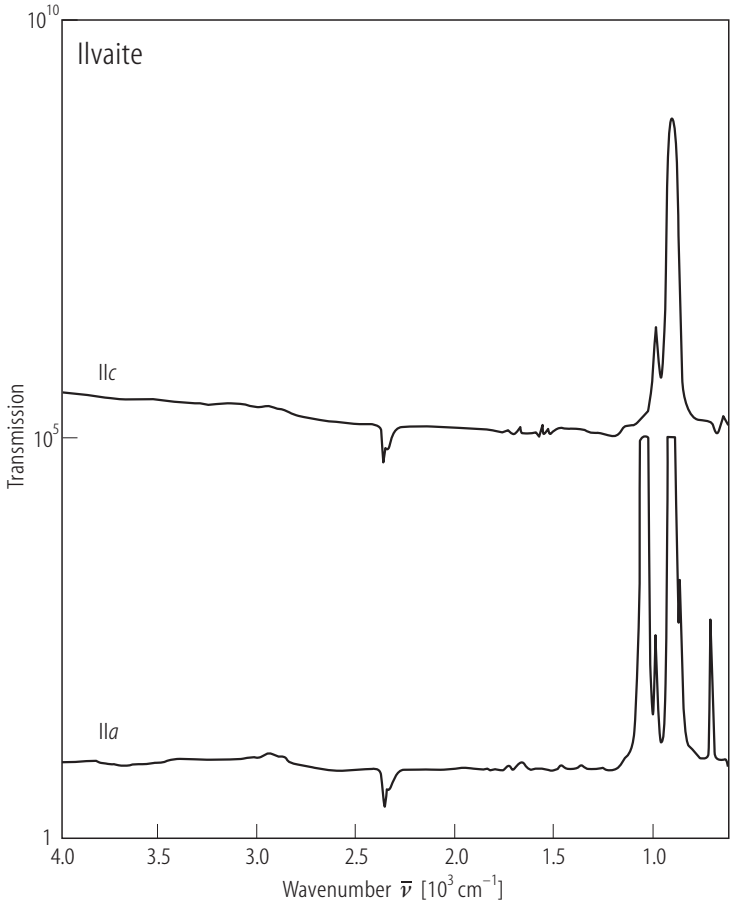

Fig. 25. Ilvaite, $Ca_{0.93}Fe_{2.73}Al_{0.05}Mn_{0.07}Si_2O_8(OH)$. Polarized single crystal transmission spectra in the mid-infrared frequency range (600…4000 cm^{-1}) (***E*** ∥ ***a***; ***E*** ∥ ***c***). Absorption scale is given in decadic logarithm [89G3]. The powder transmission spectra are not shown.

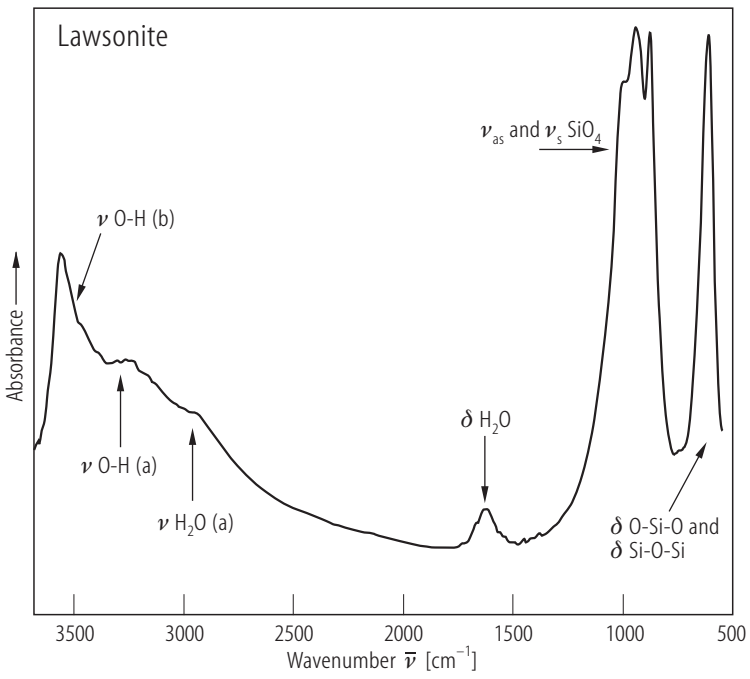

Fig. 26. Lawsonite. IR spectrum at ambient conditions, showing H_2O, OH and Si_2O_7 regions [99S1].

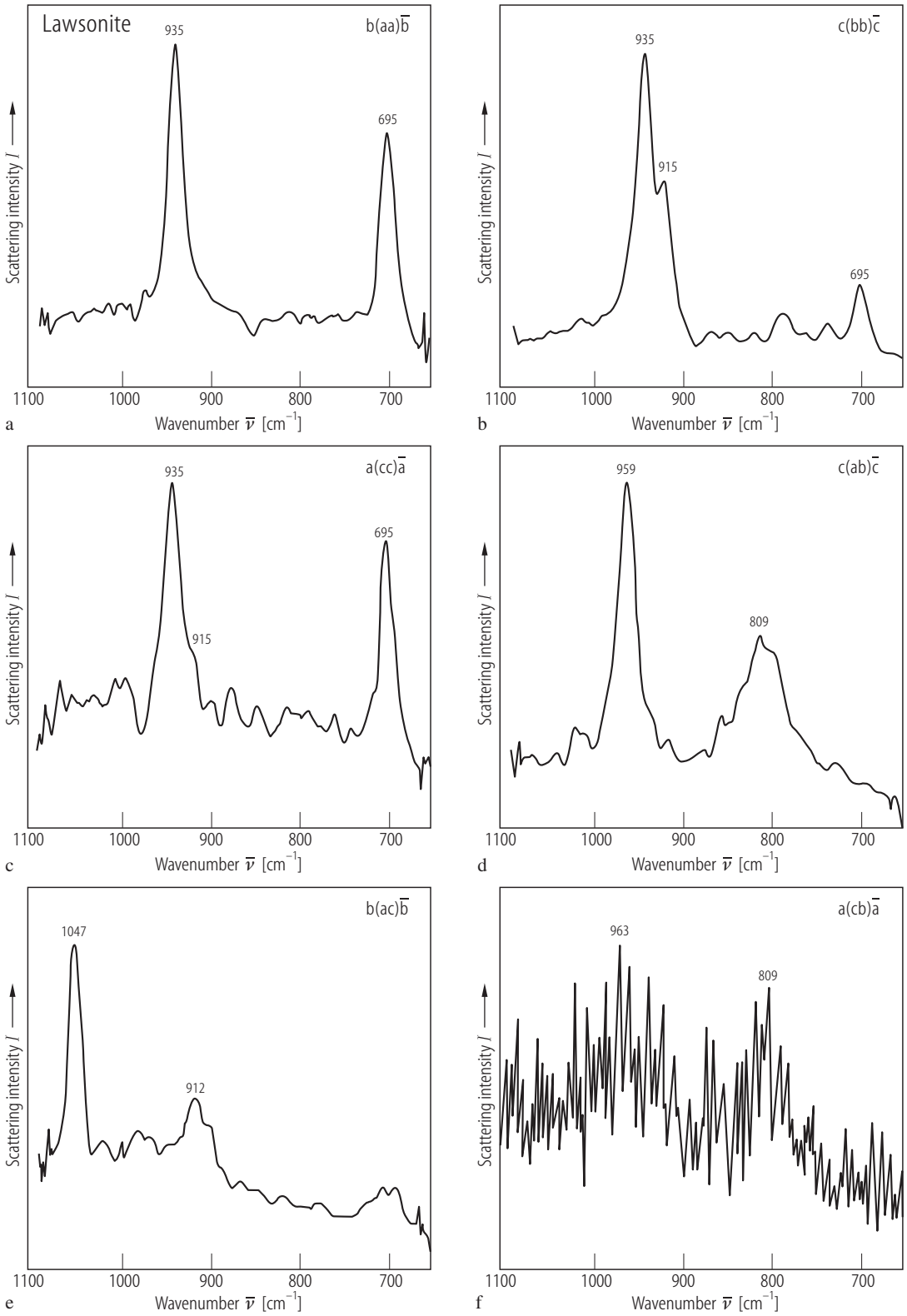

Fig. 27. Lawsonite. Oriented Raman spectra in the high frequency region **(a, b, c)**: A_g modes; **(d)**: B_{1g} modes; **(e)**: B_{2g} modes; **(f)**: B_{3g} modes [90L1].

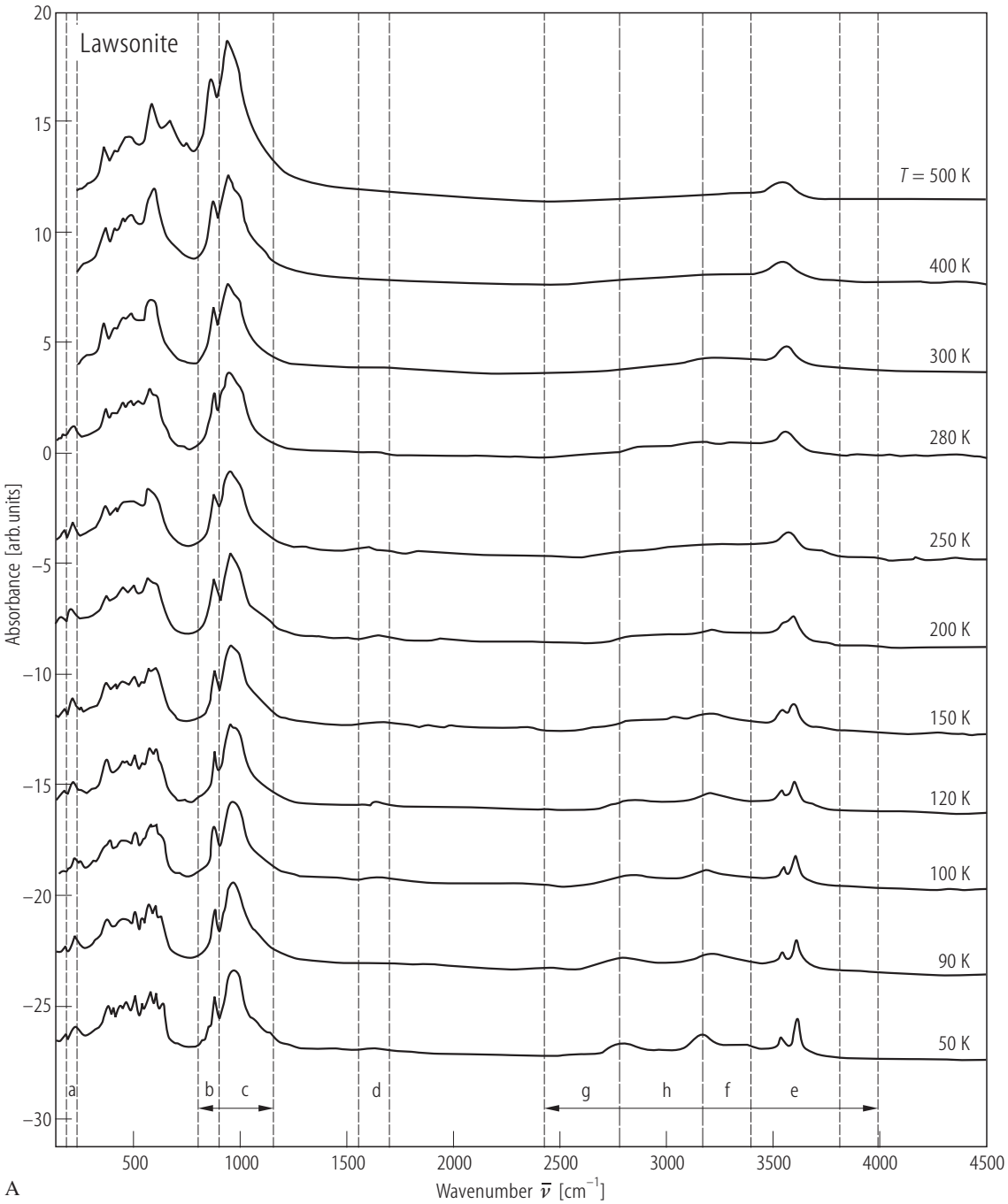

Fig. 28. Lawsonite. **(A)** Merged IR powder absorption spectra (peaks and regions chosen from the spectra for analysis are labelled a to h). **(B)** Variation of frequency as function of temperature for different regions in **(A)**. For the temperature dependence of peaks b (900 cm^{-1}) and e (3600 cm^{-1}) it was possible to apply a base line, and hence to calculate a function $\Delta\omega$ (solid line). **(C)** Thermal variation of Δcorr. On the right the changes of Δcorr, are shown as function of temperature. The vertical dashed lines in **(B)** and **(C)** represent the transition temperatures (T_2 = 130 K, T_1 = 265 K) [00M1].

For Figs. (B), (C) see next pages

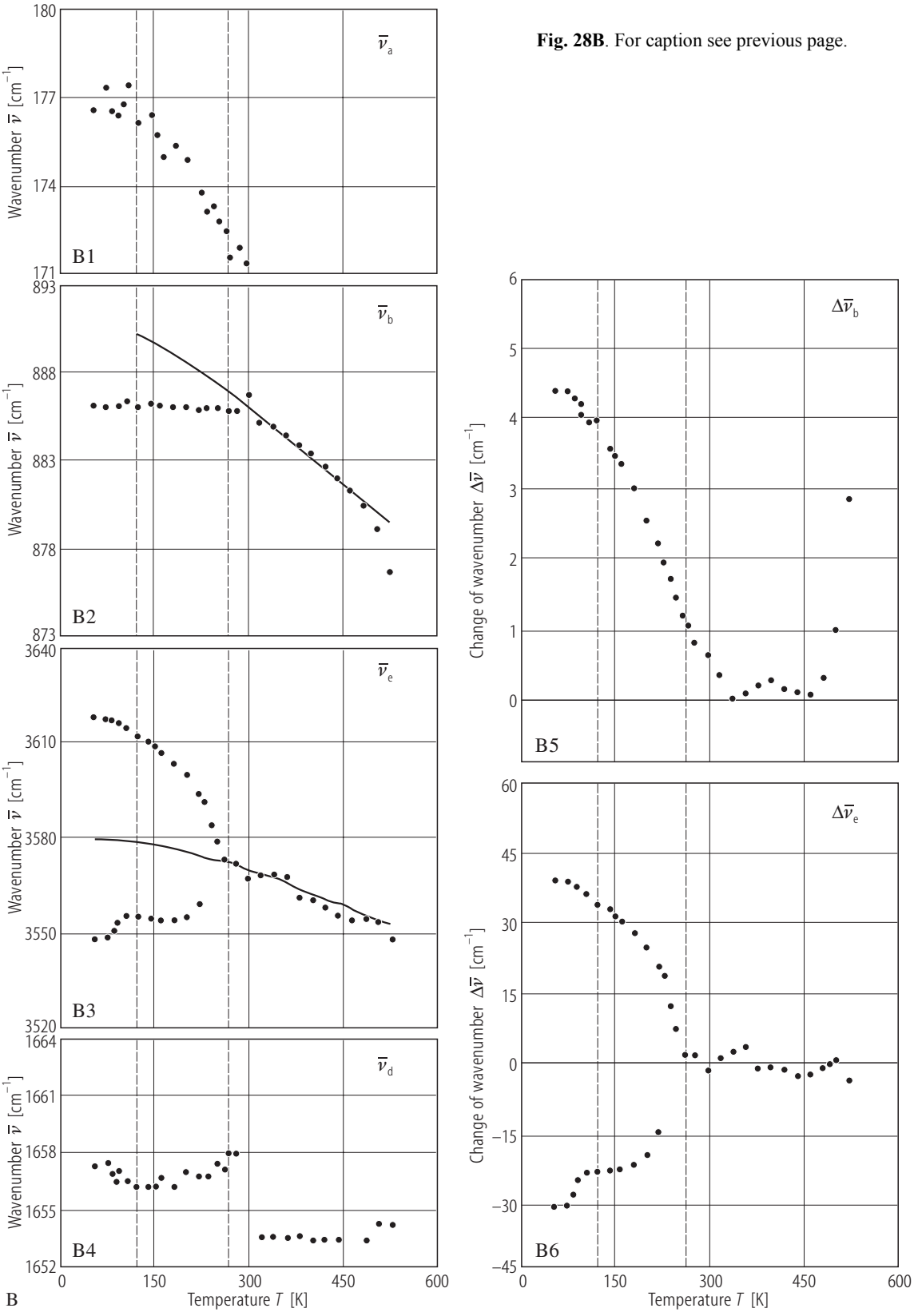

Fig. 28B. For caption see previous page.

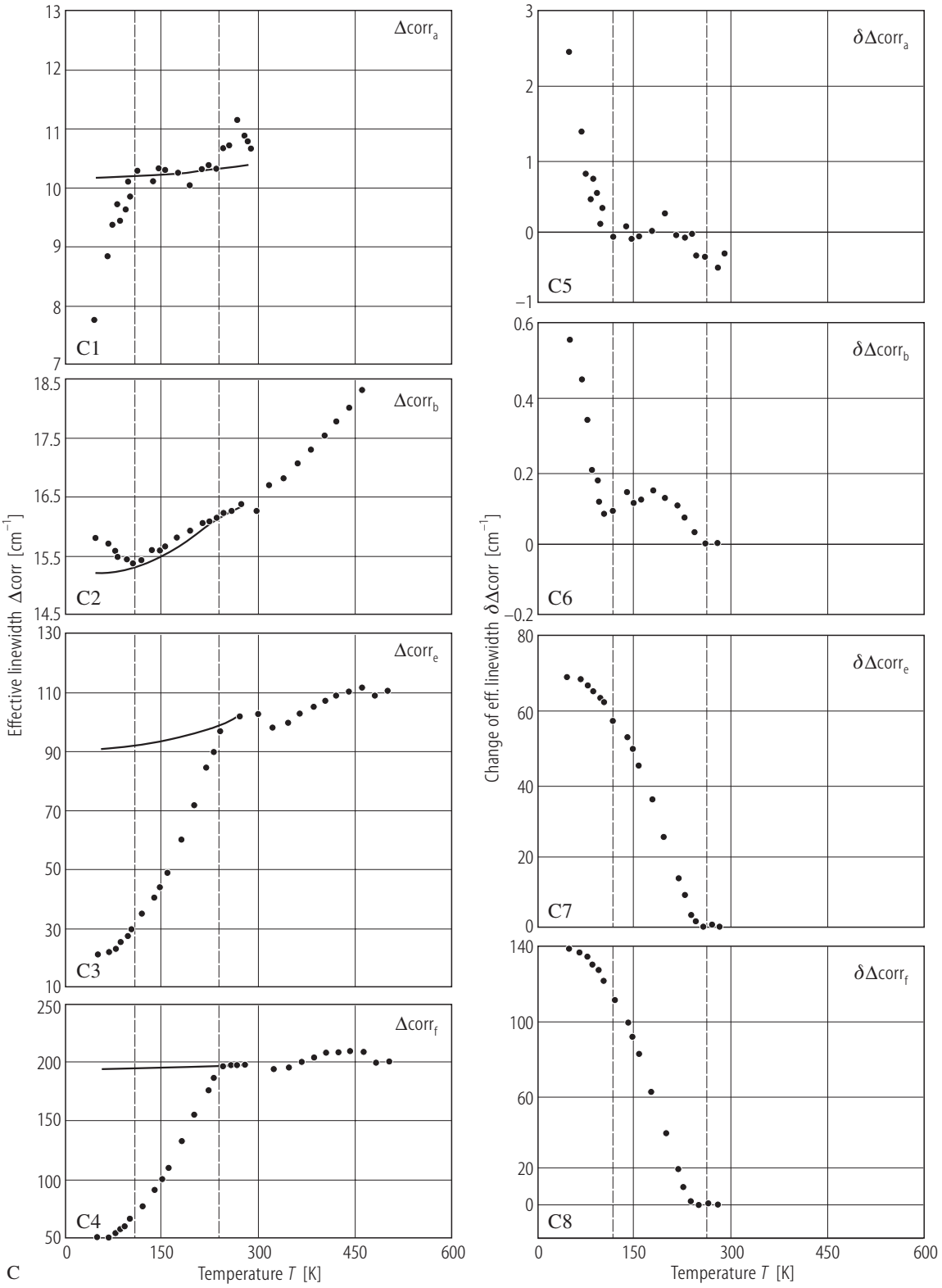

Fig. 28C. For caption see p. 135

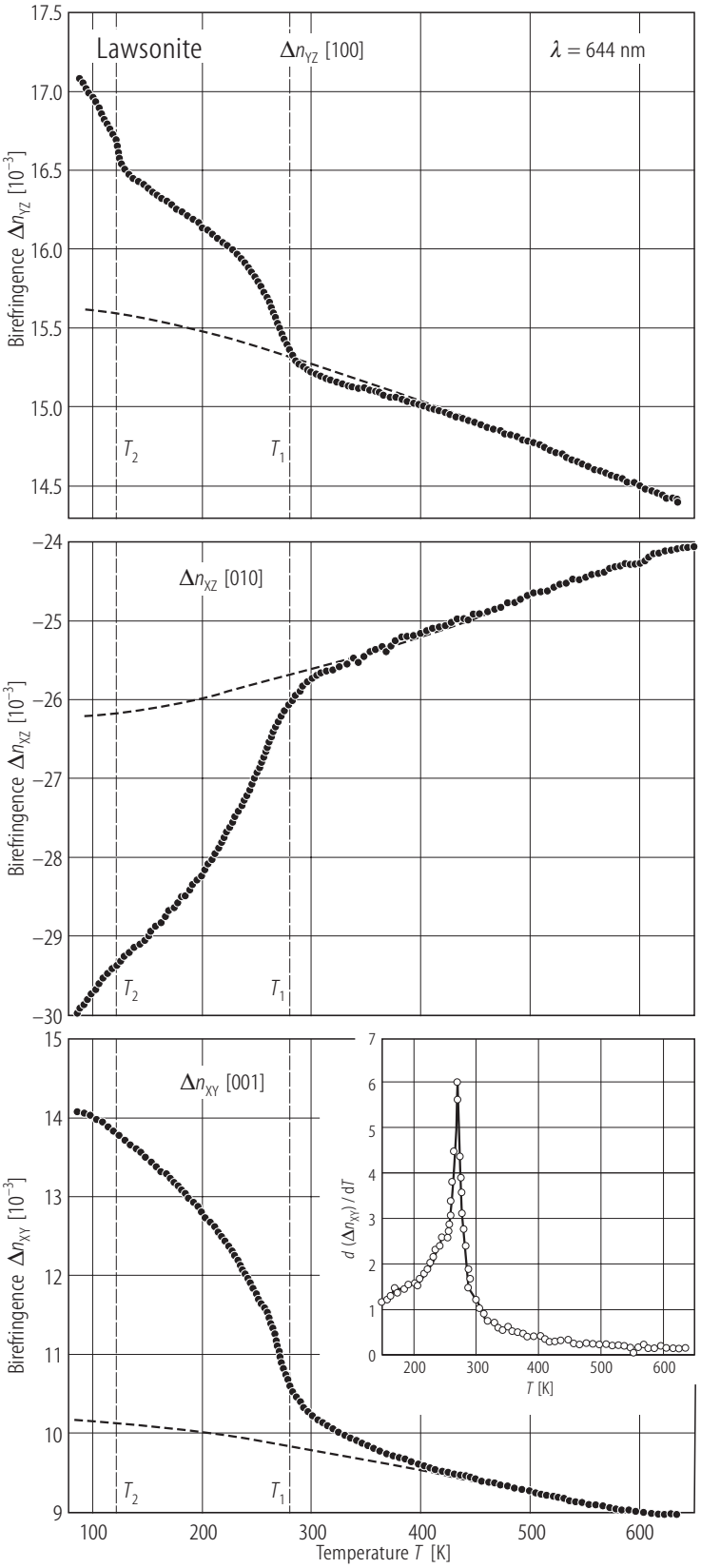

Fig. 29. Lawsonite. Temperature dependences of the optical birefringence along the principal crystallographic directions. In inset the temperature dependence of the derivative $d(\Delta n_{XY})/dT$ is shown [00S2].

References for 8.1.2.3

36K1 Kohkoros, P.: Naturwissenschaften 24 (1936) 619
41Y1 Ygberg, E.R.: Geol. Fören. Stockholm Förh. 134 (1941) 394
47W1 Wickman, F.E.: Arkiv. Kemi Mineral. Geol. 25 A (1947) 1
48T1 Takeuchi, Y.: X rays 5 (1948) 8
54B1 Belov, N.V., Mokeeva, V.I.: Tr. Inst. Kristallogr. Akad. Nauk, SSSR 9 (1954) 47
57S1 Seki, Y.: Sci. Rep. Saitama Univ., Ser. B 2 (1957) 363
59P1 Pabst, A.: Z. Kristallogr. 112 (1959) 53
59R1 Rumanova, I.M., Skipetrova, T.I.: Dokl. Akad. Nauk SSSR 124 (1959) 324 (Sov. Phys. Dokl. 4 (1959) 20
60D1 Davis, G.A., Pabst, A.: Am. J. Sci. 258 (1960) 689
60R1 Rumanova, I.M., Belov, N.V.: Kristallografiya 5 (1960) 215 (Sov. Phys. Crystallogr. 5 (1960) 199)
61A1 Agnell, S.O., Gay, P.: Nature 189 (1961) 743
61P1 Pabst, A.: Z. Kristallogr. 115 (1961) 307
61P2 Pistorius, C.W.F.T.: Am. Mineral. 46 (1961) 982
62H1 Heinrich, E.W., Deane, R.W.: Am. Mineral. 47 (1962) 758
62N1 Nickel, E.H., Charette, D.J.: Am. Mineral. 47 (162) 764
64A1 Abrashev, K.K., Ilyukhin, V.V., Belov, N.V.: Kristallografiya 9 (1965) 816 (Sov. Phys. Crystallogr. 9 (1965) 69)
68B1 Bartholomé, P., Duchesne, J.C., Van der Plas, L.: Ann. Soc. Geol. Belg. 90 (1968) 779
68N1 Nitsch, K.H.: Naturwissenschaften 55 (1968) 388
69C1 Cannillo, E., Dal Negro, A., Rossi, G.: Rend. Soc. Ital. Mineral. Petrol. 26 (1969) 2
69H1 Herzenberg, C.L., Riley, D.L.: Acta Crystallogr. A 25 (1969) 389
71B1 Baur, W.H.: Am. Mineral. 56 (1971) 1573
71B2 Borshagovskii, B.V., Marfunin, A.S., Mkrtchyan, A.R., Nagyaryan, G.N., Stukan, R.A.: Phys. Status Solidi (b) 43 (1971) 479
71F1 Filipenko, O.S., Pobedinskaya, E.A., Ponomarev, V.I., Belov, N.V.: Dokl. Akad Nauk SSSR 200 (1971) 591
71G1 Gerard, A., Grandjean, F.: Solid State Commun. 9 (1971) 1845
72B1 Beran, A., Bittner, H.: Neues Jahrb. Mineral. Monatsh. (1972) 551
72D1 Dietrich, V.: Schweiz Mineral. Petrogr. Mitt. 52 (1972) 57
74B1 Beran, A., Bittner, H.: Tschermaks Mineral. Petrogr. Mitt. 21 (1974) 11
74L1 Labotka, T.C., Rossman, G.R.: Am. Mineral. 59 (1974) 799
75G1 Gerard, A., Grandjean, F.: J. Phys. Chem. Solids 36 (1975) 1365
75G2 Grandjean, F., Gerard, A.: Solid State Commun. 16 (1975) 553
76H1 Haga, N., Takeuchi, Y.: Z. Kristallogr. 144 (1976) 161
77C1 Carlin, R.L., Van Duynveldt, A.J.: Magnetic Properties of Transition Metal Compounds, Springer Verlag, 1977
77H1 Heilmann, I.U., Olsen, N.B., Olsen, J.S.: Phys. Scr. 15 (1977) 285
77H2 Hill, G.: Z. Kristallogr. 146 (1977) 241
77P1 Paques-Ledent, M.T., Grandjean, F., Gerard, A.: Bull. Soc. R. Sci. Liege 46 (1977) 337
77P2 Pabst, A.: Neues Jahrb. Mineral. Abh 129 (1977) 1
77R1 Robinson, R.D., Fang, J.H.: Am. Mineral. 62 (1977) 167
78A1 Amthauer, G., Evans, B.J.: Phys. Chem. Miner. 3 (1978) 66
78B1 Baur, W.H.: Am. Mineral. 63 (1978) 311
79N1 Nolet, D.A., Burns, R.G.: Phys. Chem. Miner.4 (1979) 221
79Y1 Yamanaka, Y., Takeuchi, Y.: Phys. Chem. Miner. 4 (1979) 149
80E1 Evans, B.J., Amthauer, G.: J. Phys. Chem. Solids 41 (1980) 985
80P1 Perkins, D., Westrum, E.F., Essne, E.J.: Geoch. Cosmochim. Acta 44 (1980) 61
82F1 Finger, L.W., Hazen, R.M., Huges, J.M.: Yearbook Carnegie Inst. Washington 81 (1982) 386
83S1 Smith, K.A., Kirkpatrick, R.J., Oldfield, E., Henderson, D.M.: Am. Mineral. 68 (1983) 1206
83T1 Takeuchi, Y., Haga, N., Bunno, M.: Z. Kristallogr. 163 (1983) 267

84A1 Amthauer, G., Rossman, G.: Phys. Chem. Miner. 11 (1984) 37
84C1 Coey, J.M.D., Allan, J., Xuemin, K., Van Dang, N., Ghose S.: J. Appl. Phys. 55 (1984) 1963
84G1 Ghose, S., Hewat, A.W., Marezio, M.: Phys. Chem. Miner.11 (1984) 67
84G2 Ghose, S., Hewat, A.W., Marezio, M., Dang, N.V., Robie, R.A., Evans, H.T.: EOS, Trans. Am. Geophys. Union 65 (1984) 289
84L1 Litterst, F.J., Amthauer, G.: Phys. Chem. Miner.10 (1984) 250
85G1 Ghose, S., Sen Guputa, P.K., Schlemper, E.O.: Am. Mineral. 70 (1985) 1248
85S1 Sherman, D.M.: Phys. Chem. Miner.12 (1985) 161
85S2 Sherman, D.M., Waite, T.D.: Am. Mineral. 70 (1985) 1262
87D1 Döring, E., Hurkuck, W.: Z. Kristallogr.178 (1987) 54
87F1 Finger, L.W., Hazen, R.M.: Z. Kristallogr.179 (1987) 415
87G1 Ghazi-Bayat, B., Amthauer, G., Schurmann E., Hellner, E.: Mineral. Petrol. 37 (1987) 97
87G2 Ghosh, D., Kundu, T., Das Gupta, S., Ghose, S.: Phys. Chem. Miner.14 (1987) 151
88G1 Ghose, S.: in Structural and Magnetic Phase Transitions in Minerals, Ghose, S., Coey, J.M.D., Salje, E., (eds.), Springer Verlag, 1988, p. 141
88G2 Ghose, S., Hewat, A.W., Marezio, M., Dang, N.V., Robie, R.A., Evans, H.T.: Adv. Phys. Geochem. 7 (1988) 141
88R1 Robie, R.A., Evans, H.T., Hemingway, B.S.: Phys. Chem. Miner. 15 (1988) 390
88X1 Xuemin, K., Ghose, S., Dunlap, B.D.: Phys. Chem. Miner.16 (1988) 55
89G1 Ghazi-Bayat, B., Amthauer, G., Hellner, E.: Mineral. Petrol. 40 (1989) 101
89G2 Ghose, S., Tsukimura, K., Hatch, D.M.: Phys. Chem. Miner.16 (1989) 483
89G3 Güttler, B., Salje, E., Ghose, S.: Phys. Chem. Miner.16 (1989) 606
90G1 Ghose, S., Hewat, A.W., Pinkey, M.: Solid State Commun. 74 (1990) 413
90K1 Kundu, T., Ghosh, D.: Phys. Chem. Miner.17 (1990) 157
90L1 Le Cléach, A., Gillet, P.: Eur. J. Mineral. 2 (1990) 43
91N1 Nickel, E.H., Nichols, M.C.: Mineral Reference Manual, Van Nostrand Reinhold, 1991
92A1 Armbruster, T., Oberhansli, R., Bermanec, V.: Eur. J. Mineral 4 (1992) 17
92G1 Ghazi-Bayat, B., Behruzi, M., Litterst, F.J., Lottermoser, W., Amthauer, G.: Phys. Chem. Miner.18 (1992) 491
92L1 Li, Z., Zeng, Y.: Hyperfine. Interact. 70 (1992) 1033
93A1 Armbruster, T., Oberhansli, R., Bermanec, V., Dixon, R.: Schweiz. Mineral. Petrogr. Mitt. 73 (1993) 349
93B1 Bluncson, C.R., Evans, B.J.: J. Appl. Phys. 73 (1993) 5345
93G1 Ghazi-Bayat, B., Amthauer, G., Ahsbans, H.: Phys. Chem. Miner.20 (1993) 402
93K1 Kovalev, O.V.: Representation of the Crystallographic Space Groups, Stokes H.T., Hatch, D.M., (eds.), Gordon and Breach Science Publishers, New York, 1994, p. 390
93T1 Takeuchi, Y., Sawada, H., Taniguchi, H.: Proc. Inst. Natural Sci., Nihon Univ. 28 (1993) 39
94C1 Carpenter, M.A., Powell, R., Salje, E.K.H.: Am. Mineral. 79 (1994) 1053
94C2 Carrozzini, B.: Eur. J. Mineral 6 (1994) 465
94D1 De Melo, M.A.C., Klaus, H.H., Litterst, F.J., Amthauer, G.: Hyperfine. Interact. 85 (1994) 145
94P1 Pawley, A.: Contrib. Mineral. Petrol. 118 (1994) 99
94S1 Schmidt, M.W., Poli, S.: Earth Planet. Sci. Lett. 124 (1994) 105
94T1 Takeuchi, Y., Sawada, H., Taniguchi, H., Uno, R., Tabira, Y.: Z. Kristallogr. 209 (1994) 861
95C1 Cesena, M., Schepke, M., De Melo, M.A.C., Litterst, F.J., Amthauer, G.: J. Magn. Magn. Mater. 140-144 (1995) 1889
95G1 Gabula, S.P., Kozlova, S.G.: private commun. (cited by [95L1, 00S2])
95L1 Libowitzky, E., Armbruster, T.: Am. Mineral 80 (1995) 1277
95P1 Poli, S., Schmidt, M.W.: J. Geophys. Res. 100 (1995) 22299
95S1 Schmidt, M.W.: Am. Mineral. 80 (1995) 1286
96C1 Comodi, P., Zanazzi, P.F.: Am. Mineral. 81 (1996) 833
96H1 Holland, T.J.B., Redfernm, S.A.T., Pawley, A.R.: Am. Mineral. 81 (1986) 341
96L1 Libowitzky, E., Armbruster, T.: Am. Mineral 81 (1996) 9
96L2 Libowitzky, E., Rossman, G.R.: Am. Mineral. 81 (1996) 1080
98S1 Schmidbauer, E., Amthauer, G.: Phys. Chem. Miner. 25 (1998) 522

99D1 Daniel, I., Fiquet, G., Gillet, P., Schmidt, M.W., Hanfland, M.: Phys. Chem. Miner. 26 (1999) 406
99L1 Lager, G.A., Libowitzky, E., Schultz, A.J.: Proc. 17th General Meeting Int. Mineralog. Association, Toronto, 1999
99S1 Scott, H.P., Williams, Q.: Phys. Chem. Miner.26 (1999) 437
00C1 Chinnery, N., Pawley, A.R., Clark, S.M.: Am. Mineral. 85 (2000) 1001
00G1 Grevel, K.D., Nowlan, E.U., Fasshauer, D.W., Burchard, M.: Am. Mineral. 85 (2000) 206
00M1 Meyer, H.W., Carpeter, M.A., Graeme-Barber, A., Sondergeld, P., Schrauz, W.: Eur. J. Mineral. 12 (2000) 1139
00S1 Sinogeikin, S.V., Schilling, F.R., Bass, J.D.: Am. Mineral. 85 (2000) 1834
00S2 Sondergeld, P., Schranz, W., Tröster, A., Carpenter, M.A., Libowitzky, E., Kityk, A.V.: Phys. Rev. B 62 (2000) 6143
01M1 Martin-Olalla, J.M., Hayward, S.A., Meyer, H.W., Rames, S., Del Cerro, J., Carpenter, M.A.: Eur. J. Mineral. 13 (2001) 5
01M2 Meyer, H.W., Marion, S., Sondergeld, P., Carpenter, M.A., Knight, K.S., Redfern, A.T., Dove, M.T.: Am. Mineral. 86 (2001) 566